THÈSE

En vue de l'obtention du

DOCTORAT DE L'UNIVERSITÉ DE TOULOUSE

Délivré par :

Institut National Polytechnique de Toulouse (INP Toulouse)

Discipline ou spécialité :

Electromagnétisme et Systèmes Haute Fréquence

Présentée et soutenue par :

Mme JINGYI WANG
le mardi 9 janvier 2018

Titre :

Contribution to the characterization of stratified structures: electromagnetic analysis of a coaxial cell and a microstrip line

---

Ecole doctorale :

Génie Electrique, Electronique, Télécommunications (GEET)

Unité de recherche :

Laboratoire Plasma et Conversion d'Energie (LAPLACE)

Directeur(s) de Thèse :

M. JUNWU TAO

Rapporteurs :

M. FABIEN NDAGIJIMANA, UNIVERSITE GRENOBLE ALPES
M. GEORGES ALQUIE, UNIVERSITE PARIS 6

Membre(s) du jury :

M. FABIEN NDAGIJIMANA, UNIVERSITE GRENOBLE ALPES, Président
M. JUNWU TAO, INP TOULOUSE, Membre
Mme MARTINE POUX, INP TOULOUSE, Membre

RÉSUMÉ

L’objectif de cette étude est le développement des logiciels de modélisation électromagnétique spécifique aux cellules de caractérisation micro-ondes des matériaux. Ce développement s’appuie sur des méthodes numériques alternatives à celle des éléments finis largement utilisés dans des logiciels de commerce. Pour le besoin d’extraction des propriétés des matériaux par des méthodes de modélisation inverse, la recherche en l’efficacité numérique de l’analyse directe est le point central de cette étude.

Les cellules de caractérisation ciblées dans ce travail concernent une cellule coaxiale et une cellule en ligne planaire. La présence d’un matériau inconnu est modélisée par une structure de transmission hétérogène stratifiée. L’application de la méthode de l’opérateur transverse (TOM) sur la cellule coaxiale multicouche a permis la détermination de la constante de propagation du mode fondamental, la répartition des champs électromagnétique, et les caractéristiques des modes d’ordre supérieurs pour le besoin de la caractérisation des discontinuités entre ligne vide et ligne chargée. Dans le cas de la cellule en microruban l’utilisation de la méthode de résonance transverse modifiée (MTRM) a permis la détermination des caractéristiques des modes d’ordre fondamental et supérieur. Chaque cellule étant constitué de plusieurs sections différentes, la matrice S de l’ensemble sera déterminée par l’utilisation de plusieurs méthodes modales : méthode de raccordement modal (« Mode Matching ») et méthode variationnelle multimodale (MVM).

Les codes d’analyse directe sont couplés avec plusieurs programmes d’optimisation pour constituer les logiciels d’extraction des paramètres matériaux. Ceux-ci sont appliqués à des échantillons de matériaux sous forme de cylindre trouée par la cellule coaxiale, ou de plaquette rectangulaire mince par la cellule microruban. Des résultats d’extraction large bande ont été obtenus ; des valeurs sont comparables avec ceux publiés. Aussi bien des diélectriques à fortes pertes que des matéraux nano structurés ont fait l’objet des études par nos méthodes.

Mots clés:

Méthode numérique, procédure d'optimisation, cellule coaxiale, matériau diélectrique à forte perte, microruban, matériau de Nanostructure.

ABSTRACT

The objective of this dissertation is the development of electromagnetic modelling software specific to the cells of microwave material characterization. This development is based on numerical methods that are alternative to finite element method which is widely used in commercial software. For the need to extract the properties of materials by inverse modelling methods, research into the numerical efficiency of direct analysis is the focus in this thesis.

The characterization targeted cells in this work concern a coaxial cell and a planar line. The presence of an unknown material is modelled by a stratified heterogeneous transmission structure. The application of the transverse operator method (TOM) on the multi-layered coaxial cell allowed the determination of the propagation constant of fundamental mode and its corresponding field distribution of the electromagnetic fields, and the characteristics of higher-order modes for the need of the characterization of discontinuities between empty line and loaded line. In the case of the microstrip line, the use of the modified transverse resonance method (MTRM) allowed the determination of characteristics of the fundamental and higher order modes. Since each cell consists of several different sections, the matrix S of the set will be determined by the use of the several modal methods, such as modal connection method ("mode matching") and multimodal variational method (MVM).

The direct analysis codes are coupled with several optimization programs to constitute the software for extracting the material parameters. These are applied to material samples in cylinder form holed by the coaxial cell, or thin rectangular wafer by the microstrip line. Broadband extraction results were obtained, values are comparable with those published. Both high-loss dielectrics and nanostructured materials have been studied by our methods.

Keywords:

Numerical method, optimization procedure, coaxial cell, high-loss dielectric material, microstrip line, nanostructure material.

Table of contents

LIST OF SYMBOLS

List 1: BASIC SYMBOLS

SYMBOLS	DESCRIPTIONS
i or j	Imaginary number $i^2 = -1$ or $j^2 = -1$
ε	Permittivity
ε_0	Permittivity in free space
ε_r	Relative permittivity
$\tan\delta$	Loss tangent
ε'	Dielectric constant
ε''	Dielectric loss
μ	Permeability
μ_0	Permeability in free space
μ_r	Relative permeability
f	Frequency
ω	Angular frequency
λ_c	Cutoff wavelength
c_0	Light speed in free space
α	Attenuation constant
β	Phase constant
γ	Propagation constant ($\alpha+j\beta$)
k_0	Propagation constant in free space
ρ	Radial distance in cylindrical coordinate
φ	Azimuth in cylindrical coordinate
z	Longitudinal height in cylindrical coordinate
a	Inner radius of coaxial cell
b	External radius of coaxial cell
η	Known 4 by 4 matrix for transformation
η_0	Known 2 by 2 matrix for transformation
λ	Eigen value
w	Width of stripline of microstrip
h	Height of substrate of microstrip
t_1	Thickness of ground plane of microstrip
t_2	Support height
τ	Thickness of strip line of microstrip
ζ	Airgap between strip and sample
Ω	Impedance unit

List 2: MAIN SYMBOLS IN THEORETICAL FORMULATIONS

SYMBOLS	DESCRIPTIONS
$\mathbf{E}$	Electric field
$\mathbf{H}$	Magnetic field
$\mathbf{D}$	Electric flux density
$\mathbf{B}$	Magnetic flux density
$\mathbf{M}$	Fiction magnetic current density
$\mathbf{J}$	Electric current density
L	Transverse operator
Φ	Transverse field vector
E_{t}	Transverse electric field
$\boldsymbol{e}_{\mathrm{tn}}$	Electric transverse field of nth mode
H_{t}	Transverse magnetic field
$\boldsymbol{h}_{\mathrm{tn}}$	Magnetic transverse field of nth mode
∂_{t}	Transverse curl operator
$\partial^{+}{}_{\mathrm{t}}$	Adjoint transverse curl operator
∂_{l}	Longitudinal derivative operator
i_n	Current vector
v_n	Voltage vector
A_n/B_n	Coefficients of voltage/current formulations
$\mathcal{H}$	Heaviside operator
δ_{mn}	Kronecker symblo
y_{n}	Mode admittance
Y_{n}	Admittance operator
k_{xn}	nth mode transverse propagation constant (x)
k_{yn}	nth mode transverse propagation constant (y)
a_n/b_n	Modal coefficients in dispersion matrix
u_z	Unit axis vector in z direction
$G(r\|r')$	Green's function
Z_{sc}	Short circuit impedance
Z_{oc}	Open circuit impedance
Z_{load}	Load impedance
Z_L	Transmission line impedance of length L
Z_0	Characteristic impedance in free space
Z_{i}	Characteristic impedance in ith region
Γ	Reflection coefficient
P	Transmission coefficient

GENERAL INTRODUCTION

Modelling and simulation are essential to the design of compact and high-performance electronic systems working in higher broad frequency bands in the field of electromagnetics engineering. The development of modelling software allowing the research of microwave material characterization exempts from a long and expensive experimentation especially in the domain where their crucial parameters are highly attractive in a variety of applications from communication devices to civilian services. There are commercial electromagnetic packages that are used by the engineers during the design, analyse, implementation and test stages. Researchers have also developed their own packages from the numerical methods as well as using commercial ones, but makes software programming easy-controllable and object-oriented. Numerical implementation including computer programming and simulations is related to the extraction of microwave materials properties by means of measurements and experiments. To establish the relationship between the measured scattering parameters and the material properties, a full wave analysis is needed which consists of two problems: the forward (or direct) modelling problem of characteristic scattering coefficients for given complex permittivity and permeability, and the inverse modelling problem of determination the material properties for a given diffraction matrix.

The direct numerical analysis about characterization of scattering matrix is of the scope in this study. For the research in direct electromagnetics analysis, involving the study of electric and magnetic fields and their interaction, it uses the proper mathematics of physical phenomena and principles. Electric and magnetic phenomena are well-established on Maxwell's equations including Faraday's law of induction, Ampere's law, Gauss's law for electricity and magnetism, written in modern form with vector differential expression, they are:

$$
\begin{aligned}
&\nabla \times \boldsymbol{E} = -\frac{\partial}{\partial \boldsymbol{t}} \boldsymbol{B} - \boldsymbol{M} \\
&\nabla \times \boldsymbol{H} = \frac{\partial}{\partial \boldsymbol{t}} \boldsymbol{D} + \boldsymbol{J} \\
&\nabla \cdot \boldsymbol{D} = \rho \\
&\nabla \cdot \boldsymbol{B} = 0
\end{aligned}
$$

with the associated constitutive equations

$$
\begin{aligned}
\boldsymbol{B} &= \mu \boldsymbol{H} \\
\boldsymbol{D} &= \varepsilon \boldsymbol{E}
\end{aligned}
$$

Note that $\nabla\cdot$ is divergence operator and $\nabla\times$ is curl operator. Faraday' s law of induction is that the curl of electric field (***E***) is equal to the negative of rate of charge of the magnetic flux through the area enclosed by the loop, with ***E***, ***B*** and ***M*** being the electric field, magnetic flux density and fictitious magnetic current density; Ampere's law is that the curl of the magnetic field (***B***) is proportional to the electric current flowing the loop with ***H***, ***D*** and ***J*** being magnetic field, electric flux density, and electric current density; Gauss's law of electricity is that the electric flux out of any closed surface is proportional to the total charge enclosed within the surface with ρ the net electric charge density and that of magnetism is the net magnetic flux out of any closed surface being zero. In the associate functions, ε and μ are electric permittivity and magnetic permeability of media.

The solution to time-dependent Maxwell's equations is in general intractable, with difficulties due mainly to the imposition of the boundary conditions. Normally the closed-form analytical solution is not amenable to offer a complete description of electromagnetic field at every point in the most structures used in today's integrated circuits. Therefore, the right efficient numerical approximation is practical and needed for characterizations to model the structures. In this thesis, it focusses exclusively on the computational electromagnetics which is a multi-disciplinary field composed of electromagnetic theory and numerical methods with mathematic algorithm, and computer science. These techniques have been available, grown and matured to the point, for realistic problems in microwave engineering. Many numerical methods have been invented and the somewhat more classical methods have been refined for those modern structures. Although the rapid advent in computers imposes less severe restrictions on the temporary storage requirements and CPU time, it is prerequisite for any numerical methods for characterizations. In the development of numerical methods, versatility is another of its strong points. Numerical methods are chosen on the basis of trade-offs between accuracy, speed, storage requirement, versality, etc., and are often structure-dependent. Obviously, when a specific structure is analysed, one should make a choice as to which method is best suited for the structure.

The inverse problem is the second step after the direct analysis by numerical method; the complex permittivity and permeability of the material are extracted by matching theoretical and measurement results. This dissertation is organized into four chapters to discuss the direct problem for characterization of the scattering parameters and the inverse problem for electromagnetic properties extraction.

In modern computational electromagnetics (CEM), these methods form the basis for the now ubiquitous method of moment (MoM) and finite element method (FEM). While Rayleigh-Ritz and Galerkin's methods are in principle very different, they lead to the same set of discretized equations, are closely related, and are often discussed as if they were identical. Whilst the most the widely used method like method of moment, finite element method and finite difference time domain method, all have been implemented in powerful computer codes. For suitable problems, these methods are very powerful; and with the advent in computer speed and memory, the full-wave techniques are potentially very accurate. We will discuss this content in Chapter I subsequently.

Generally, the accuracy of these methods is related to the discretization (i.e. mesh size). The finer is the mesh, the better is the accuracy. The largest mesh size is limited by the available computer resources and takes a lot of time for a simulation. Then there are another class of numerical method such as transverse resonance method (TRM) and transverse operator method (TOM) for two-dimensional transverse discontinuity analysis, and mode-matching method (MMM), multimodal variational method (MVM) for three-dimensional longitudinal discontinuity analysis. When the discontinuity in the guide produce effects upon fields, it is possible to use analytical theory numerically to obtain the desired results. Such as multiple uniaxial discontinuities in guiding structure, i.e., the cylinder sample inside an enlarged coaxial cell, or block laid on the microstrip line, the hybrid numerical methods can be applied for the tangential and longitudinal discontinuity analysis. For more information, the numerical theories are elaborated in Chapter II for propagation constants and its corresponding field distributions in two-dimensional transverse discontinuity and in Chapter III for diffraction parameters in three-dimensional single and multiple uniaxial discontinuities.

Then in the fourth chapter, based on the direct analysis of the characterization of stratified structures and uniaxial discontinuities caused by the under-test sample insertion, the inverse problem for calculating the complex permittivity of the high-loss materials under test from the measured complex reflection coefficients can be solved in an optimization way by developed codes in coaxial cell, inside typical calibration scenarios are presented for the transition between vector network analyser (VNA) and the under-test set. Then we will concentrate on the object on the electromagnetic properties measurement of nanostructured metamaterial, such as double negative metamaterial (DNM), laying on the planar structure – microstrip line. Because of the heterogeneity of the loaded cross section, no analytical expression is available for calculation of the electromagnetic properties of the material from the measured parameters. Therefore, two steps are necessary for the determination of the electromagnetic properties of the sample. The first step is the direct problem, based on the Nicolson-Ross-Weir method, the effective constants of the transverse section are calculated from the complex permittivity and permeability of the sample. By making use of the modified transverse resonance method (MTRM) to analyse the multi-layered microstrip line for obtaining the propagation constants, the relative complex permittivity and permeability are deduced from the inverse modelling procedure.

CHAPTER I INTRODUCTION

I.1 MATERIAL CHARACTERIZATION

Microwave materials have been widely used in variety of applications at microwave frequency, and the understanding of material properties is a prerequisite requirement for the development of high-frequency devices. For a number of material the electrical properties is not known as accurate as it should be, or not at the right frequency for which the application works. That is how the characterization of materials properties came into being.

The accurate measurement of microwave materials properties is challenging since there has been an abundance of methods developed, analysed and employed for measuring electromagnetic permeability and permittivity, presented explicitly in the literatures, of dielectrics and magnetics [I-1], and composite metamaterials [I-2]. For example, a free-space measurement system [I-3] was developed for the measurement of dielectric properties of planar slabs of lossy ceramic and composite materials; while cavity or perturbation techniques [I-4] have been used for low-loss materials on the resonance frequency. Although these techniques provide accurate values in this case, it is not suitable for high-loss material characterization. Broadband measurement of complex permittivity and permeability for high-loss material are determined by making use of the transmission/reflection method [I-5] and transmission line method [I-6]. Except the traditional measurement methods, artificial neuronal network (ANN) [I-7] for complex structures, containing a transition part, has been developed based on the coaxial open-ended waveguide. And the dynamic measurement of complex dielectric properties at high temperature (up to ~1000 °C) has been developed [I-8] in a dual mode cylindrical cavity. The choice of optimal technique and resulting measurement uncertainties depends critically on the type of bulk solid to be characterized. Recently, artificial constructed materials [I-9] have become of considerable interest because of its electromagnetic characteristics unlike those of any conventional materials.

For each case one or more techniques may be used depending on the experimental setup. In most case direct relations do not exist between measured parameters and electric properties, so the extraction of either permittivity or permeability will be taken by inverse modelling based essentially on efficient and accurate fullwave electromagnetic analysis of electric properties measurement cell.

I.1.1 Electromagnetic properties of material

The knowledge of material properties is a key point in most industrial or scientific applications, which need to be characterized by measurement methods in different frequency ranges including radio frequency (RF) or microwave range. Among all physic parameters the most important are complex permittivity and complex permeability.

The complex permittivity consists of dielectric constant (ε'), which counts for the ability of material to store energy, and dielectric loss (ε'' being positive), which indicates the ability to convert absorbed energy into heat, in the expression of $\varepsilon = \varepsilon' - j\varepsilon''$. The loss factor ($\tan\delta = \varepsilon''/\varepsilon'$) that affects heat distribution is one of the important properties, which is seen to be the ratio of the imaginary to the real part of complex permittivity. Microwave isotropic materials are usually characterized by the real relative permittivity, ε_r, with $\varepsilon'=\varepsilon_r\varepsilon_0$, ε_0 being the vacuum permittivity, and the loss tangent at a certain frequency, in the expression as $\varepsilon = \varepsilon_r\varepsilon_0(1 - j\tan\delta)$.

The complex permeability of the medium is expressed by $\mu = \mu' - j\mu''$, the imaginary part μ'' accounts for loss due to damping forces. The relative permeability, μ_r, with $\mu'=\mu_r\mu_0$, when μ_0 is the vacuum permeability.

The permittivity defines the relation between an electric field in a material and the induced electric polarization. For isotropic materials, the polarization is in the same direction than the external electric field and its magnitude does not vary with the orientation of electric field. Then the permittivity will be a scalar number for a given frequency. For isotropic magnetic material the permeability is also a scalar number. However there exist a certain number of materials which are anisotropic and their permittivity and permeability are expressed in tensor form as the following

$$[\varepsilon]=\begin{bmatrix}\varepsilon_{xx} & \varepsilon_{xy} & \varepsilon_{xz}\\ \varepsilon_{yx} & \varepsilon_{yy} & \varepsilon_{yz}\\ \varepsilon_{zx} & \varepsilon_{zy} & \varepsilon_{zz}\end{bmatrix} \text{ and } [\mu]=\begin{bmatrix}\mu_{xx} & \mu_{xy} & \mu_{xz}\\ \mu_{yx} & \mu_{yy} & \mu_{yz}\\ \mu_{zx} & \mu_{zy} & \mu_{zz}\end{bmatrix}.$$

Any dielectric materials can exist in solids, liquids, or gases states, depending on its temperature and pressure conditions. In our case we are only interested by studying solid material in atmosphere pressure at room temperature.

I.1.2 Measurement method

In RF and microwave range the material characterization implies the choice of measurement methods. The most used ones can be classified as non-resonant methods and resonant methods. Non-resonant methods are often used to get a general knowledge of electromagnetic properties over a wide frequency range, while resonant methods are used to get accurate knowledge at single frequency or several discrete frequencies. Non-resonant methods and resonant method are complementary each other, and often combined to obtain more accurate knowledge of material properties.

We will introduce shortly these two kinds of measurement methods.

- *Resonant methods*

With these methods we can consider the measurement cell as a generalized resonant circuit, often materialized by a resonant cavity. The frequencies of resonance and the quality factor associated with each resonant frequency are two quantities which can be determined with usual microwave measurement instrument such like vector network analyser (VNA). If metallic cavity is used the quality factor may be very high, leading to very accurate determination of resonant frequencies in a discrete set of frequencies. The accuracy will be less with planar resonators as the quality factor will be much less. When high loss material is considered, depending on the sample size, the resonance may completely be vanished. That is why this kind of methods is not suitable for high loss material measurement.

When the sample occupy only a very small portion of the cavity volume, the electromagnetic field will be mainly determined by that of the unloaded cavity with both resonant frequencies and quality factors are known. The introduction of small size sample gives rise on only small shift of resonant frequencies with decreased quality factor. We say that there is small perturbation of the electromagnetic field which causes the small changes of our two measurable quantities. The inverse modelling will be easy and simpler since reasonably good approximation can be obtained with formal expressions.

- *Non-resonant methods*

With the non-resonant methods, the properties of materials are fundamentally deduced from the characteristic impedance and wave velocities of a guiding structure filled with materials to be measured. When an electromagnetic wave propagates from one structure to another, both the characteristic wave impedance and wave velocity change, resulting in a partial reflection of the electromagnetic wave from the interface between two structures filled with different materials. Measurement of the reflection and transmission can provide information from which the deduction of the permittivity and permeability relationships will be taken. Non-resonant methods mainly include reflection methods and transmission/reflection methods which will be discussed later for our work.

Reflection methods. In the reflection method, the properties of a sample are obtained from the reflection due to a discontinuity between a known guiding structure (transmission line or waveguide) and a space containing the material sample. This space may be a half free space, a resonant cavity or another guiding structure filled fully or partially with the sample under test. This space will be modelled as a one port with its equivalent impedance which is a function of material permittivity and permeability.

Transmission/reflection methods. In a transmission/reflection method both input and output ports are known guiding structures, and the sample under test is placed in another guiding structure. The permittivity and permeability of the sample are derived from the reflection and transmission measurement of entire measurement cell.

I.1.3 Measurement cells

As discussed in the above section in microwave and RF frequency range the electric parameters which can be measured easily are: resonant frequencies, quality factor, and scattering parameters including reflection and transmission coefficient related to the fundamental mode of a known guiding structure. Then the measurement cell utilizes mostly transmission line including coaxial one and planar one, rectangular waveguide, and all kinds of resonator (planar, metallic cavity or dielectric resonator).

In this work we are interested by wideband permittivity and permeability for some moderately or highly lossy materials. For its facilities of fabrication, we will work with coaxial line and microstrip line based measurement cells. When using coaxial cells both reflected method and reflexion/transmission method will be considered. In the microstrip line based study only reflexion/transmission method will be used.

I.2 NUMERICAL ELECTROMAGNETICS

The characterization of material properties from measured parameters mainly includes two steps: direct problem and inverse problem. In the direct problem accurate electromagnetic analysis will be taken on a given measurement cell in which estimated values of permittivity and permeability will be used, leading to the complete solution of Maxwell’s equation with fixed boundary conditions. From the field solution of Maxwell’s equation all physic parameters such as resonant frequencies, quality factors, reflection and transmission coefficient can be deduced by using post processing techniques. All these are function of trial permittivity and permeability value at a given frequency.

Due to the complicity of measurement cells, no analytical expression is available for solution of Maxwell’s equations. Numerical techniques will be used to obtain approximate solutions.

Numerical techniques have been essentially elaborated in considerable detail in the books edited by Ttoh [I-10], Sorrentino [I-11]. The origin of the method can be acquired in the early work on microwave network theory of Montgomery [I-12] and Marcuvitz [I-13]. Altschuler and Goldstone [I-14] developed network representations of class obstacles in waveguide regions when the diffraction problem is of a vector type can be obtained by use of E/H-type modes. A transverse-network representation for hybrid modes in inhomogeneously filled waveguide is derived in the work of Clarricoats and Oliner [I-15] which showed that hybrid modes may be represented by a pair of coupled radial-line modes of pure E and H type. Later a generalized derivation of the transverse field equations is described in the book edited by Felsen and Marcuvitz [I-16] and explained the modal representations of the electromagnetic field in transverse inhomogeneous region. In addition, a method is described of K. Solbach and I. Wolff [I-17] for the exact calculation of the field distributions and the phase constants of single and coupled dielectric image lines of rectangular cross section. R. Mittra [I-18] presented the computation of the propagation constants and field distribution of an inverted strip dielectric waveguide by mode-matching technique. Masterman and Clarricoats [I-19] described a computational method to settle a series of transverse waveguide discontinuity problems and showed that the solution is found to be sensitive to the number of truncated field functions. Rozzi [I-20] proposed the variational method described by Collin [I-21] and extended into more than one interacting discontinuity in the irises in a homogeneous uniform waveguide and also has been applied to the inhomogeneous cases [I-22]. The transverse operator method is used to calculate the propagation constants for the multi-layered guiding structures [I-23], and the description of field distribution makes the trial functions of the field expansion series in the discontinuity analysis.The transverse resonance method was introduced for characterizing finline discontinuities [I-24], stripline discontinuities [I-25], and quasi-planar structure [I-26] in a rigorous manner which had a great advantage of a substantial reduction of computer time. Multimodal variational method [I-27] is proposed to elaborate a formulation of uniaxial cascaded waveguide discontinuities, assemble diffraction matrix is obtained by carrying out the chaining of the scattering matrix of individual discontinuity, equated to multipoles and separated by waveguide section of length d_n equal to the distance between two discontinuities.

I.2.1 Spatial discretization based method

The complexity of wave guiding structures makes the analytical solution to Maxwell's equations intractable, therefore, numerical method come into prominence and become more attractive along with the advent of computer. To convert differential or integral equations to linear equations system the unknown electromagnetic field will be expressed as linear combination of a set of known mathematic function of scalar or vector type. When this approximation is taken by subdividing the entire region to a great number of small subregion the method can be called spatial discretization based one. This is the case for most commercial solvers, i.e., Ansoft HFSS, COMSOL Multiphysics, and CST Microwave studio.

The three most commonly used full wave methods in electromagnetics are introduced such as (1) method of moment, (2) finite-difference time-domain method and (3) finite element method. Most electromagnetic problems involve either partial differential equations or integral equations. Partial differential equations are usually solved using the finite difference method or finite element method; integral equations are solved conveniently using the moment method.

➢ Method of Moment

The moment method or the method of moments (MoM) [I-28] is used for solving linear partial differential equations which have been formulated as integral equations (i.e., in boundary integral form). Because it requires calculating only boundary values, rather than values throughout the space, it is significantly more efficient in terms of computational resources for problems with a small surface/volume ratio. Conceptually, it works by constructing a "mesh" over the modelled surface.

However MoM is significantly computationally less efficient than volume-discretization methods (finite element method, finite difference method, finite volume method) for many problems. Boundary element formulations typically give rise to fully populated matrices. This means that storage requirements and computational time will tend to grow in peace with the square of the problem size. By contrast, finite element matrices are typically banded (elements are only locally connected) and the storage requirements for the system matrices typically grow linearly with the problem size.

➢ Finite-Difference Time-Domain Method

Finite-difference time-domain method is a technique that Maxwell's time-dependent electromagnetic curl equations are replaced by differential equations. It is also called Yee's method [I-29], named after the Chinese American applied mathematician Kane S. Yee. His method has been used to solve numerous scattering problems on microwave circuits, dielectrics, and electromagnetic absorption in biological tissue at microwave frequency.

Initially there was little interest in the FDTD method, probably due to a lack of sufficient computing resourced. However, with the advent of powerful computers and advance to the method itself, the FDTD technique has become a popular method for solving electromagnetic problems. The mathematical pre-processing is minimal, and the method can be applied to a wide range of structures including those with odd shapes. A price one has to pay is numerical inefficiency. Certain precautions have to be taken into consideration when the method is utilized for an open-region problem in which the region is truncated to a finite size. Also, the method requires that the mesh points lie on the boundary.

- **Finite Element Method**

The finite element method is similar to the finite difference method. However, it has variational features in the algorithm and contains several flexible features. In the finite element method, instead of the partial differential equations with boundary conditions, variational expressions are applied to each of the small areas or volumes subdividing the region of interest. Usually these small segments are polygon such as triangles and rectangles for two-dimensional problems and tetrahedral elements for three-dimensional problems. The finite element method formulation of the problem results in a system of algebraic equations. The method yields approximate values of the unknowns at discrete number of points over the domain. To solve the problem, it subdivides a large problem into smaller, simpler parts that are called finite elements. The simple equations that model these finite elements are then assembled into needs to be exercised when the finite element method is applied to an open-region problem such as dielectric waveguide circuit.

Table.1.1. Simulation Software in EM.

Name	License	Algorithm	Area of application
COMSOL Multiphysics	Commercial	FEM, Boundary element method, Ray Tracing	General purpose
HFSS	Commercial	FEM, FDTD, MoM, Hybrid FEBI, Eigen Mode	A broad range of applications including antennas, phased arrays, passive RF/MW components, high-speed interconnects, connectors, IC packaging and PCBs.
CST	Commercial	FEM	A wide range of EM simulation software to address design challenges across the electromagnetic spectrum, from static and low frequency to microwave and RF, for a range of applications, including EDA & electronics, EMC & EMI and charged particle dynamics.
Momentum	Commercial	MoM	For passive planar elements development, integrated into Agilent EEsof Advanced Design System.
NEC	Open source	MoM	Widely used as the basis for many GUI-based programs on many platforms.

There are many commercial simulators available for electromagnetic modelling on the market, the effectiveness of which has been proven in many varied applications based on the numerical full wave methods. The list of notable software packages is nominal EM (electromagnetic) simulators in Table.1.1.

I.2.2 Eigenmodes based methods

In the commercial software simulations, spatial discretisation of complex configurations consumes computer memory and solving the equations takes considerable time. Large scale computational problems face the memory requirement and time-consuming for high performance and accuracy. As the inverse modelling requires generally a great number of direct analysis before convergent results be obtained, numerical efficiency becomes a key criterion. The development of specific tools with increasing numerical performance is the objective of most eigenmodes based methods.

Many modal analysis techniques [I-30], including transverse operator method, transverse resonance method, mode matching method and multimodal variational method, are now applied to microwave and millimeter-wave circuit structures to describe the stratified cross-sections and uniaxial conjunctions in our research. The design software of hybrid techniques can be built into one package, just like the other electromagnetic modelling methods are developed by university researchers for complex structures with several advantages.

- ✓ More manageable
- ✓ Targeted-oriented

Knowledge of the capabilities and limitations of these numerical algorithms leads to a better understanding of their impact on various applications, and points the way to further research. A brief description of these method which will be used in our research is as follow.

- ➢ **Transverse operator method (TOM)**

Transverse operator method concentrates on eliminating the longitudinal components from Maxwell’s equation and resolving the propagation constants by developing the transverse fields in series of modes of a closed structure. It is useful for the stratified guiding structures, by making use of the orthogonality relation, eliminating the longitudinal components, which is normal to the interfaces of two different media, the Maxwell's equation is simplified into "four-vector" equation matrix with a transverse operator. Based on the different structures, such as coaxial cell in cylindrical coordinate or microstrip line in Cartesian coordinate, the transverse operator can be rearranged and leads to the resolution of the eigenvalue problems simultaneously including the fundamental and higher-order modes by the determination of matrix being zero.

➢ Transverse resonance method (TRT)

Transverse resonance method is the technique we apply resonance condition along a transverse direction (transverse with respect to the main propagation direction). Since the fields form standing waves in the transverse plane of the waveguide at the cut off frequency, as can be inferred from "bouncing plane wave" interpretation of waveguide modes, it can be modelled with the equivalent transmission lines operating at resonant frequency.

This method in two-dimensional analysis can be used to calculate various important quantities, wavenumbers for complicated wave guiding structures (dielectric-loaded guides, surface wave, etc.), and resonance frequencies of resonant cavities (resonators), which permits us to obtain the transverse equivalent network in the view of wave propagation in the waveguide filled with a dielectric slab. The transverse resonance technique employs a transmission line model of the transverse cross section of the waveguide and gives a much simpler and more direct solution for the cut off frequency. If the attenuation is taken into consideration, the complete field equations will be employed for more information. This method in three-dimensional analysis is an extension of a classical one, similar to the mode matching method and is suitable for characterization of the discontinuity in a planar transmission line.

➢ Mode matching method (MMM)

The mode matching method is typically applied to the problem of scattering at the discontinuity in the waveguide. The field on both sides of the discontinuity are expanded in terms of the modes in respective waveguide regions with unknown field coefficients. After the boundary conditions are applied at the discontinuity, the orthogonality relationship of the modes is invoked to generate a set of linear simultaneous equations in which the unknown are the field coefficient which are subsequently solved by matrix inversion.

The first step in this method is to subdivide the waveguide cross section into segments in such a way that in each segment the fields can be conveniently expanded into series. The boundary conditions are applied at each interface between segments. By invoking the orthogonality of the expansion functions, a homogeneous set of linear equation is derived. A value of the propagation constant is sought that makes the determination of this system of equation zero.

➢ Multimodal variational method (MVM)

Multimodal variational method is used to characterize the cascaded discontinuities in homogenous and inhomogeneous structures. This technique, similar to the general scattering matrix method, combines the mutual interactions of cascaded discontinuities by way of fundamental and high-order modes. As in most modal decomposition techniques, an important factor for obtaining accurate results is the choice of the size of the S matrix for each discontinuity, In the MVM case, by taking a certain number of "accessible" modes on either side of the discontinuity, the convergence study is as a function of accessible modes.

Besides the fullwave methods described above, a number of other numerical methods exist, such as spectral domain method, transmission line matrix method, and general scattering matrix method, etc. The use of one method or another, depends on the studied structure and the frequency domain, the ease of implementation, the available computer means and the desired accuracy.

For all analysis results obtained from our specific numerical program, comparisons have been effectuated in this work with commercial software, such as HFSS and COMSOL, before its use in inverse modelling during electric properties extraction.

I.3 CONCLUSION

This thesis is a contribution to the numerical modelling and characterization of passive microwave devices, with transverse and uniaxial discontinuities, in enlarged coaxial cell and microstrip line based cell, to extract electric properties of materials at RF and microwave frequencies. The development of material properties characterization is based on the inverse modelling procedure by microwave measurement methods, and the direct analysis for the complicated test structures is the focus and will be treated at a greater length in coverage by numerical electromagnetic methods.

- Chapter II will present the characterization of the propagation constants of fundamental and high-order modes in the multi-layered structures by transverse operator method and transverse resonance method.

- Chapter III will elaborate the scattering parameters analysis of the simple and cascaded discontinuities by mode matching and multimodal variational methods respectively, in coaxial type dielectric measurement cell, and the multimodal variational analysis for planar transmission line based measurement cell.

- Chapter IV will illustrate the inverse modelling for complex permittivity and complex permeability measurement by two measurement cells, and by using specific theoretical tools developed in the preceding two chapters.

References of chapter I

[I-1]. L. F. Chen, et al. Microwave electronics: measurement and materials characterization. John Wiley & Sons, 2004.

[I-2]. J. Baker-Jarvis, et al, Measuring the permittivity and permeability of lossy materials: Solids, liquids, metals, building materials and negative-index materials, 2005.

[I-3]. D. K. Ghodgaonkar, V. V. Vasundara and K. V. Vijay. "A free-space method for measurement of dielectric constants and loss tangents at microwave frequencies." IEEE Transactions on Instrumentation and measurement 38.3 (1989): 789-793.

[I-4]. A. J. Canos, et al. "A novel technique for deembedding the unloaded resonance frequency from measurements of microwave cavities." IEEE transactions on microwave theory and techniques54.8 (2006): 3407-3416.

[I-5]. Baker-Jarvis, James, Eric J. Vanzura, and William A. Kissick. "Improved technique for determining complex permittivity with the transmission/reflection method." IEEE Transactions on microwave theory and techniques 38.8 (1990): 1096-1103.

[I-6]. M. E. Requena-Pérez, et al. "Combined use of genetic algorithms and gradient descent optimization methods for accurate inverse permittivity measurement." IEEE Transactions on Microwave Theory and Techniques 54.2 (2006): 615-624.

[I-7]. M. M. El Afendi, Tellache, J.W. Tao, B. Hadjadji, & M. Benmimoune, (2017). Dielectric characterization using FEM modeling and ANNs for coaxial waveguide with conical open-ended radiation. International Journal of Microwave and Wireless Technologies, 9(3), 523-534.

[I-8]. J. M. Catalá-Civera, et al. "Dynamic measurement of dielectric properties of materials at high temperature during microwave heating in a dual mode cylindrical cavity." IEEE Transactions on Microwave Theory and Techniques 63.9 (2015): 2905-2914.

[I-9]. Smith, David R., John B. Pendry, and Mike CK Wiltshire. "Metamaterials and negative refractive index." *Science* 305.5685 (2004): 788-792.

[I-10]. T. Itoh, Ed., Numerical Techniques for Microwave and Millimetre-wave Passive Structures, New York: John Wiley and Sons, 1989.

[I-11]. R. Sorrentino, Ed., Numerical Methods for Passive Microwave and Millimetre Structures, New York: IEEE Press, 1989.

[I-12]. C. G. Montgomery, R. H. Dick, and E. M. Purcell, Ed., Princinples of Microwave Circuits, New York: McCraw-Hill, 1948.

[I-13]. N. Marcuvitz, Waveguide Handbook, New York: McCraw-Hill, 1951.

[I-14]. H. M. Altschuler and L. O. Goldstone, " One network representations of certain network obstacles in waveguide regions," IRE Trans. Microwave Theory Tech., vol. MTT-7, pp: 213-221, Apr. 1959.

[I-15]. P. J. B. Clarricoats and A. A. Oliner, "Transverse-network representation for inhomogeneously filled circular waveguides," Proc. Inst. Electr. Eng., vol. 112, pp: 883-894, May 1965.

[I-16]. L. B. Felsen and N. Marcuvitz, Radiation and Scattering of Waves, Englewood Cliffs, N. J.: Prentice-Hall, 1973.

[I-17]. K. Solbach and I. Wolff, "The Electromagnetic Fields and the Phase Constants of Dielectric Image Lines," IEEE Trans. Microwave Theory Tech., vol. MTT-26, pp: 266-274, Apr. 1978.

[I-18]. R. Mittra, Y. Hou and V. Jamnejad, "Analysis of Open Dielectric Waveguides Using Mode-Matching Technique and Variational Methods," IEEE Trans. Microwave Theory Tech., vol. MTT-28, pp:36-43, Jan. 1980.

[I-19]. P. H. Masterman and P. J. B. Clarricoats, "Computer field-matching solution of waveguide transverse discontinuities," Proceeding of the IEE, vol. 118, pp:51-63, Jan. 1971.

[I-20]. T. E. Rozzi, “The variational treatment of thick interacting inductive irises,” IEEE Trans. Microwarle Theory Tech., vol. MTT-21, pp: 82-88, Feb. 1973.

[I-21]. R. E. Collin, Field Theory of Guide Waves, New York: McGraw-Hill, 1960.

[I-22]. P. Couffignal et al., “A multimodal variational approach for the characterization of waveguide discontinuities for microwave filter design,” Proc. 20th European Microwave Conference. (Buda-pest), pp: 919-924, 1990.

[I-23]. Tao, J-W., et al. "Transverse operator study of a large class of multidielectric waveguides." IEE Proceedings H (Microwaves, Antennas and Propagation). Vol. 137. No. 5. IET Digital Library, 1990.

[I-24]. R. Sorrentino and T. Itoh, "Transverse resonance analysis of finline discontinuities," IEEE Trans. Microwave Theory Tech., vol. MTT-324, pp:1663-1638, Jan. 1984.

[I-25]. T. Uwano, R. Sorrentino, and T. Itoh. "Characterization of strip line crossing by transverse resonance analysis," IEEE Trans Microwave Theory Tech., vol. MTT-35, no.12, pp: 1369-1376, 1987.

[I-26]. J. Tao and H. Baudraud, "A modified transverse resonance method for the analysis of multilayered, multiconductor quasi-planar structures with finite conductor thickness and mounting grooves," IEEE Trans. Microwave Theory Tech., vol. 40, pp: 1966-1970, Oct. 1992.

[I-27]. J. Tao and H. Baudrand, "Multimodel variational analysis of uniaxial waveguide discontinuities," IEEE Trans. Microwave Theory Tech., vol. 39 pp: 506-516, Mar. 1991.

[I-28]. R. F. Harrington, Field computation by moment methods, IEEE Press, 1993.

[I-29]. K. S. Yee, "Numerical solutions of initial boundary value problem involving Maxwell's equations in isotropic media," IEEE Trans. Antenna and Propagation, vol. AP-14, pp: 302-307, 1966.

[I-30]. A. Wexler, "Solution of waveguide discontinuities by modal analysis," IEEE Trans on Microwave Theory and Tech, vol.15, no.9, pp: 508-517, 1967.

Chapter II EIGENVALUE ANALYSIS IN GUIDING STRUCTURES

Dielectric material measurement cells in RF and microwave range often make use of wave propagation or wave resonance. As a result, different propagation structures are key elements of these measurement systems. The direct electromagnetic analysis of these cells by modal methods requires the basic modal knowledge of electromagnetic theory [II-1] in these stratified structures [II-2]. In terms of mathematical formulation, we are dealing with the following eigenvalue equation:

$$\mathcal{L}\Phi = \lambda\Phi \tag{2.1}$$

Here $\mathcal{L}$ is a differential operator and Φ being a physical quantity of electromagnetic solution. Most often they are electric or magnetic fields or combinations of both.

In this chapter we will study two structures: the enlarged coaxial cell partially filled with dielectric layers in annular form, and the planar cell with multilayer substrates on both sides of the metallization layer. The search for the modal base for each structure will be the subject of the following sections.

II.1 EIGENVALUE ANALYSIS OF PARTIALLY FILLED COAXIAL STRUCTURE

Fig.2.1 shows a cross section of multilayered coaxial structure. Each layer is one kind of materials in the form of a ring, characterized by its permittivity and its permeability in tensor form for more generality.

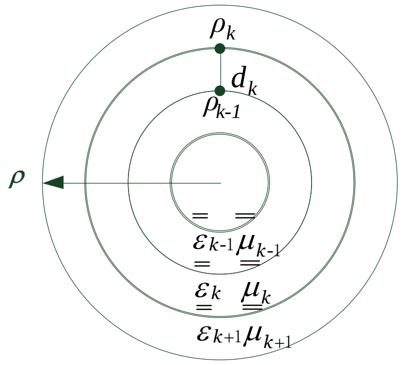

Fig.2.1. Geometry of stratified structures in cylindrical coordinate.

The transverse operator method was chosen for the formulation of the eigenvalue equation for this structure. After a description of the method adapted to this type of structure, numerical applications will be effectuated and compared to the results of simulations obtained with several commercial software.

II.1.1 Theoretical Formulation

Transverse operator method has been successfully applied to propagation problems in [II-3] and [II-4] or magnetic multi-dielectric structures [II-5] and [II-6], as well as to some radiation problem [II-7]. The starting equation is a rearrangement of Maxwell's equations of " four-vector" modes proposed by Marcuvitz [II-8] in the following form:

$$\overline{\overline{\mathcal{L}}}\cdot\Phi = j\cdot\eta\cdot\partial_l\Phi \qquad (2.2)$$

$\overline{\overline{\mathcal{L}}}$ is the transverse operator defined by

$$\overline{\overline{\mathcal{L}}} = \begin{bmatrix} k_0\overline{\overline{\varepsilon}}_E - \frac{1}{k_0}\partial_t\left(\frac{1}{\mu_{ll}}\partial_t^+\right) & -\frac{\overline{\varepsilon}_{tl}}{\varepsilon_{ll}}\partial_t^+ - \partial_t\frac{\overline{\mu}_{lt}}{\mu_{ll}} \\ -\frac{\overline{\mu}_{tl}}{\mu_{ll}}\partial_t^+ - \partial_t\frac{\overline{\varepsilon}_{lt}}{\varepsilon_{ll}} & k_0\overline{\overline{\mu}}_E - \frac{1}{k_0}\partial_t\left(\frac{1}{\varepsilon_{ll}}\partial_t^+\right) \end{bmatrix}$$

with $\eta = \begin{bmatrix} 0 & \eta_0 \\ \eta_0 & 0 \end{bmatrix}$ and $\eta_0 = \begin{bmatrix} 0 & -j \\ j & 0 \end{bmatrix}$.

In transverse operator formation $\overline{\overline{\mathcal{L}}}$, $\Phi = \left[E_t \quad H_t'\right]'$, where $H_t' = -jz_0H_t$, denotes the transverse field vectors, $k_0 = \omega_0\sqrt{\mu_0\varepsilon_0}$ and $z_0 = \sqrt{\mu_0/\varepsilon_0}$ are, respectively, the propagation constant and characteristic impedance in the free space. ∂_t is the transverse curl operator with its adjoint operator ∂_t^+, ∂_l is the longitudinal derivative operator normal to slab interfaces. We consider a guiding structure which comprises media characterized by their relative tensor permittivity and permeability.

$$\overline{\overline{\varepsilon}} = \begin{bmatrix} \overline{\overline{\varepsilon}}_t & \overline{\varepsilon}_{tl} \\ \overline{\varepsilon}_{lt} & \varepsilon_{ll} \end{bmatrix}; \quad \overline{\overline{\mu}} = \begin{bmatrix} \overline{\overline{\mu}}_t & \overline{\mu}_{tl} \\ \overline{\mu}_{lt} & \mu_{ll} \end{bmatrix}$$

And the relative permittivity and permeability tensor in each layer will be given by the following complex matrices:

$$\overline{\overline{\varepsilon}}_E = \overline{\overline{\varepsilon}}_t - \frac{\overline{\varepsilon}_{tl}\overline{\varepsilon}_{lt}}{\varepsilon_{ll}} \qquad \overline{\overline{\mu}}_E = \overline{\overline{\mu}}_t - \frac{\overline{\mu}_{tl}\overline{\mu}_{lt}}{\mu_{ll}}$$

By applying the relationship between$\eta\eta_0$ and η, one can yield the following equation

$$-j\cdot\eta\cdot\overline{\overline{\mathcal{L}}}\cdot\Phi = \partial_l\Phi \tag{2.3}$$

The formulation for a coaxial structure will be developed in cylindrical coordinates. Taking the *z*-axis direction as the propagating direction, the propagation factor $e^{-\gamma z}$ is assumed. And taking the tangential interfaces normal to ρ -direction, for non-ferrite guiding structure (e. g., coaxial cell) with transverse inhomogeneity and isotropy, the relative permittivity and permeability of each medium filled in the structure will be scalar (diagonal tensors) $\mu = \mu_0\,\mu_r$ and $\varepsilon = \varepsilon_0\,\varepsilon_r$. Consider the only φ-independent solutions which match with the measurement cell's feeding condition, the transverse curl operators and longitudinal derivative operator become

$$\partial_t = \begin{bmatrix} -\gamma \\ 0 \end{bmatrix},\ \partial_t^{+} = \begin{bmatrix} \gamma & 0 \end{bmatrix},\ \partial_l = \partial_\rho + \frac{1}{\rho}\begin{pmatrix} 1 & 0 & 0 & 0 \\ 0 & 0 & 0 & 0 \\ 0 & 0 & 1 & 0 \\ 0 & 0 & 0 & 0 \end{pmatrix}.$$

Solution of transverse operator in polar coordinates will be presented in the Appendix I-i. Then the transverse operator can be written as a diagonal matrix

$$\overline{\overline{\mathcal{L}}} = \begin{bmatrix} k_{\varepsilon r} & 0 & 0 & 0 \\ 0 & k_\varepsilon & 0 & 0 \\ 0 & 0 & k_{\mu r} & 0 \\ 0 & 0 & 0 & k_\mu \end{bmatrix} \tag{2.4}$$

For computation convenience, all the four transverse field components are converted in different order which is expressed as

$$\Phi_t = \begin{bmatrix} E_t & H_t{}' \end{bmatrix}' = \begin{bmatrix} e_\varphi & e_z & h_\varphi^{'} & h_z^{'} \end{bmatrix}' \Leftrightarrow \Phi_t = \begin{bmatrix} \Phi_\varphi & \Phi_z \end{bmatrix}' = \begin{bmatrix} e_\varphi & h_\varphi^{'} & e_z & h_z^{'} \end{bmatrix}'$$

Because of the differential matrix equation (2.3), the matrix $\overline{\overline{L}}$ can be expressed as

$\overline{\overline{L}} = -j\eta\overline{\overline{\mathcal{L}}}$. The transverse operator $\overline{\overline{L}}$ can be reorganized as

$$\overline{\overline{L}} = \begin{bmatrix} 0 & \overline{\overline{L}}_{12} \\ \overline{\overline{L}}_{21} & 0 \end{bmatrix} = \begin{bmatrix} 0 & 0 & 0 & -k_{\mu} \\ 0 & 0 & -k_{\varepsilon} & 0 \\ 0 & k_{\mu r} & 0 & 0 \\ k_{\varepsilon r} & 0 & 0 & 0 \end{bmatrix}$$

With $\overline{\overline{L}}_{12} = \begin{bmatrix} 0 & -k_0\mu_r \\ -k_0\varepsilon_r & 0 \end{bmatrix}$, $\overline{\overline{L}}_{21} = \begin{bmatrix} 0 & k_0\mu_r + \gamma^2/k_0\varepsilon_r \\ k_0\varepsilon_r + \gamma^2/k_0\mu_r & 0 \end{bmatrix}$.

According to the defined transverse operator and the given conditions, the formulation of transverse operator equations can be divided into two coupled equations:

$$\overline{\overline{L}}_{12}\Phi_z = \frac{1}{\rho}\partial_\rho \rho \Phi_\varphi \qquad \overline{\overline{L}}_{21}\Phi_\rho = \partial_\rho \Phi_z$$

Two differential matrix equations in terms of Φ_z can be obtained in the following form

$$\left(\rho^2\partial_\rho^2\overline{\overline{I}} + \rho\partial_\rho\overline{\overline{I}} + \rho^2\overline{\overline{P}}\right)\Phi_z = 0 \tag{2.5}$$

with $\overline{\overline{P}} = -\overline{\overline{L}}_{21}\overline{\overline{L}}_{12} = \begin{bmatrix} \lambda & 0 \\ 0 & \lambda \end{bmatrix}$.

The direct solution to the differential equation (2.5) is given by

$$\Phi_z(\rho) = J_0\left(\overline{\overline{P}}^{\frac{1}{2}}\rho\right)\overline{C}_1 + Y_0\left(\overline{\overline{P}}^{\frac{1}{2}}\rho\right)\overline{C}_2 = \overline{\overline{K}}^{21}\overline{C}_1 + \overline{\overline{K}}^{22}\overline{C}_2 \tag{2.6}$$

$$\Phi_\varphi(\rho) = \overline{\overline{L}}_{21}^{-1}.\partial_\rho.\Phi_z(\rho) = \overline{\overline{K}}^{11}\overline{C}_1 + \overline{\overline{K}}^{12}\overline{C}_2 \tag{2.7}$$

with $\overline{\overline{L}}_{21}^{-1} = \begin{bmatrix} 0 & 1/k_{\varepsilon r} \\ 1/k_{\mu r} & 0 \end{bmatrix}$

in which J_0 and Y_0 are Bessel functions of first kind and Bessel function of second kind (Neumann function) of the 0th order. From the solution equations (2.6) and (2.7), it will be rewritten in the form of matrix as follows

$$\begin{bmatrix} \Phi_\varphi(\rho) \\ \Phi_z(\rho) \end{bmatrix} = \overline{\overline{K}} \begin{bmatrix} \bar{C}_1 \\ \bar{C}_2 \end{bmatrix} \tag{2.8}$$

in which the development of matrix K will be defined in the Appendix I-ii. The continuity equations at the interface between the ith and the i+1th layers will be deduced in the following form

$$\begin{bmatrix} \Phi_\varphi \\ \Phi_z \end{bmatrix}^{(i+1)} \left(\rho^{(i)}\right) = \overline{\overline{K}}^{(i+1)} \left(\rho^{(i)}\right) \begin{bmatrix} \bar{C}_1 \\ \bar{C}_2 \end{bmatrix}^{(i+1)} = \begin{bmatrix} \Phi_\varphi \\ \Phi_z \end{bmatrix}^{(i)} \left(\rho^{(i)}\right) = \overline{\overline{K}}^{(i)} \left(\rho^{(i)}\right) \begin{bmatrix} \bar{C}_1 \\ \bar{C}_2 \end{bmatrix}^{(i)} \tag{2.9}$$

For the definition of relations between Φ and C, we will make use of the boundary condition at the external interface of the outer conductor or internal interface if there is e.g., coaxial cell. And the C is the four elements unknown vectors defined by the boundary conditions to determine the characteristic equation.

II.1.2 Axisymmetric solution in cylindrical coordinates

Due to the azimuthal symmetry in cylindrical coordinates shown in Fig.2.2, only φ-independent solution will be considered and z-direction is identified as that of the propagation direction with its propagating factor $e^{-\gamma z}$.

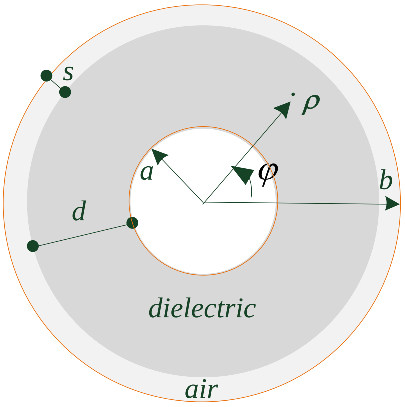

Fig.2.2. Transverse cross section of coaxial cell loaded with toroidal dielectric.

According to equation (2.8), $\overline{\overline{K}}$ is a 4 × 4 transfer matrix, $\begin{bmatrix}\Phi_\varphi & \Phi_z\end{bmatrix}'$ is a column vector with 4 tangential field components, and C is a unknown column vector coefficients. In order to determine the propagation constants of hybrid modes propagating in the guiding structure, to reduce the memory burden and boost the calculation speed, we can transfer the four tangential components into another form given by

$$\begin{bmatrix}\Phi_\varphi & \Phi_z\end{bmatrix}' \Leftrightarrow \begin{bmatrix}\Psi_m & \Psi_e\end{bmatrix}' = \begin{bmatrix} jz_0h_\varphi & e_z & e_\varphi & jz_0h_z\end{bmatrix}'$$

A transfer matrix relating to the $\Psi_m = \begin{bmatrix} jz_0h_\varphi & e_z\end{bmatrix}'$ will be given by

$$\Psi_m\Big|_\rho = \overline{\overline{M}}\begin{bmatrix} d_1 \\ d_2\end{bmatrix} = \begin{bmatrix} \sqrt{\lambda}J_0^{'}\left(\sqrt{\lambda}\rho\right)/k_{\mu r} & \sqrt{\lambda}Y_0^{'}\left(\sqrt{\lambda}\rho\right)/k_{\mu r} \\ J_0\left(\sqrt{\lambda}\rho\right) & Y_0\left(\sqrt{\lambda}\rho\right)\end{bmatrix}\begin{bmatrix} d_1 \\ d_2\end{bmatrix} \tag{2.10}$$

A transfer matrix relating to the $\Psi_e = \begin{bmatrix} e_\varphi & jz_0h_z\end{bmatrix}'$ will be given by

$$\Psi_e\Big|_\rho = \overline{\overline{N}}\begin{bmatrix} d_3 \\ d_4\end{bmatrix} = \begin{bmatrix} \sqrt{\lambda}J_0^{'}\left(\sqrt{\lambda}\rho\right)/k_{\varepsilon r} & \sqrt{\lambda}Y_0^{'}\left(\sqrt{\lambda}\rho\right)/k_{\varepsilon r} \\ J_0\left(\sqrt{\lambda}\rho\right) & Y_0\left(\sqrt{\lambda}\rho\right)\end{bmatrix}\begin{bmatrix} d_3 \\ d_4\end{bmatrix} \tag{2.11}$$

in which matrix M and N are the 2 × 2 matrices, it will be easier and fast to figure out the propagation constants for all the hybrid modes. To find out the solution of the propagation constant, the boundary conditions on the external/internal conductor are applied for the coaxial waveguide, and the propagation constant will be obtained.

At the interface ρ=a, the tangential electric components should be zero for all the modes including fundamental and higher order modes, and the tangential magnetic field will be the maximum which can be normalized to be 1 for the need of eigenvalue research. Specifically, the greatest constant J_{sa} of the magnetic field h_φ or h_z are corresponding to the TEM/TM modes or TE modes. And at the interface ρ=b, the tangential electric components are also zero, same as the inner interface case, it will be useful for the homogeneous equations to be the zero-constant column vector, and the tangential magnetic component is defined as a constant J_{sb}. For continuity at the interface ρ=a+d, the tangential electric and magnetic components are continuous as the relation that the equations display.

At the surface of inner conductor, we will obtain the equation as $\Psi_m\Big|_{(\rho=a)} = \begin{bmatrix} J_{sa} & 0\end{bmatrix}'$.

From which, we can derive the column vector coefficient in term of the transfer matrix and boundary vector of the inner conductor. Then by making use of the continuity at the interface between air and dielectric $\Psi_m\Big|_{(\rho=c)}=\Psi_m\Big|_{(\rho=c+\xi)}$ and the boundary condition at the external conductor $\Psi_m\Big|_{(\rho=b)}=\begin{bmatrix}J_{sb} & 0\end{bmatrix}'$. The solution matrix equation for the TEM/TM modes will be developed in the Appendix I-iii, and the transfer matrix for between two surfaces of inner and external conductors is defined as

$$\overline{\overline{M}}=\overline{\overline{M}}_4\overline{\overline{M}}_3^{-1}\overline{\overline{M}}_2\overline{\overline{M}}_1^{-1} \tag{2.12}$$

The matrix *M* is defined by equation (2.12) deduced from the transverse operator by applying the boundary conditions for good conductor and dielectric interfaces for the two-layered structure. Similarly, for the n-layered stratified guiding structures, the transfer matrix for TEM/TM and TE modes is given by

$$\overline{\overline{M}}=\left(\prod_{i=1}^{2n}\overline{\overline{M}}_{2i}\overline{\overline{M}}_{2i-1}^{-1}\right) \text{ and } \overline{\overline{N}}=\left(\prod_{i=1}^{2n}\overline{\overline{N}}_{2i}\overline{\overline{N}}_{2i-1}^{-1}\right)$$

The trial solution of the solution matrix equation will be given by

$$\det\left(\overline{\overline{M}}_{12}\right)=0 \tag{2.13}$$

In the equivalent way, the trial solution for the TE modes will be given by

$$\det\left(\overline{\overline{N}}_{21}\right)=0 \tag{2.14}$$

II.2 NUMERICAL RESULTS

The transverse operator method is described for the study of different kind of dielectric waveguides in this chapter. The characterization of the multi-dielectric rectangular guiding structures has been obtained in last section and compared with the published results which show a good agreement. This section we will consider multi-layered coaxial cell filled with lossless dielectrics or high-loss samples.

II.2.1 Propagation constants in lossless case

A two layers structure shown in Fig.2.3 will be studied, with the coaxial cell of the inner and outer radius, respectively, $a=6mm$ and $b=20mm$, are filled with dielectric layer of thickness $d = 10mm$ and dielectric constant ε_r=16. And air layer has thickness of 4mm.

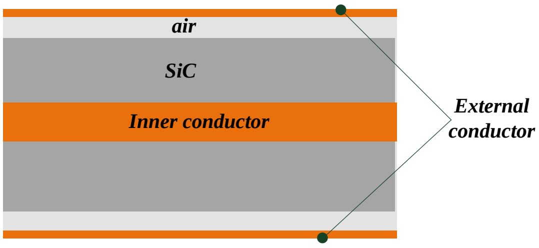

Fig.2.3. Longitudinal cross section of coaxial cell loaded with dielectric.

In Fig.2.4, our theoretical results are compared to that obtained by finite element method from HFSS. Good agreement can be observed for the dispersion characteristic for lossless two-layered structure over a brand frequency range from 0.5 to 4 GHz. In Fig.2.4, we verified the phase constant for the dominant mode in the coaxial cell when it is partially filled with lossless ceramic sample. Then also the propagation constant for higher order modes which are illustrated in Fig.2.5 can be solved by the analytical method and compared the cut-off frequency of eigenmodes with those from COMSOL shown in Table. 2.1.

Table. 2.1. Cutoff Frequency Comparison.

Mode	TOM (GHz)	Comsol (GHz)	Δf /f (%)
TM_{01}	2.7813	2.782112	0.029
TM_{02}	6.09	6.092691	0.044
TM_{03}	9.628	9.653388	0.26
TE_{01}	2.971	2.972124	0.038
TE_{02}	6.205	6.205256	0.004
TE_{03}	9.706	9.71261	0.92

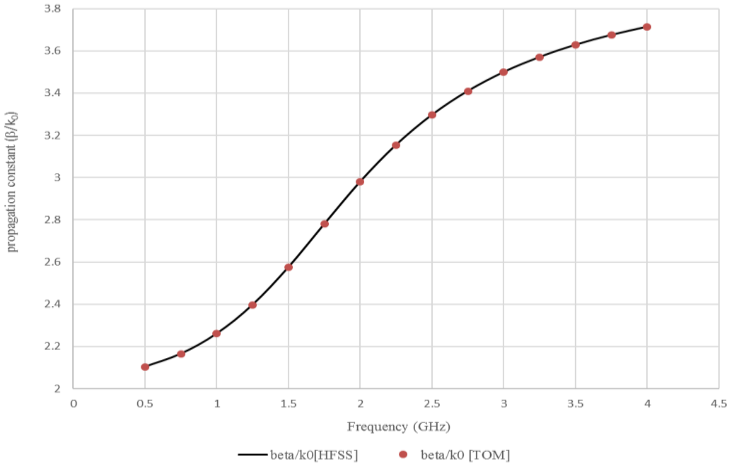

Fig.2.4. Normalized phase constant for quasi-TEM in lossless two-layered coaxial cell, comparison with HFSS simulation.

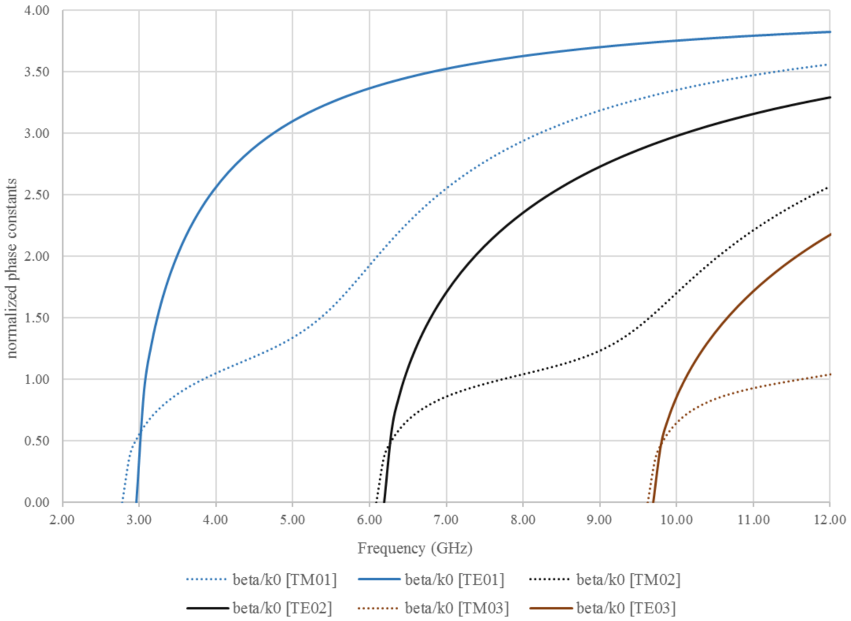

Fig.2.5. Normalized phase constant for higher order mode in lossless two layers coaxial cell. The modes are arranged from left to right TE_{01}, TM_{01}, TE_{02}, TM_{02}, TE_{03}, and TM_{03}.

Except the propagation constants of fundamental and higher order modes in the guiding structure, we can utilize the relation between the tangential filed components and the transfer matrix, by making use of the corresponding propagation constants of each mode as eigenvalues, in the equations (2.13) and (2.14), to obtain the eigenfunctions, which is useful for the discontinuity discussion as a series of basis functions. These normalized field distributions also verified and proved our theoretical analysis.

II.2.2 Propagation constant in the lossy cases

Dielectric materials have been developed and are finding increasing use in the microwave circuits. In one case, it has such small losses that we may analyses their behavior by considering them as ideal lines and then usually make a simple perturbation calculation to obtain the effects. In the other cases, high loss materials shall be most concerned with in the microwave heating applications. The object of this latter part is ultimately to determine the attenuation constant, propagation constant in the nonhomogeneous transmission line.

For a coaxial line, the insulation dielectric between inner and outer conductor is normally the air. Therefore, when we insert the dielectric sample in the enlarged cell of the transverse cross section as shown in Fig.2.2 and longitudinal cross section in

Fig.2.3, the inside space is naturally separated into two layers seen from longitudinal cross section which means that the configuration is the multi-layered structure. In the coaxial cell, besides the fundamental TEM mode, higher order modes, such as TE and TM modes, can also propagate in the guiding structure whose propagation constants are demonstrated in Fig.2.5 when there is no loss or negligible loss. In other cases, for the high-loss materials, to obtain the complex propagation sensitively and accurately is another subject for discontinuity analysis which is elaborated in next section, next the work concentrates on TEM mode with high loss in two-layer structures.

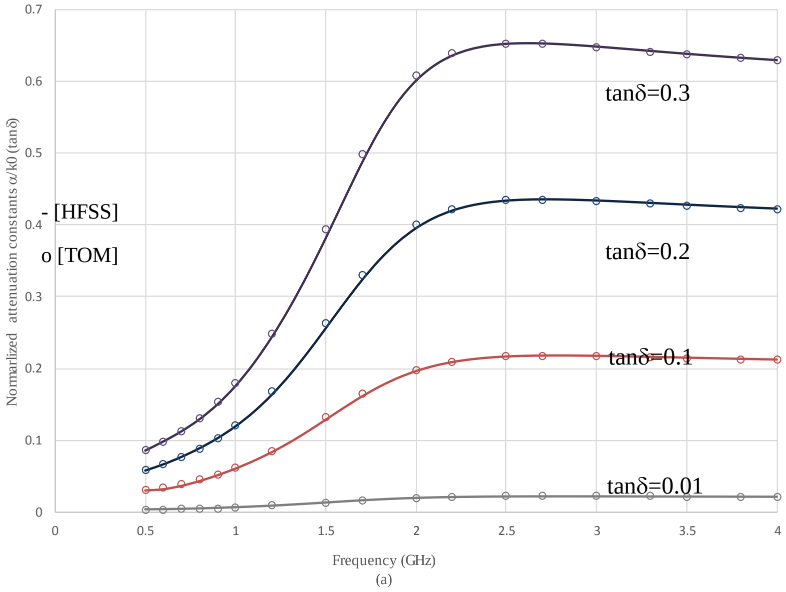

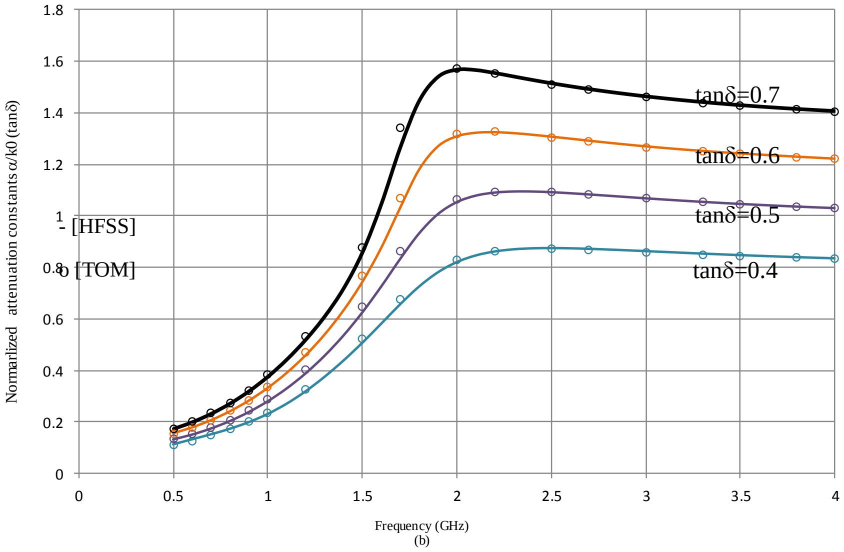

Fig.2.6. Normalized attenuation constants with a loss tangent (a) tanδ = 0.01, 0.1, 0.2 (b) tanδ = 0.4, 0.5, 0.6 of coaxial cell loaded with dielectric. Comparison between the numerical results ('o') and simulation results from HFSS (solid lines).

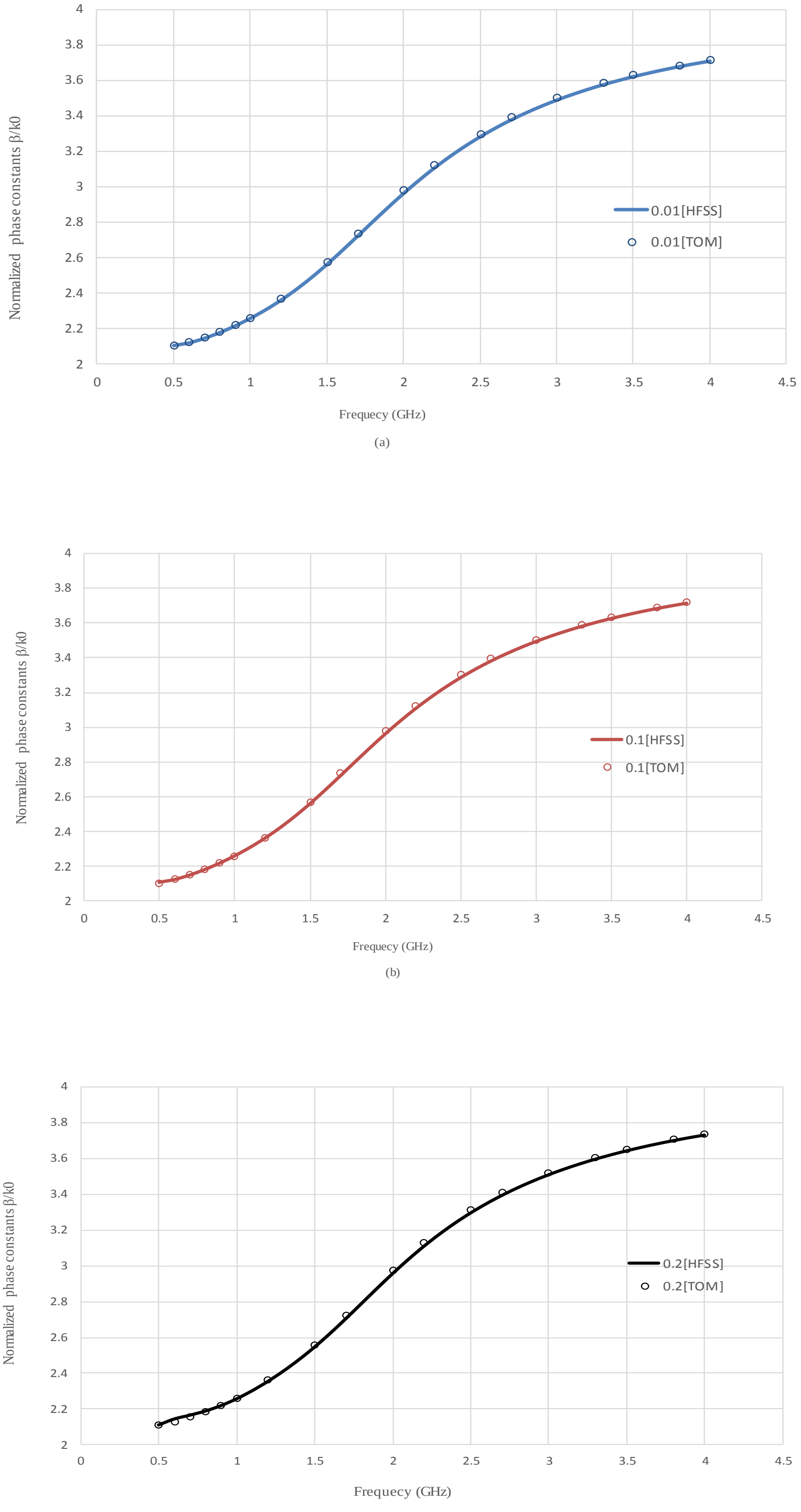

(a)

(b)

(c)

Fig.2.7. Normalized phase constants with a loss tangent (a) tanδ=0.01 (b) tanδ=0.1 coaxial cell loaded with dielectric. Comparison between the numerical results ('o') and simulation results from HFSS (solid lines).

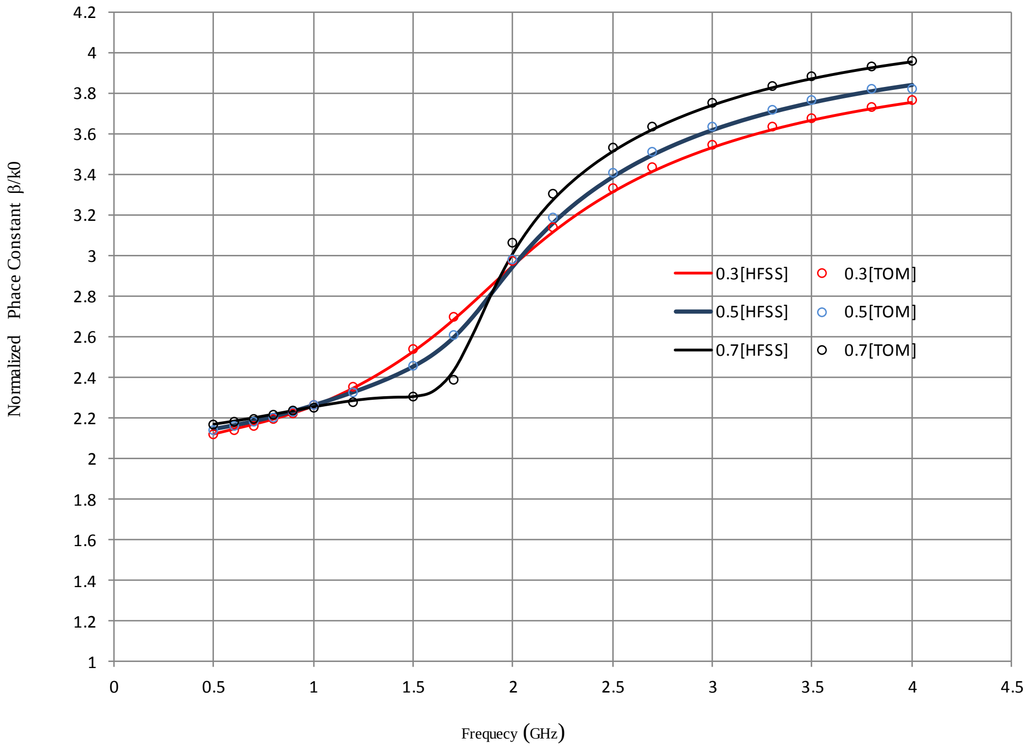

Fig.2.8. Normalized phase constants with a loss tangent tanδ=0.3, 0.5, 0.7 of coaxial cell loaded with dielectric. Comparison between the numerical results ('o') and simulation results from HFSS (solid lines).

In Fig.2.4, it is shown the phase constant of TEM mode without loss, and then we will discuss about the complex propagation constant for the lossy cases with the loss tangent over a range from 0.001 to 0.7. In our studies, we compared the normalized attenuation constant and normalized phase constant by our method ('o') with that of simulation result by HFSS in same multilayered structure. The normalized attenuation constants are compared in Fig.2.6, it shows that the numerical results derived from transverse operator method ('o') have been reached a very good agreement with those from simulation software HFSS over a frequency range from 0.5 to 4 GHz. And so are the normalized phase constants in Fig.2.7 and Fig.2.8. In the expressions, the complex propagation constants formed of attenuation constant and phase constant, are all normalized by the wavenumber in the free space k_0. Except for the accuracy, our method is also converged very fast which we will discuss in next chapter for the discontinuity analysis.

II.2.3 Propagation constants in loss three-layered structure

The transverse operator method is always used in the stratified structure. In this section, we will introduce a three-layered coaxial cell of the same dimensions filled with the lossy sample shown in Fig.2.9. The ring sample is sandwiched by Teflon and air in the three-layered coaxial cell, with the complex dielectric constants of the torus

Teflon and sample ε_{rt} and ε_{rd} and the thickness of those torus inserted objects are s and d shown in Table. 2.2. In this part, we will discuss the complex propagation constants of fundamental and higher order modes in the three-layered structure.

Table. 2.2. Structure parameters of multi-layered coaxial cell.

Parameters	Dielectric constants	Loss tangent	Dimensions(mm)
a	-	-	6
b	-	-	20
s	-	-	2
d	-	-	2
ε_{rt}	2.1	0.001	-
ε_{rd}	16	0.3	-

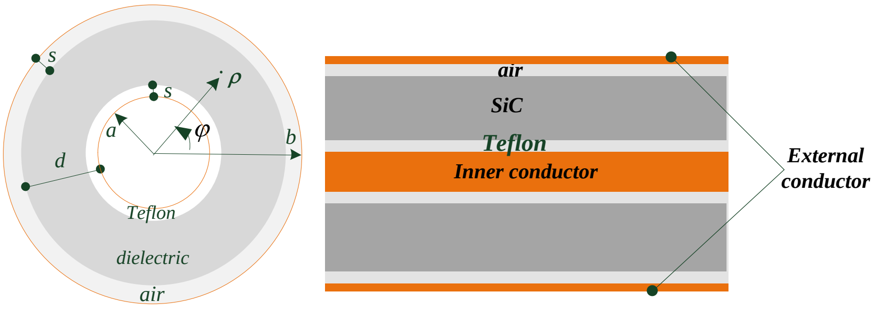

(a) (b)

Fig.2.9. Geometry of stratified structure (a) transverse cross-section and (b) longitudinal cross-section of coaxial cell loaded with dielectric.

Normally, the complex propagation constants are not easy to figure in the stratified structure with high loss. In this part, we researched on the complex propagation constants of fundamental mode (quasi-TEM) and evanescent higher order modes in the brand band frequency range from 1 to 2.5 GHz. The quasi-TEM propagates in the wave guiding structure with no cut off frequency, from last section, we know that the higher order modes propagate when the frequency is larger than 2.78GHz, so in this part we talk about the only one fundamental mode propagating in the coaxial cell, with the evanescent modes excited near the longitudinal discontinuities illustrated in Fig.2.10 and Fig.2.11. All the propagation constants and its field distribution are discussed here to lay the foundation for the longitudinal discontinuity analysis in the next chapter.

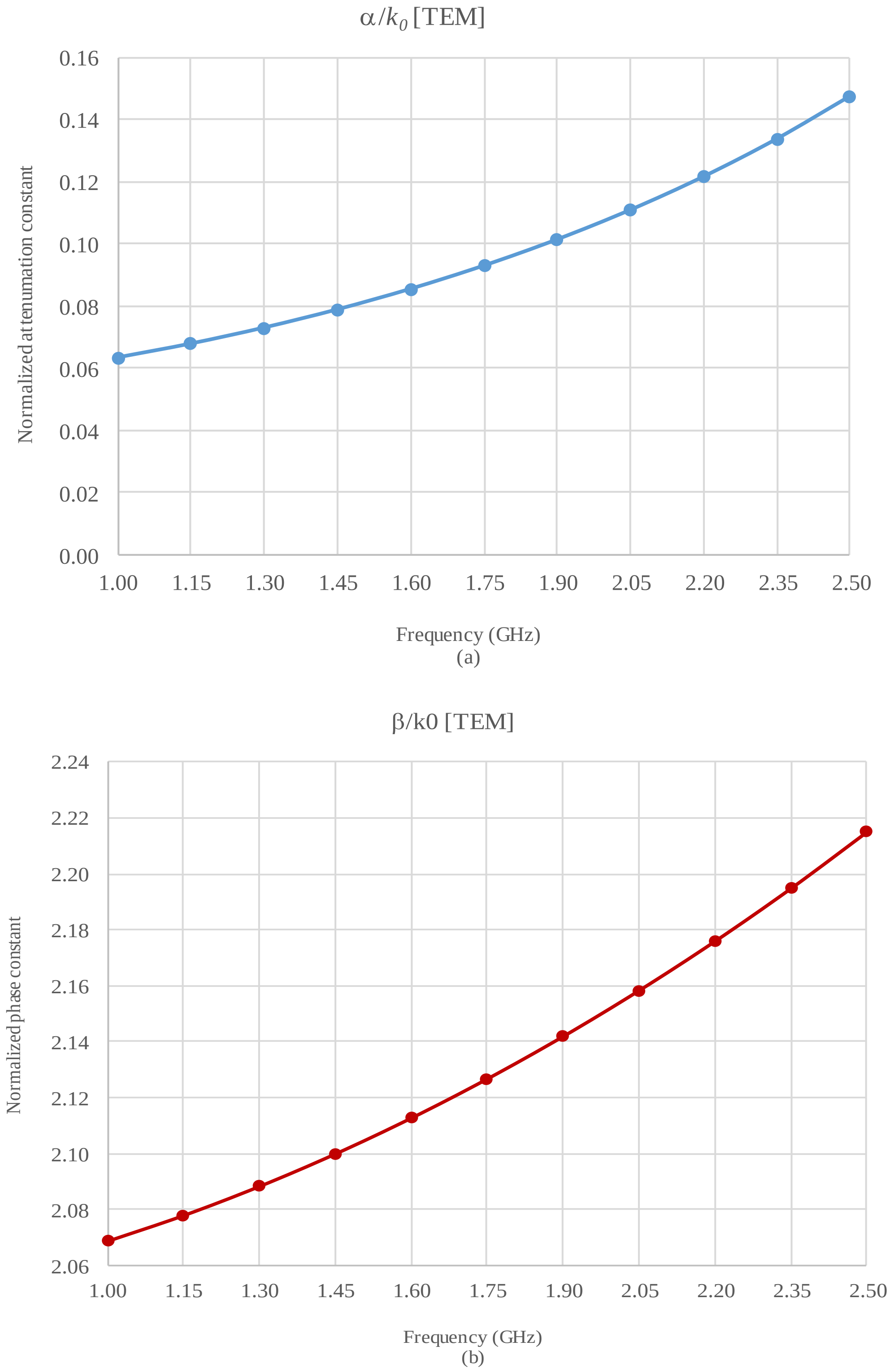

α/k_0 [TEM]

β/k0 [TEM]

Fig.2.10. Normalized complex propagation constant of fundamental mode (a) normalized attenuation constant and (b) normalized phase constant of three-layered coaxial cell.

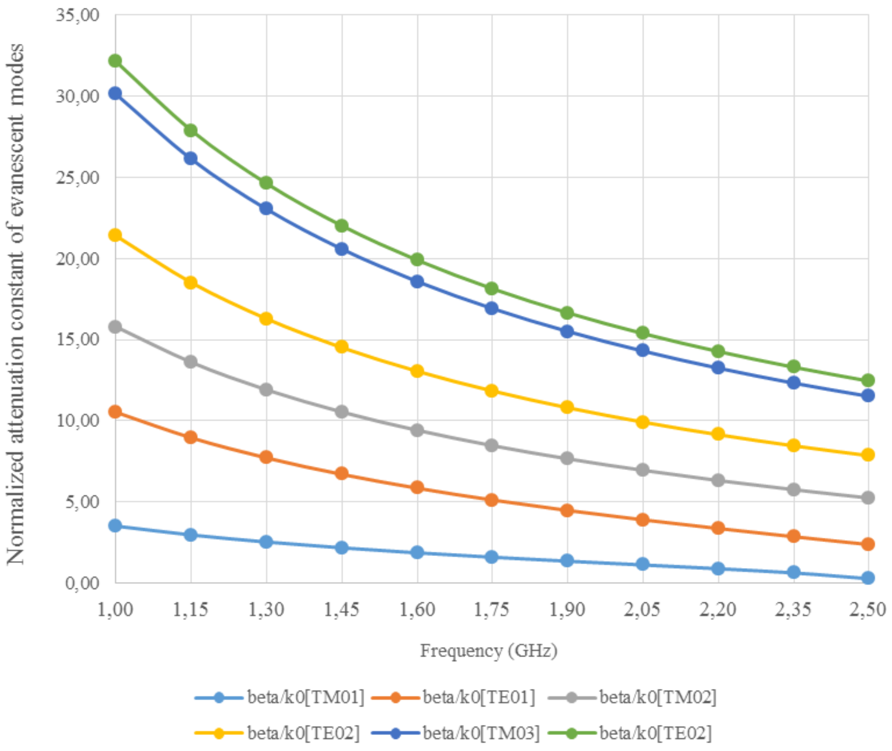

Fig.2.11. Normalized attenuation constants of evanescent higher order modes of three-layered coaxial cell.

II.3 EIGENVALUE ANALYSIS IN MULTILAYERED PLANAR STRUCTURE

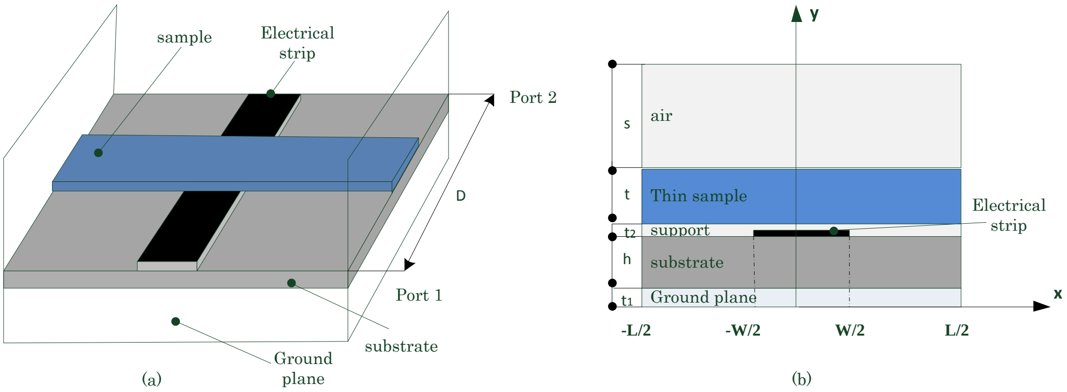

Fig.2.12. Test fixture loaded with thin film sample. (a) three-dimension and (b) cross section view. Source: Queffelec, P. Le Floc'h, M. and Gelin, P. (1998). "Broad-band characterization of magnetic and dielectric thin films using a microstrip line", IEEE Transmission on Instrumentation and Measurement, 47(4), 956-963.

Fig.2.12 shows a planar transmission line based measurement setup for thin layer dielectric sample. As the sample width is chosen to be large enough compared to the signal line width, the edge effect will be neglected and the central part can be considered as a boxed symmetric multilayered line that the half of structure is given in the following figure (Fig.2.13). The symmetry plane is at the left side.

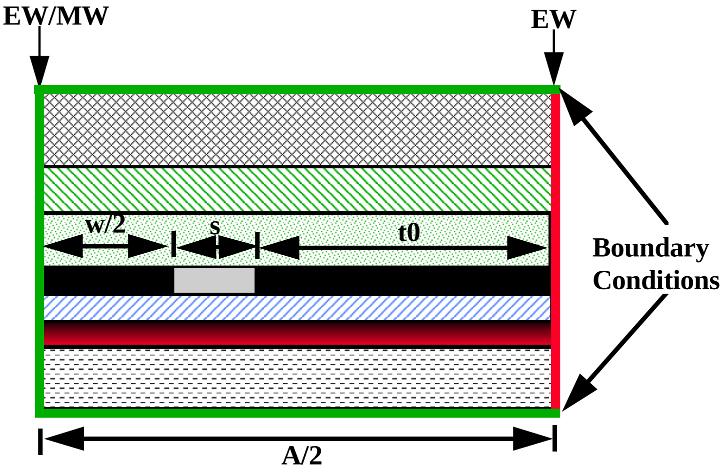

Fig.2.13. General Configuration of multilayered planar transmission line.

A short description of the modified transverse resonance method will be given in the first, followed by a number of studies on mode basis involved in the dielectric measurement work. These works will serve the direct analysis of the measurement cell with presence of thin sample.

II.3.1 Modified transverse resonance formulation

In the transverse resonance formulation in the report [II-9] and literatures[II-10], a boxed structure with perfect electric conductor boundary will be considered as several parallel plate waveguides put together, with the first and the last one be short circuited. The use of microwave network circuit theory will deduce the equivalent input impedance at one side, and the resonance will be obtained when this impedance is similar to a short circuit. As the input impedance is a function of transverse propagation constant which in turn depends on the *z* direction propagation constant, we obtain the eigenvalue problem with solutions corresponding to first and higher order modes.

In the original transverse resonance formulation, the reactive energy stored at the discontinuity neighborhood is represented by equivalent lump circuit element. A modified version of transverse resonance method has been developed by adapting the multimodal variational discontinuity analysis to the eigenvalue problem study.

II.3.1.1 Variational form for a three layers case

We consider three parallel plate transmission lines in Fig.2.14. For any electromagnetic wave propagating to *z* axis with $e^{-\gamma z}$ as propagation factor, the transverse propagation constant k_x in each layer is related to γ, and the height of parallel plate line. The electric and magnetic field in the section between x_{i-1} and x_i are given by

$$
\begin{aligned}
E_t^{(i)}(r) &= \sum_n \tilde{v}_n^{(i)}(x) e_{tn}^{(i)}(y) \\
J^{(i)}(r) &= \begin{bmatrix} H_z^{(i)} \\ -H_y^{(i)} \end{bmatrix}(r) = \sum_n \tilde{i}_n^{(i)}(x) j_n^{(i)}(y)
\end{aligned}
\qquad (2.15)
$$

The new vector $\mathbf{J}^{(i)}(r)$ has the advantage to be parallel to electric vector $\mathbf{E}_t$. Reduced modal voltage and current $v^{(i)}_n$ and i_n are defined by

$$
\tilde{v}_n^{(i)}(x) = A_n^{(i)} e^{-jk_{xn}^{(i)}x} + B_n^{(i)} e^{jk_{xn}^{(i)}x}, \quad \tilde{i}_n^{(i)}(x) = A_n^{(i)} e^{-jk_{xn}^{(i)}x} - B_n^{(i)} e^{jk_{xn}^{(i)}x} \qquad (2.16a)
$$

The rearrangement of these relations by using the modal voltage and current values at xi-1 will lead to the well-known relations for transmission line theory

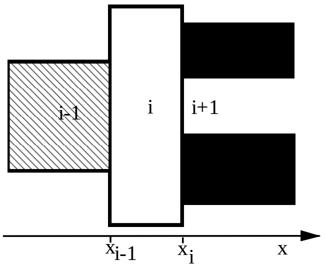

Fig.2.14. Transverse resonance formulation for three layers case.

$$
\begin{aligned}
\tilde{v}_n^{(i)}(x) &= \tilde{v}_n^{(i)}(x_{i-1}) \cos k_{xn}^{(i)}(x - x_{i-1}) - j\tilde{i}_n^{(i)}(x_{i-1}) \sin k_{xn}^{(i)}(x - x_{i-1}) \\
\tilde{i}_n^{(i)}(x) &= -j\tilde{v}_n^{(i)}(x_{i-1}) \sin k_{xn}^{(i)}(x - x_{i-1}) + \tilde{i}_n^{(i)}(x_{i-1}) \cos k_{xn}^{(i)}(x - x_{i-1})
\end{aligned}
\qquad (2.16b)
$$

The same relations can be obtained in i+1 region. The continuity relation at interface i+1 can be written as

$$
E_t^{(i)}(y) = E_t(x_i, y) = \sum_n \tilde{v}_n^{(i)}(x_i) e_{tn}^{(i)}(y) = \sum_n \tilde{v}_n^{(i+1)}(x_i) e_{tn}^{(i+1)}(y) \qquad (2.17a)
$$

$$
\mathcal{H}_i \sum_n \tilde{i}_n^{(i)}(x_i) j_n^{(i)}(y) = -\mathcal{H}_i \sum_n \tilde{i}_n^{(i+1)}(x_i) j_n^{(i+1)}(y) \qquad (2.17b)
$$

Here the use of Heaviside operator $\mathcal{H}_i$ will limit the continuity of tangential component of magnetic field in only part of interface which is no perfect electric conductor (Fig.2.14). In general, an element of a complete base is orthogonal to an element of an adjoint base. In the present situation, the nth solution of adjoint problem is supposed as known, with eigenvalue $k^{(i)+}_{un}$ and eigenvector $\{\boldsymbol{e}^{(i)}_{tn}, \boldsymbol{h}^{(i)}_{tn}\}^{+}$. Orthogonality is therefore illustrated by the following relation

$$\rangle \mathrm{j}^{(i)}_{\mathrm{m}}{}^{+} \left| \mathrm{e}^{(i)}_{tn} \right\langle = N^{(i)}_{n}\delta_{mn} \tag{2.18}$$

with δ_{mn} the Kronecker symbol. Using the adjoint basis, we can define the admittance operator by

$$\hat{Y}^{(i)}_{n} = \frac{\mathrm{j}^{(i)}_{\mathrm{n}}}{N^{(i)}_{n}} \rangle \mathrm{j}^{(i)}_{\mathrm{n}}{}^{+} \Big| \tag{2.19}$$

It's application to (2.17a) lead to the following

$$\hat{Y}^{(i)}_{n}\mathrm{E}^{(i)}_{\mathrm{t}}(y) = \tilde{v}^{(i)}_{n}(x_i)\,\mathrm{j}^{(i)}_{\mathrm{n}}(y), \quad \hat{Y}^{(i+1)}_{n}\mathrm{E}^{(i)}_{\mathrm{t}}(y) = \tilde{v}^{(i+1)}_{n}(x_i)\,\mathrm{j}^{(i+1)}_{\mathrm{n}}(y) \tag{2.20}$$

A new vector $\mathbf{J}^{(i)}_{t}$(y) is then defined at interface x_i by

$$\begin{aligned} \mathrm{J}^{(i)}(y) &= \sum_{\mathrm{n}} \tilde{i}^{(i)}_{\mathrm{n}}(x_{\mathrm{i}})\,\mathrm{j}^{(i)}_{\mathrm{n}}(y) + \sum_{\mathrm{m}} \tilde{i}^{(i+1)}_{\mathrm{m}}(x_{\mathrm{i}})\,\mathrm{j}^{(i+1)}_{\mathrm{m}}(y) \\ &= \left[\sum_{\mathrm{n}} \frac{\tilde{i}^{(i)}_{\mathrm{n}}(x_{\mathrm{i}})}{\tilde{v}^{(i)}_{\mathrm{n}}(x_{\mathrm{i}})} \hat{Y}^{(i)}_{\mathrm{n}} + \sum_{\mathrm{m}} \frac{\tilde{i}^{(i+1)}_{\mathrm{m}}(x_{\mathrm{i}})}{\tilde{v}^{(i+1)}_{\mathrm{m}}(x_{\mathrm{i}})} \hat{Y}^{(i+1)}_{\mathrm{m}} \right] \mathrm{E}^{(i)}_{\mathrm{t}}(y) \\ &= \left[\sum_{\mathrm{n}} \tilde{y}^{(i)}_{\mathrm{n}}(x_{\mathrm{i}})\hat{Y}^{(i)}_{\mathrm{n}} + \sum_{\mathrm{m}} \tilde{y}^{(i+1)}_{\mathrm{m}}(x_{\mathrm{i}})\hat{Y}^{(i+1)}_{\mathrm{m}} \right] \mathrm{E}^{(i)}_{\mathrm{t}}(y) \end{aligned} \tag{2.21}$$

For multilayer planar transmission line with only one partially metallized interface at x_i, the variational form on interface electric filed $\boldsymbol{E}^{(i)}_{t}$ is given by

$$\mathcal{F}\left\{\mathrm{E}^{(i)}_{\mathrm{t}}\right\} = \rangle \mathrm{E}^{(i)}_{\mathrm{t}} \left| \mathrm{J}^{(i)} \right\langle = \rangle \mathrm{E}^{(i)}_{\mathrm{t}} \left| \hat{Y}^{(i)} \mathrm{E}^{(i)}_{\mathrm{t}} \right\langle \tag{2.22}$$

As $\mathbf{J}^{(i)}$(y) will be null on the no metallic part and $\boldsymbol{E}^{(i)}_{t}$ will be null on conducting part, the minimization of (2.22) lead to a linear eigenvalue system whose solutions will determine the researched modal base.

Extend our studies in the case of two successive interfaces, as shown in Fig.2.14. The same equation that (2.21) is established for $\boldsymbol{E}^{(i-1)}_{t}$, using the basis of regions i-1 and i.

$$\mathrm{J}^{(\mathrm{i}-1)}(y) = \left[\sum_{\mathrm{n}} \tilde{y}_{\mathrm{n}}^{(\mathrm{i}\text{-}1)}\left(x_{\mathrm{i}\text{-}1}\right)\hat{Y}_{\mathrm{n}}^{(\mathrm{i}\text{-}1)} + \sum_{\mathrm{m}} \frac{\tilde{i}_{\mathrm{m}}^{(\mathrm{i})}\left(x_{\mathrm{i}\text{-}1}\right)}{\tilde{v}_{\mathrm{m}}^{(\mathrm{i})}\left(x_{\mathrm{i}\text{-}1}\right)}\hat{Y}_{\mathrm{m}}^{(\mathrm{i})}\right]\mathrm{E}_{\mathrm{t}}^{(\mathrm{i}\text{-}1)}(y) \tag{2.23a}$$

$$= \left[\sum_{\mathrm{n}} \tilde{y}_{\mathrm{n}}^{(\mathrm{i}\text{-}1)}\left(x_{\mathrm{i}\text{-}1}\right)\hat{Y}_{\mathrm{n}}^{(\mathrm{i}\text{-}1)} + \sum_{\mathrm{m}} \tilde{y}_{\mathrm{m}}^{(\mathrm{id})}\left(t_{\mathrm{i}}\right)\hat{Y}_{\mathrm{m}}^{(\mathrm{i})}\right]\mathrm{E}_{\mathrm{t}}^{(\mathrm{i}\text{-}1)}(y) + \left[\sum_{\mathrm{m}} \tilde{y}_{\mathrm{m}}^{(\mathrm{io})}\left(t_{\mathrm{i}}\right)\hat{Y}_{\mathrm{m}}^{(\mathrm{i})}\right]\mathrm{E}_{\mathrm{t}}^{(\mathrm{i})}(y$$

$$\mathrm{J}^{(\mathrm{i})}(y) = \left[\sum_{\mathrm{m}} \frac{\tilde{i}_{\mathrm{m}}^{(\mathrm{i})}\left(x_{\mathrm{i}}\right)}{\tilde{v}_{\mathrm{m}}^{(\mathrm{i})}\left(x_{\mathrm{i}}\right)}\hat{Y}_{\mathrm{m}}^{(\mathrm{i})} + \sum_{\mathrm{n}} \tilde{y}_{\mathrm{n}}^{(\mathrm{i}+1)}\left(x_{\mathrm{i}}\right)\hat{Y}_{\mathrm{n}}^{(\mathrm{i}+1)}\right]\mathrm{E}_{\mathrm{t}}^{(\mathrm{i})}(y) \tag{2.23b}$$

$$= \left[\sum_{\mathrm{m}} \tilde{y}_{\mathrm{m}}^{(\mathrm{io})}\left(t_{\mathrm{i}}\right)\hat{Y}_{\mathrm{m}}^{(\mathrm{i})}\right]\mathrm{E}_{\mathrm{t}}^{(\mathrm{i}\text{-}1)}(\mathrm{y}) + \left[\sum_{\mathrm{m}} \tilde{y}_{\mathrm{m}}^{(\mathrm{id})}\left(t_{\mathrm{i}}\right)\hat{Y}_{\mathrm{m}}^{(\mathrm{i})} + \sum_{\mathrm{n}} \tilde{y}_{\mathrm{n}}^{(\mathrm{i}+1)}\left(x_{\mathrm{i}}\right)\hat{Y}_{\mathrm{n}}^{(\mathrm{i}+1)}\right]\mathrm{E}_{\mathrm{t}}^{(\mathrm{i})}(y)$$

or in a more compact form

$$\begin{bmatrix} \mathrm{J}^{(\mathrm{i}-1)} \\ \mathrm{J}^{(\mathrm{i})} \end{bmatrix} = \begin{bmatrix} \hat{Y}^{(\mathrm{i}-1,\mathrm{i}-1)} & \hat{Y}^{(\mathrm{i}-1,\mathrm{i})} \\ \hat{Y}^{(\mathrm{i},\mathrm{i}-1)} & \hat{Y}^{(\mathrm{i},\mathrm{i})} \end{bmatrix} \begin{bmatrix} \mathrm{E}_{\mathrm{t}}^{(\mathrm{i}\text{-}1)} \\ \mathrm{E}_{\mathrm{t}}^{(\mathrm{i})} \end{bmatrix} \tag{2.23c}$$

The associated stationary form is then

$$\mathcal{F}\left\{\begin{bmatrix} \mathrm{E}_{\mathrm{t}}^{(\mathrm{i}\text{-}1)} \\ \mathrm{E}_{\mathrm{t}}^{(\mathrm{i})} \end{bmatrix}\right\} = \left\rangle \begin{bmatrix} \mathrm{E}_{\mathrm{t}}^{(\mathrm{i}\text{-}1)} \\ \mathrm{E}_{\mathrm{t}}^{(\mathrm{i})} \end{bmatrix}^{t} \middle| \begin{bmatrix} \mathrm{J}^{(\mathrm{i}-1)} \\ \mathrm{J}^{(\mathrm{i})} \end{bmatrix} \right\langle = \left\rangle \begin{bmatrix} \mathrm{E}_{\mathrm{t}}^{(\mathrm{i}\text{-}1)} \\ \mathrm{E}_{\mathrm{t}}^{(\mathrm{i})} \end{bmatrix}^{t} \middle| \hat{Y} \begin{bmatrix} \mathrm{E}_{\mathrm{t}}^{(\mathrm{i}\text{-}1)} \\ \mathrm{E}_{\mathrm{t}}^{(\mathrm{i})} \end{bmatrix} \right\langle \tag{2.24}$$

We have now opportunity to discuss the presence in equations (2.21) and (2.23) of reduced admittances Y. If the region i-1 is preceded (or succeeded) by one of the side boundary, our knowledge of the theory of the transmission lines makes it easy to determine these admittances according to the boundary condition (electric, magnetic or simply matched load).

Depending on whether the structure can be divided into two or three subsections, the stationary form studied will be (2.22) or (2.24). For a more complex structure, a generalization of (2.24) is necessary.

II.3.1.2 Linear eigenvalue system

Choose an appropriate base on which we project the fields $\boldsymbol{E}_{\mathrm{t}}^{(\mathrm{i})}$ as follows

$$\mathrm{E}_{\mathrm{t}}^{(\mathrm{i})}(y) = \sum_{\mathrm{q}} c_{\mathrm{q}}^{(\mathrm{i})} \mathrm{g}_{\mathrm{q}}^{(\mathrm{i})}(\mathrm{y}) \tag{2.25}$$

We then have the quadratic form corresponding to (2.22)

$$\sum_{p}\sum_{q} c_{\mathrm{p}}^{(\mathrm{i})} c_{q}^{(\mathrm{i})} G_{pq}\ , \quad G_{pq} = \left\rangle \mathrm{g}_{\mathrm{p}}^{(\mathrm{i})} \middle| \hat{Y}^{(\mathrm{i})}\, \mathrm{g}_{\mathrm{q}}^{(\mathrm{i})} \right\langle \tag{2.26}$$

An approximate solution, thus numerical problem will be obtained by minimizing (2.26), which leads to the following linear system of equations

$$\sum_q G_{pq} c_{\mathrm{q}}^{(\mathrm{i})} = 0 \tag{2.27}$$

The matrix $\{G_{pq}\}$ for an one interface problem is given by

$$\begin{aligned} G_{\mathrm{pq}} &= \rangle \mathrm{g}_{\mathrm{p}}^{(\mathrm{i})} \left[\sum_{\mathrm{n}} \tilde{y}_{\mathrm{n}}^{(\mathrm{i})}(x_{\mathrm{i}}) \hat{Y}_{\mathrm{n}}^{(\mathrm{i})} + \sum_{\mathrm{m}} \tilde{y}_{\mathrm{m}}^{(\mathrm{i+1})}(x_{\mathrm{i}}) \hat{Y}_{\mathrm{m}}^{(\mathrm{i+1})} \right] \mathrm{g}_{\mathrm{q}}^{(\mathrm{i})} \langle \\ &= \sum_{\mathrm{n}} \tilde{y}_{\mathrm{n}}^{(\mathrm{i})}(x_{\mathrm{i}}) \rangle \mathrm{g}_{\mathrm{p}}^{(\mathrm{i})} \hat{Y}_{\mathrm{n}}^{(\mathrm{i})} \mathrm{g}_{\mathrm{q}}^{(\mathrm{i})} \langle + \sum_{\mathrm{m}} \tilde{y}_{\mathrm{m}}^{(\mathrm{i+1})}(x_{\mathrm{i}}) \rangle \mathrm{g}_{\mathrm{p}}^{(\mathrm{i})} \hat{Y}_{\mathrm{m}}^{(\mathrm{i+1})} \mathrm{g}_{\mathrm{q}}^{(\mathrm{i})} \langle \\ &= \sum_{\mathrm{n}} \tilde{y}_{\mathrm{n}}^{(\mathrm{i})}(x_{\mathrm{i}}) \rangle \mathrm{g}_{\mathrm{p}}^{(\mathrm{i})} \mathrm{j}_{\mathrm{n}}^{(\mathrm{i})} \langle \rangle \mathrm{j}_{\mathrm{n}}^{(\mathrm{i})+} \mathrm{g}_{\mathrm{q}}^{(\mathrm{i})} \langle + \sum_{\mathrm{m}} \tilde{y}_{\mathrm{m}}^{(\mathrm{i+1})}(x_{\mathrm{i}}) \rangle \mathrm{g}_{\mathrm{p}}^{(\mathrm{i})} \mathrm{j}_{\mathrm{m}}^{(\mathrm{i+1})} \langle \rangle \mathrm{j}_{\mathrm{m}}^{(\mathrm{i+1})+} \mathrm{g}_{\mathrm{q}}^{(\mathrm{i})} \langle \end{aligned} \tag{2.28}$$

In the same manner we can get for a two interfaces structure the following quadratic form

$$\sum_{u=i-1}^{i} \sum_{v=i-1}^{i} \sum_{p} \sum_{q} c_{\mathrm{p}}^{(\mathrm{u})} c_{\mathrm{q}}^{(\mathrm{v})} G_{pq}^{(\mathrm{uv})} \ , \quad G_{pq}^{(\mathrm{uv})} = \left(\mathrm{g}_{\mathrm{p}}^{(\mathrm{u})} \left(\hat{Y}^{(\mathrm{uv})} \mathrm{g}_{\mathrm{q}}^{(\mathrm{v})} \right(\right. \right. \tag{2.29}$$

And the corresponding linear system

$$\sum_{v=i-1}^{i} \sum_{q} G_{pq}^{(\mathrm{uv})} c_{\mathrm{q}}^{(\mathrm{v})} = 0 \tag{2.30}$$

The matrices {G} are defined as for (2.28), and will be explicated by studying some real structures. The resolution of (2.27) or (2.30) allows the determination of the propagation constant for the first and higher order modes, corresponding to the eigenvalues, and the development coefficients of the fields, corresponding to the eigenvectors.

II.3.1.3 Matrix development for practical transmission lines

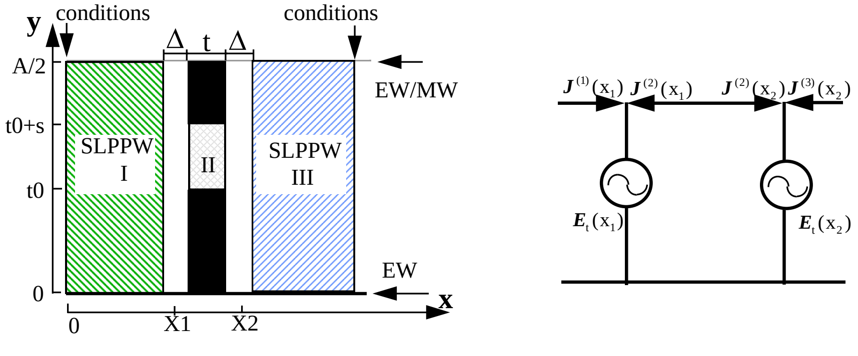

Fig.2.15. General cross section configuration and its equivalent circuit.

For practical boxed planar transmission lines, such as finline [I-24][II-12], microstrip [II-13], stripline [II-14], planar-plate [II-15]-[II-18], coplanar waveguide or slotline [II-19][II-20], we propose a general cross section configuration as follows

For each parallel plate section with height of A, we have the mode basis given by the solution of the following differential equations

- modes TE_x

$$\xi''(y)+k_y{}^2\xi(y)=0,\ \text{avec}\ \ \xi(0)=\xi(A)=0 \tag{2.31a}$$

$$\phi''(x)+k_x{}^2\phi(x)=0 \tag{2.31b}$$

- modes TM_x

$$\zeta''(y)+k_y{}^2\zeta(y)=0,\ \text{avec}\ \ \zeta'(0)=\zeta'(A)=0 \tag{2.31c}$$

$$\varphi''(x)+k_x{}^2\varphi(x)=0 \tag{2.31d}$$

with the transverse propagation constant**Error! Objects cannot be created from editing field codes.**. The solutions of (2.31a) and (2.31c) will be of sinusoidal type with the nth eigenvalue and eigenfunction given by

$$k_{yn}=\frac{n\pi}{A},\ \ \xi_n(y)=A_n\sin k_{yn}y,\ \ \zeta_n(y)=B_n\cos k_{yn}y \tag{2.32}$$

The transverse variation will be determined by initial values $\tilde{v}_{\mathrm{n}}^{(\mathrm{i})}(x_0)$ and $\tilde{i}_{\mathrm{n}}^{(\mathrm{i})}(x_0)$. The complete solution for each component is in the following relations

- Mode TE_x :

$$e_{\mathrm{yn}}(y)=\sqrt{\varepsilon_n/w}\cosh\tau_{\mathrm{n}}\cos k_{\mathrm{yn}}y=\mathrm{Ch}\,\tau_{\mathrm{n}}\cos k_{\mathrm{yn}}y \tag{2.33a}$$

$$e_{\mathrm{zn}}(y)=\sqrt{\varepsilon_n/w}\sinh\tau_{\mathrm{n}}\sin k_{\mathrm{yn}}y=\mathrm{Sh}\,\tau_{\mathrm{n}}\sin k_{\mathrm{yn}}y \tag{2.33b}$$

$$h_{\mathrm{yn}}(y)=-y_{\mathrm{n}}\,\mathrm{Sh}\,\tau_{\mathrm{n}}\sin k_{\mathrm{yn}}y \tag{2.33c}$$

$$h_{\mathrm{zn}}(y)=y_{\mathrm{n}}\,\mathrm{Ch}\,\tau_{\mathrm{n}}\cos k_{\mathrm{yn}}y \tag{2.33d}$$

- Mode TM$_x$

$$e''_{yn}(y) = \sqrt{2/w}\cosh\tau''_n \cos k_{yn} y = \mathrm{Ch}\,\tau''_n \cos k_{yn} y \qquad (2.34a)$$

$$e''_{zn}(y) = \sqrt{2/w}\sinh\tau''_n \sin k_{yn} y = \mathrm{Sh}\,\tau''_n \sin k_{yn} y \qquad (2.34b)$$

$$h''_{yn}(y) = -y''_n\,\mathrm{Sh}\,\tau''_n \sin k_{yn} y \qquad (2.34c)$$

$$h''_{zn}(y) = y''_n\,\mathrm{Ch}\,\tau''_n \cos k_{yn} y \qquad (2.34d)$$

One can note that $\boldsymbol{j}_n(y) = \boldsymbol{h}_{tn}(y)\times x = y_n \boldsymbol{e}_{tn}(y)$, which permits the simplification of equations (2.33) and (2.34) when using TE$_x$ and TM$_x$ as basis function.

The coefficients Chτ_n and Shτ_n are given in the following table, so as the reduced admittance for each TE$_x$ and TM$_x$ modes.

	TE$_{xn}$	TM$_{xn}$
Chτ_n	$\sqrt{\varepsilon_n/A}\,\dfrac{\gamma}{k_{un}}$	$-\sqrt{2/A}\,\dfrac{k_{yn}}{k_{un}}$
Shτ_n	$\sqrt{\varepsilon_n/A}\,\dfrac{k_{yn}}{k_{un}}$	$-\sqrt{2/A}\,\dfrac{\gamma}{k_{un}}$
y_n	$k^{(i)}_{xn}/\omega\mu_0\mu^{(i)}_r$	$\omega\varepsilon_0\varepsilon^{(i)}_r/k^{(i)}_{xn}$
Y_n	$k^{(i)}_{xn}/k_0\mu^{(i)}_r$	$k_0\varepsilon^{(i)}_r/k^{(i)}_{xn}$

$Y_n = Z_0 y_n$ est is the real admittance with Z_0 the free space wave impedance. $\varepsilon_0=1$, $\varepsilon_n=2$, for $n\neq0$. For $n=0$, both 3 components for TM$_x$ mode will be null, while TE$_{x0}$, represents the DC field between 2 parallel plate with e_{y0}.

There exist many possible trial functions. For our part, the Chebyshev polynomial has been chosen for the facilitation to obtain the Fourier transform. In the Table. 2.3, we have listed the trial functions and the corresponding Fourier transform for each type of most often used planar structures.

Table. 2.3. Trial functions and Fourier transform for different boxed structures.

$$\xi_q(\mathrm{y})=\frac{1}{\sqrt{s}}\mathrm{T}_q(\eta)\left(1-\eta^2\right)^{-1/2}\quad \tilde{g}^{(\mathrm{s})}_{\mathrm{qny}}=\int_s \xi_q(\mathrm{y})\cos k^{(\mathrm{s})}_{\mathrm{yn}}y\,dy,\ \tilde{g}^{(\mathrm{p})}_{\mathrm{qny}}=\int_s \xi_q(\mathrm{y})\cos k^{(\mathrm{p})}_{\mathrm{yn}}(y-t_0)\,dy$$

$$\zeta_q(\mathrm{y})=\frac{1}{\sqrt{s}}\mathrm{U}_q(\eta)\qquad \tilde{g}^{(\mathrm{s})}_{\mathrm{qnz}}=\int_s \zeta_q(\mathrm{y})\sin k^{(\mathrm{s})}_{\mathrm{yn}}y\,dy,\ \tilde{g}^{(\mathrm{p})}_{\mathrm{qnz}}=\int_s \zeta_q(\mathrm{y})\sin k^{(\mathrm{p})}_{\mathrm{yn}}(y-t_0)\,dy$$

Structures	boxed microstrip	boxed CPW	Finline/boxed Slotline
η	y/s	2(y-t0)/s-1	2(y-t0)/s-1
q	0, 2, 4,...	0, 1, 2, 3,...	0, 2, 4,...
symmetry plane	MW	MW	EW
$k^{(s)}_{yn}$	(2n-1)π/A	(2n-1)π/A	2nπ/(A/2)
$k^{(p)}_{yn}$	nπ/s	nπ/s	2nπ/s
$\frac{2}{\pi\sqrt{s}}\tilde{g}^{(s)}_{qny}$	$(-1)^{q/2}\,\mathrm{J}_q(k^{(s)}_{yn}s)$	$cos\,0.5(k^{(s)}_{yn}A-q\pi)\,J_q(0.5k^{(s)}_{yn}s)$	$\cos(k^{(s)}_{yn}\frac{A}{2}-q\pi)\,J_q(0.5k^{(s)}_{yn}s)$
$\frac{2}{\pi\sqrt{s}}\tilde{g}^{(s)}_{qnz}$	$\frac{2}{\pi\sqrt{s}}\tilde{g}^{(s)}_{qny}\frac{q}{k^{(s)}_{yn}s}$	$\frac{2}{\pi\sqrt{s}}\tilde{g}^{(s)}_{qny}\frac{2q}{k^{(s)}_{yn}s}$	$\frac{2}{\pi\sqrt{s}}\tilde{g}^{(s)}_{qny}\frac{2q}{k^{(s)}_{yn}s}$
$\frac{2}{\pi\sqrt{s}}\tilde{g}^{(p)}_{qny}$	$(-1)^{q/2}\,\mathrm{J}_q(n\pi)$	$\cos 0.5(n-q)\pi\,\mathrm{J}_q(0.5n\pi)$	$(-1)^n\cos 0.5q\pi\,\mathrm{J}_q(0.5n\pi)$

$\frac{2}{\pi\sqrt{s}}\tilde{g}_{qnz}^{(p)}$	$(-1)^{q/2} q\, J_q(n\pi)/n\pi$	$cos 0.5(n-q)\pi 2q\, J_q(0.5n\pi)/n\pi$	$(-1)^n \cos 0.5q\pi q\, J_q(0.5n\pi)/n\pi$

With the determination of parallel plate structure’s eigenfunction and the trial function, the linear system depends on the matrix G in (2.26) for one interface case and (2.30) for two interfaces case. As an example, for G_{yzpq}, the development of matrix elements in (2.30) can be taken as follows:

$$\begin{aligned} G_{yzpq}^{(11)} &= \sum_n \frac{\varepsilon_n}{A} Y_n^{(1)}(x_1) \cosh \tau_n^{(s)} \sinh \tau_n^{(s)+} \tilde{g}_{pny}^{(s)} \tilde{g}_{qnz}^{(s)} + \sum_m \frac{\varepsilon_m}{s} Y_m^{(2d)}(t) \cosh \tau_m^{(p)} \sinh \tau_m^{(p)+} \tilde{g}_{pmy}^{(p)} \tilde{g}_{qmz}^{(p)} \\ &= \sum_n D_{yzn}^{(s1)} \tilde{g}_{pny}^{(s)} \tilde{g}_{qnz}^{(s)} + \sum_m D_{yzm}^{(pd)} \tilde{g}_{pmy}^{(p)} \tilde{g}_{qmz}^{(p)} \end{aligned}$$

II.3.2 Numerical results

In this section, we will first determine the mode basis of the reference microstrip line used in our measurement setup. After that a number of known and unknown material filled multilayer structure will be studied, with results compared to other obtained from some most used commercial software.

II.3.2.1 Mode basis of reference microstrip line

For our study, we chose the material AD255C as substrate with electrical properties given in Table. 2.4. This material allows circuit design with low dielectric, low cost and excellent low loss characteristics. The stability over wide frequency and temperature ranges makes it ideal for variety microwave and RF applications. The other parameters of the reference microstrip line shown in Fig.2.12 are: h = 1.524mm the substrate thickness, w = 4. 257mm, the central strip width, and $t_1 = t_2 = 35\mu m$ the thickness of the strip conductor and ground conductor.

Table. 2.4. Frequency dependent parameters of Substrate ADC-255C.

Properties	@1MHz	@10GHz
Relative permittivity (may vary by thickness)		
Dielectric Constant (ε_r)	2.55	2.55
Dissipation factor (loss tangent or tanδ)	0.0011	0.0014

Here we will consider only zero thickness assumption case. By varying frequency between 200MHz and 1.6GHz which is the working frequency range for designed measurement setup, we obtain the first 3 eigenvalues in Fig.2.16. We can see that in this frequency range only the first mode - named also quasi-TEM mode, is the only propagated one, when all the higher order modes are evanescent with only imaginary part of the complex propagation constant.

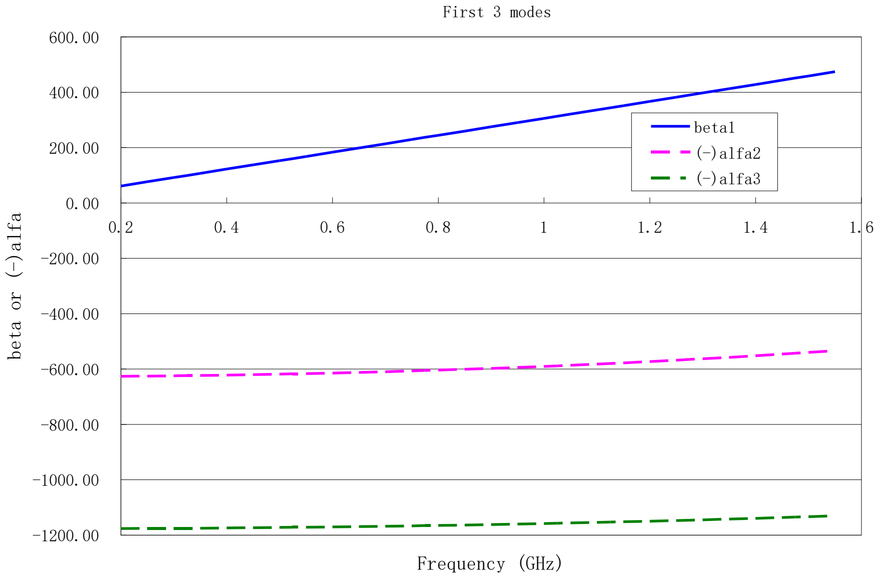

Fig.2.16. Propagation constants of first three modes in microstrip line.

II.3.2.2 Mode basis for some dielectric filled multilayered structures

In this part we will consider first the multilayer case with alumina slab with several thicknesses from 0.25mm to 2mm. Then Plexiglas filled structure will be also studied. Finally we will finish a ceramic material of former Transtech company for which only the lossless case is considered.

- *Alumina filled multilayer structures*

Here we consider that the relative permittivity of our alumina slab is 9.9 and the eigenmode researches are taken for thickness varying from 0.25mm to 2mm. The influence of alumina thickness on the normalized propagation constant for the quasi-TEM mode is shown in Fig.2.17, while the frequency behaviour for the first and second higher modes are given in Fig.2.18. We can see that only the propagating quasi-TEM mode is very sensitive to the alumina sample thickness, when both the first and the second higher order mode remain unchanged with the sample thickness varying from 0.25mm to 2mm. This can be explicated by the evanescent nature for which the box mode is predominant.

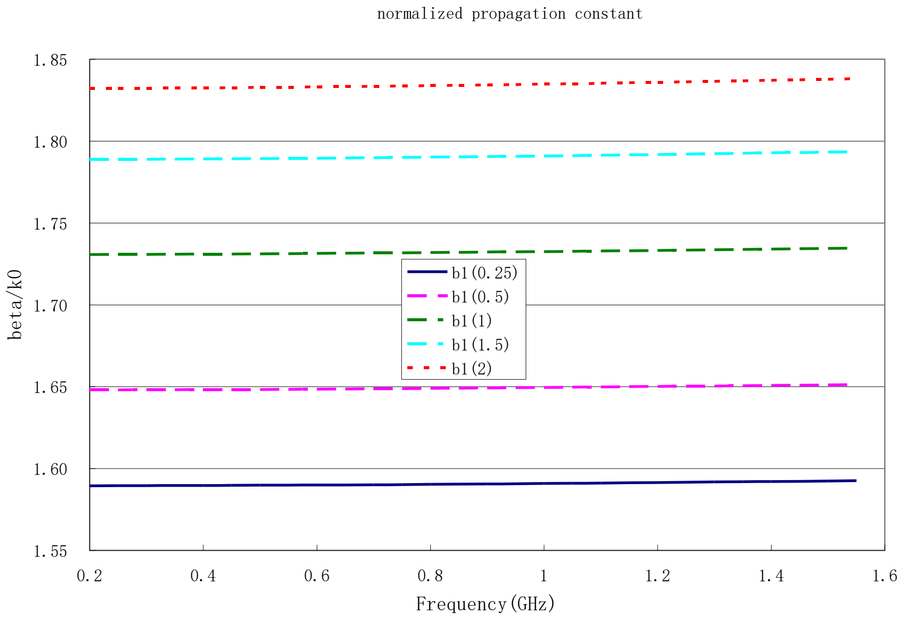

Fig.2.17. Normalized propagation constants of alumina covered microstrip line with different slab thickness (from 0.25mm to 2mm)

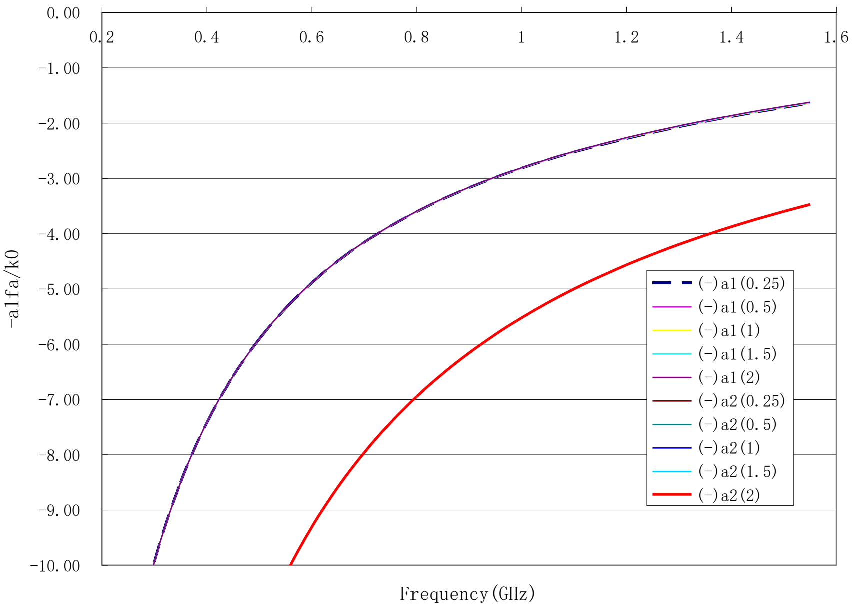

Fig.2.18. Normalized attenuation constants of first two evanescent modes in alumina covered microstrip line.

- *Plexiglas filled multilayer structures*

We consider a Plexiglas slab of 10mm thickness above the reference microstrip line. In Fig.2.19 the relative propagation constant is given in 200MHz-1600MHz frequency range, while the higher order modes are characterized by relative attenuation constant in the same frequency range in Fig.2.20.

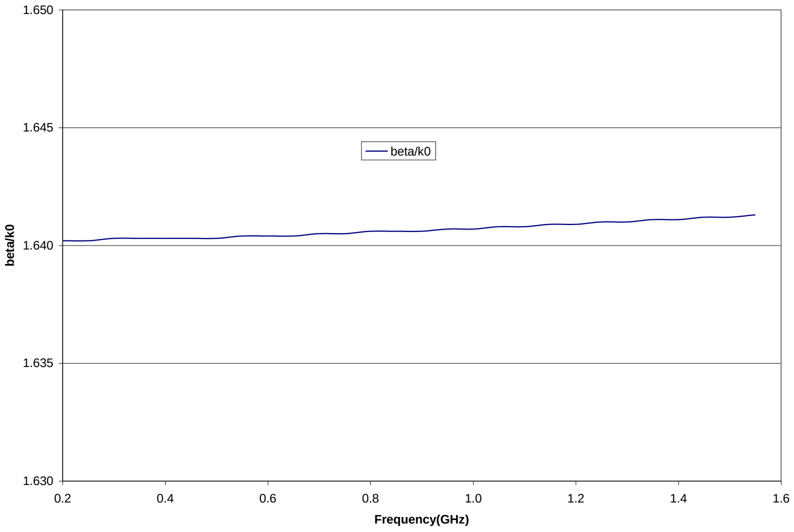

Fig.2.19. Normalized propagation constants of plexiglass covered microstrip line

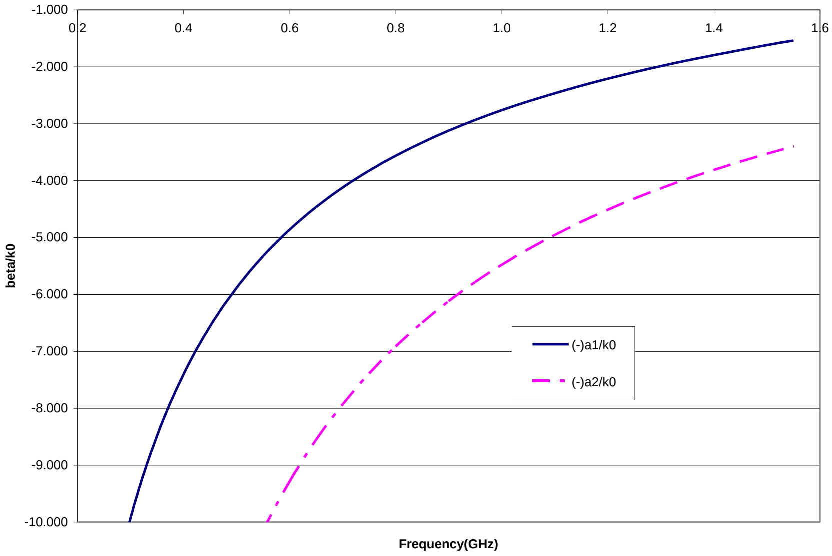

Fig.2.20. Normalized attenuation constants of first two evanescent modes in plexiglass covered microstrip line.

- *<u>Transtech ceramic filled multilayer structures</u>*

A Transtech ceramic slab (D16) of thickness 1.02mm is considered here. By covering the reference microstrip line with this slab the normalized propagation constant of TEM-like mode is given in Fig.2.21 with relative permittivity of 16 (given by Transtech at 10GHz). Fig.2.22 shows the normalized attenuation constant in the two first higher order modes.

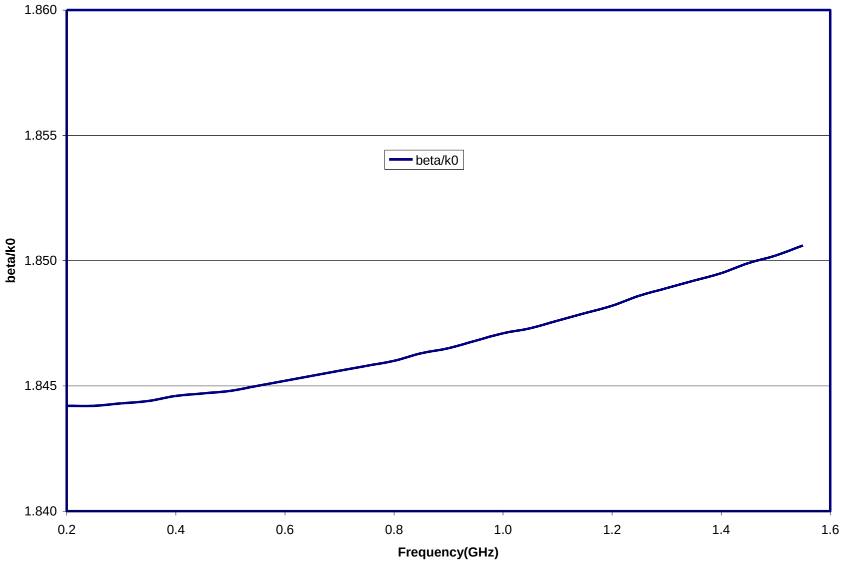

Fig.2.21. Normalized propagation constants of D16 covered microstrip line

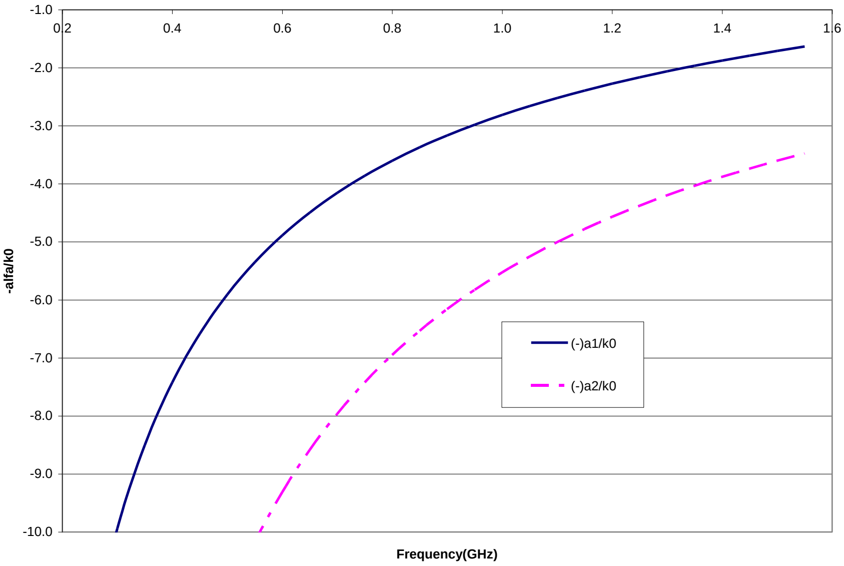

Fig.2.22. Normalized attenuation constants of first two evanescent modes in D16 covered microstrip line.

II.4 CONCLUSION

In order to determine the eigenmode basis for two guiding structures involved in our dielectric measurement cells, multilayered coaxial structure and multilayered multi dielectric planar structure, eigenvalue system has been obtained respectively by:

- Transverse operator method in cylindrical coordinates for multilayered coaxial structure;

- Modified transverse resonance formulation for multilayered multi dielectric planar structure;

Both formulations have been implanted in Matlab framework for corresponding structures used in dielectric measurement cell fabrication. Numerical simulations have been obtained by these two methods and compared to those from finite element method based commercial software.

Good agreements have been obtained for all cases, allowing us the possibility to pursue the discontinuity analysis in the following chapter.

References of chapter II

[II-1]. R. F. Harrington, Time-Harmonic Electromagnetic Fields, New York: McGraw-Hill, 1961.

[II-2]. J. R. Wait, Electromagnetic waves in stratified Media, New York: Pergamon Press, 1962.

[II-3]. J. W. Tao, R. Andriamanjato, & H. Baudrand. "General waveguide problems studies by transverse operator method." *IEEE transactions on magnetics* 31.3 (1995): 1626-1629.

[II-4]. J. W. Tao, J. Atechian, R. Ratovondrahanta, & H. Baudrand, "Transverse operator study of a large class of multidielectric waveguides." *IEE Proceedings H (Microwaves, Antennas and Propagation)*. Vol. 137. No. 5., 1990.

[II-5]. J. W. Tao, B. Chan, & H. Baudrand. "Rigorous theoretical study of longitudinally magnetized partially filled TEM phase shifter." *Electronics Letters* 26.17 (1990): 1329-1331.

[II-6]. R. Andriamanjato, B. Chan, J. W. Tao, & H. Baudrand, "Full-wave analysis of dielectric waveguide ferrite phase shifter with longitudinal magnetization." *Electronics Letters* 28.20 (1992): 1907-1908.

[II-7]. H. Baudrand J. W. Tao, & J. Atechian, "Study of radiating properties of open-ended waveguide." *IEEE Transactions on Antenna & Propagation*, Vol.36, pp.1071-1077, Aug.1988.

[II-8]. A. D. Bresler, G. H. Joshi, & N. Marcuvitz. "Orthogonality properties for modes in passive and active uniform wave guides." *Journal of Applied Physics* 29.5 (1958): 794-799.

[II-9]. J. W. Tao, La methode de resonance transverse modifiee. Mai 1997.

[II-10]. R. Sorrentino, and M. Mongiardo, Transverse Resonance Techniques-Encyclopedia of RF and Microwave Engineering, New York: John Wiley & Sons, Apr. 2005.

[II-11]. R. Sorrentino and T. Itoh, "Transverse resonance analysis of finline discontinuities," *IEEE Trans. Microwave Theory Tech.*, vol. MTT-324, pp:1663-1638, Jan. 1984.

[II-12]. J. Bornemann, F. Arndt. "Calculating the characteristic impedance of finlines by transverse resonance method." *IEEE Transactions on microwave theory and techniques*, 34.1 (1986): 85-92.

[II-13]. T. Uwano, R. Sorrentino, T. Itoh. "Characterization of microstrip-to-slotline transition discontinuites by transverse resonance analysis," *IEEE-17th European Microwave Conference*, 1987.

[II-14]. Uwano, T. O. M. O. K. I., Roberto Sorrentino, and T. A. T. S. U. O. Itoh. "Characterization of strip line crossing by transverse resonance analysis." *IEEE transactions on microwave theory and techniques* 35.12 (1987): 1369-1376.

[II-15]. M. Cohn, "Propagation in a dielectric-loaded parallel plane waveguide," *IRE Transactions on Microwave Theory and Techniques*, vol.7, no.2 pp: 202-208, 1959.

[II-16]. R. Sorrentino, "Numerical techniques for planar and quasi-planar millimeter-wave passive components." *Annals of Telecommunications* 43.7 (1988): 392-404.

[II-17]. J. W. Tao, "A modified transverse-resonance method for the analysis of multilayered, multiconductor quasiplanar structures with finite conductor thickness and mounting grooves," *IEEE Trans. on MTT* Vol.40, pp.1966-1970, Oct.1992.

[II-18]. J.W. Tao, G. Angénieux, B. Flechet, "Full wave description of propagation and losses in quasi planar transmission lines by quasi-analytical solution," *IEEE Trans. on MTT* Vol.42, pp.1246-1253, July 1994.

[II-19]. R. Salik, J. W. Tao, G. Angénieux, & B. Flechet, "A rigorous method to evaluate the electrical performances of MCM interconnections in frequency and time domains," *IEEE -CPMT* Part B: Advanced packaging, February 1996, pp.74-80.

[II-20]. J. W. Tao A. Roussy, P. Febvre, J.C. Villegier, & N. Hadacek, "Full wave frequency dependent inductance estimation for RSFQ applications in NbN multilayer technology," *30th European Microwave Conference,* Paris, Oct. 2000, pp.163-166.

Chapter III SOURCE DRIVEN ANALYSIS IN WAVEGUIDE DISCONTINUITIES

III.1 INTRODUCTION

Wave guiding structures are composite regions often consisting of only uniform or nonuniform waveguide regions but also discontinuity regions as illustrated in Fig.3.1. Discontinuities in waveguide and other microwave transmission lines occurs widely, that are regions wherein there exist discontinuities in cross-section transverse to the direction of propagation, e.g., dielectric waveguides; longitudinal discontinuities, a plane parallel to the longitudinal axis of the waveguide, may occur within or at junction (e.g., step discontinuity) of waveguide regions. The discontinuity effect is unavoidable, sometimes in other cases maybe deliberately introduced into the circuit to perform a certain electrical function (e.g., reactive diaphragm in waveguide, or stubs on a microstrip line for matching or filter circuit), but can be significant enough to warrant characterization.

In any event, microwave circuit can be represented as an equivalent circuit, depending on the type of discontinuity, the equivalent circuit may be simple shunt or series element, or T- or π-equivalent circuit may be needed. The classic reference for waveguide discontinuities and their equivalent circuit and representations is the *Waveguide Handbook* [III-1]. Although approximate equivalent circuits have been developed for the transmission line discontinuities, many do not lend themselves to easy or accurate modelling, and should be treated by numerical analysis. Computational techniques [III-2], based on modern Computer Aid Design packages, are applied for the modelling of discontinuities. In solving a given problem one often uses two or more of numerical methods in conjunction. For example, one might solve a two-dimensional analysis, e.g., approximately by transverse resonance method or transverse operator method, and then use this approximate solution as a good trial field in the variational expression for three-dimensional analysis, for example variational method or multimodal variational method.

In the vicinity of discontinuity, there are evanescent modes excited at each discontinuity or localized diffraction. In any type of cascaded connection of wave guiding structures, there are a forward- and a backward-traveling wave in each section, and each section is long enough so that any evanescent fields presents at discontinuity do not react with the evanescent field of the adjacent discontinuities. It is convenient and straightforward to apply the modal analysis, which is a rigorous and versatile and lend itself well to computer implementation, in the wave guiding structures containing discontinuities. The mode matching method is typically applied to the problem of scattering into waveguiding structures on both sides of discontinuity. At each side of the discontinuity region, the fields on both sides of the discontinuity, constituting a double infinite orthogonal set of liner equations with unknown modal coefficients, are function superposition in respective regions. Like the mode-matching method, multimodal variational method is based on the modal development of transverse electromagnetic field within a waveguide reformulated in terms of the voltage and current amplitudes of a set of mode functions. The difference is that the amplitude coefficients are the combinations of the incident and reflected waves replaced by the quantities proportional to the voltage and current; therefore the admittance operator is introduced and defined in the development for the complete structure.

For the solution process, satisfying the discontinuity boundary condition relation, the continuity condition of the tangential electric and magnetic fields is imposed along the interface of discontinuity. After the orthogonality of the expansion functions is used, by truncating the linear equations to a finite number of terms, the discontinuity matrix will be obtained. As in most modal decomposition techniques, the truncation of eigenmode basis is an important factor for obtaining accurate result, the mode quantity leads to the determination of the eigenfunctions in mode-matching formulation and the accessible modes numbers in the multimodal variational formulation.

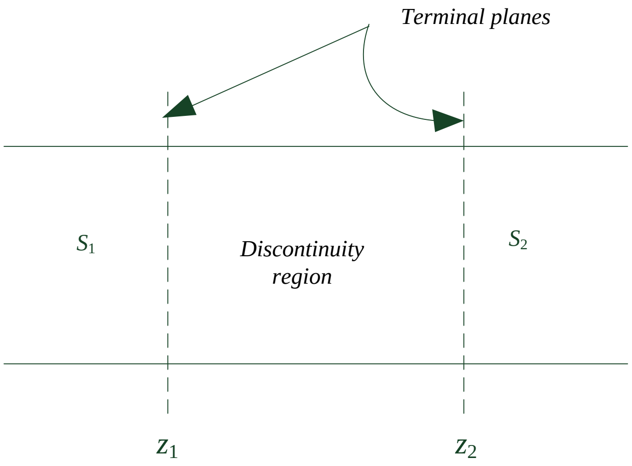

Fig.3.1. Guiding structure containing a discontinuity.

III.2 EIGENMODE BASED SOURCE DRIVEN ANALYSIS

For a discontinuity in a waveguide in Fig.3.2, at a boundary of discontinuity plane where the condition on electric ($\boldsymbol{E}_1$) and magnetic ($\boldsymbol{H}_1$) field were that the tangential components can be continuous across a surface with ε and μ equal to ε_1, μ_1 on one side and ε_2, μ_2 on the other side, the boundary condition on are still the continuity of the tangential components. It is sufficient to match the tangential field components only, since, if the fields satisfy Maxwell's equations, this automatically makes the normal components of the flux vectors satisfy the correct boundary conditions. This changes the relative amplitudes of the fields on the two sides of the discontinuity surface.

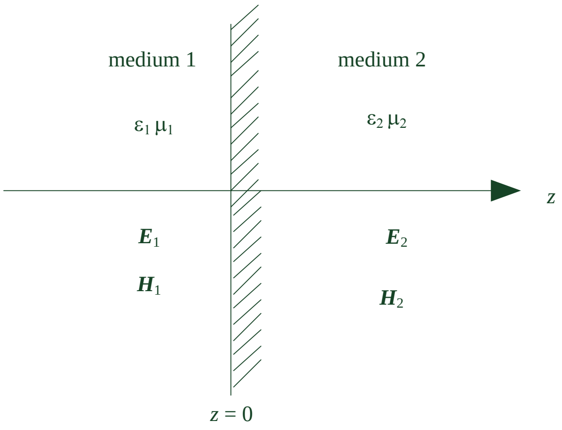

Fig.3.2. Discontinuity plane in a guiding structure.

III.2.1 Mode matching techniques

Mode matching is one of the most often used methods for formulating eigenmode based electromagnetic analysis of discontinuities involving well-defined guiding structures, with the driving source be one or several eigenmodes of constituent guiding components. It has been applied to solve for scattering parameters due to various discontinuities [III-3], parallel plane waveguide **[**III-4], strip dielectric waveguide [III-5] and microstrip line [I-6], [III-7]. It is useful in solving eigenvalue problems in [III-8], which is an extension of mode matching method to analyze the uniaxial anisotropic dielectric resonator. It can be formulated to obtain the resonance frequency of a cavity, the cutoff frequency of a waveguide, or the propagation constant of a transmission line. The detailed procedure of the method was described in the research [III-9] for analytical solutions of the problems. However, only a small class of the problems can be solved with exact solutions. So, all the researchers, who encountered this kind of problems, fell back on the computational technology for the approximate and efficient procedure.

III.2.1.1 Dispersion matrix

The mode matching method is a common method used in the formulation of boundary-value problem. This technique is useful when the geometry of the structure can be identified as a junction of two or more regions, each belonging to a separately coordinate system. In other words, in each region, there exists a set of well-defined solution of Maxwell's equations that satisfies all the boundary conditions except at the junction. When the solutions are orthogonal, they are referred to as the normal modes or eigenmodes. It has been used to analyze complex structures such as filters, impedance transformers in waveguides and power dividers.

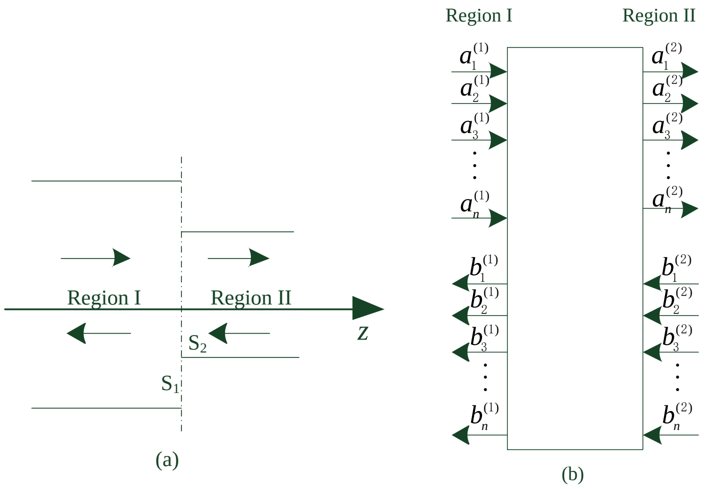

Fig.3.3. Modal analysis (a) longitudinal (b)cross section of junction discontinuity.

The basic principle of mode analysis is field development in term of an infinite series of fundamental mode and higher-order mode at the discontinuity plane between adjoint waveguides. Since the modal functions (e_t and h_t) is known owing to the discussion of propagation constants and field distribution, the problem reduced to that of figuring out double sets of modal coefficients (a_n and b_n) associated with field expansions in regions I and II. In conjunction, by applying the continuity conditions which should satisfy electromagnetic fields, these conditions in association with the orthogonal propriety of each mode lead to an infinite linear equation with unknown coefficients.

For a junction discontinuity in Fig.3.3, we assume that S_1, S_2 denote the transverse cross section for structure I and II, and the cross, unite, difference sections at the discontinuity are defined as:

$$S_c = S_1 \cap S_2 ,\quad S_u = S_1 \cup S_2 ,\quad S_D = S_1 - S_2 .$$

Considering the wave propagating along +z direction and u_z its normal unit vector, we consider modal equations in the framework of boundary conditions, in which electric and magnetic field are considered as linear combination of complexes eigenmodes. At plane z = 0, since the transverse cross section electromagnetic fields are continuous, the total transverse electric field ($\boldsymbol{E}_t$) and the total transverse magnetic field ($\boldsymbol{H}_t$) in term of the forward-and backward-modes are expressed as:

For region I (z < 0)

$$\vec{E}_t^{(1)} = \sum_{n=1}^{\infty}\left(a_n^{(1)} + b_n^{(1)}\right)\vec{e}_{tn}^{(1)}$$

$$\vec{H}_t^{(1)} = \sum_{n=1}^{\infty}\left(a_n^{(1)} - b_n^{(1)}\right)\vec{h}_{tn}^{(1)}$$

For region II (z > 0)

$$\vec{E}_t^{(2)} = \sum_{m=1}^{\infty}\left(a_m^{(2)} + b_m^{(2)}\right)\vec{e}_{tm}^{(2)}$$

$$\vec{H}_t^{(2)} = \sum_{m=1}^{\infty}\left(a_m^{(2)} - b_m^{(2)}\right)\vec{h}_{tm}^{(2)}$$

Here, subscripts *n* and *m* denote mode index in the waveguide I and II, respectively $a_n^{(1)}$, $b_n^{(1)}$ and $a_m^{(2)}$, $b_m^{(2)}$ are the amplitudes of *n*th and *m*th forward- and backward-modes in region I and II. $\boldsymbol{E_t}$, $\boldsymbol{H_t}$ and e_t, h_t are transverse electric/magnetic field and transverse electric/magnetic modal functions. The modal functions satisfy the orthogonality relation defined by

$$\iint_{Su} \vec{u}_z \cdot \left(\vec{e}_{tn}^{(1)} \times \vec{h}_{tp}^{(1)*}\right) ds = \delta_{np} \overline{\overline{N}}_p^{(1)}$$

$$\iint_{Sc} \vec{u}_z \cdot \left(\vec{e}_{tm}^{(2)} \times \vec{h}_{tq}^{(2)*}\right) ds = \delta_{mq} \overline{\overline{N}}_q^{(1)}$$

where δ_{np} and δ_{mq} are the Kronecker delta with N_p and N_q the diagonal matrices. Applying the continuity condition at the junction ($z = 0$), we obtain the equations for electric and magnetic field as

$$\vec{E}_t^{(1)} = \vec{E}_t^{(2)} \quad \left(x, y \in Su\right) \Rightarrow \sum_{n=1}^{\infty}\left(a_n^{(1)} + b_n^{(1)}\right)\vec{e}_{tn}^{(1)} = \sum_{m=1}^{\infty}\left(a_m^{(2)} + b_m^{(2)}\right)\vec{e}_{tm}^{(2)} \tag{3.1}$$

$$\vec{H}_t^{(1)} = \vec{H}_t^{(2)} \quad \left(x, y \in Sc\right) \Rightarrow \sum_{n=1}^{\infty}\left(a_n^{(1)} - b_n^{(1)}\right)\vec{h}_{tn}^{(1)} = \sum_{m=1}^{\infty}\left(a_m^{(2)} - b_m^{(2)}\right)\vec{h}_{tm}^{(2)} \tag{3.2}$$

From (3.1) and (3.2) we can derive a set of equations involving the unknown coefficients and corresponding matrices in Appendix II, by making use of the property of mode orthogonality. We can deduce the integral discontinuity equations into matrix equations, this yield

$$\overline{\overline{N}}_{p}^{(1)}\left(A^{(1)}+B^{(1)}\right)=\overline{\overline{HE}}_{mp}^{(12)}\left(A^{(2)}+B^{(2)}\right) \tag{3.3a}$$

$$\overline{\overline{EH}}_{nq}^{(12)}\left(A^{(1)}+B^{(1)}\right)=\overline{\overline{N}}_{q}^{(2)}\left(A^{(2)}+B^{(2)}\right) \tag{3.3b}$$

$$\overline{\overline{EH}}_{pn}^{(11)*}\left(A^{(1)}-B^{(1)}\right)=\overline{\overline{EH}}_{pm}^{(12)*}\left(A^{(2)}-B^{(2)}\right) \tag{3.3c}$$

$$\overline{\overline{HE}}_{qn}^{(12)*}\left(A^{(1)}-B^{(1)}\right)=\overline{\overline{EH}}_{qm}^{(22)*}\left(A^{(2)}-B^{(2)}\right) \tag{3.3d}$$

where $A^{(i)}$ and $B^{(i)}$ ($i = 1,2$ denotes the two regions) are the column vectors forming of the amplitude coefficients of the modal functions. For special case, the discontinuity sections are same

$$S_1 = S_2 = S_c = S_u$$

Because of $\overline{\overline{EH}}_{pn}^{(11)} = \overline{\overline{N}}_{p}^{(1)}$ and $\overline{\overline{EH}}_{qm}^{(22)} = \overline{\overline{N}}_{q}^{(2)}$.

$$\begin{gathered}
\overline{\overline{N}}^{(1)} A^{(1)} - \overline{\overline{HE}}^{(12)} B^{(1)} = -\overline{\overline{N}}^{(2)} B^{(1)} + \overline{\overline{HE}}^{(12)} A^{(2)} \\
\overline{\overline{HE}}^{(12)*} A^{(1)} + \overline{\overline{N}}^{(2)} B^{(1)} = \overline{\overline{HE}}^{(12)*} B^{(1)} + \overline{\overline{N}}^{(2)*} A^{(2)}
\end{gathered}$$

where * denote the conjugate of original matrix, by applying $\begin{pmatrix} B^{(1)} \\ A^{(1)} \end{pmatrix} = \overline{\overline{S}} \begin{pmatrix} A^{(2)} \\ B^{(2)} \end{pmatrix}$, the final solution of the formation are expressed by scattering parameters defined by

$$\overline{\overline{S}} = \begin{bmatrix} -\overline{\overline{N}}^{(1)} & \overline{\overline{HE}}^{(12)} \\ \overline{\overline{HE}}^{(12)*} & \overline{\overline{N}}^{(2)} \end{bmatrix}^{-1} \begin{bmatrix} \overline{\overline{N}}^{(1)} & -\overline{\overline{HE}}^{(12)} \\ \overline{\overline{HE}}^{(12)*} & \overline{\overline{N}}^{(2)} \end{bmatrix} \tag{3.5}$$

The basis of mode matching technique is the expansion of the electromagnetic field in terms of an infinite series of normal modes as a function of the frequency and dimensions. In practice, the truncation is necessary to get finite size matrices. Then the numerical convergence study will be necessary to each discontinuity.

III.2.1.2 Dispersion matrix of multiple junctions

In the case of propagation in a structure with cascaded discontinuities, we use the principle of associating the individual matrix S of each transition, taking the length into account that separate them. The determination of general S matrix of each transition is given in last section by mode-matching method. To explain the procedure conveniently, we determine the resulting matrix S of the structure formed by two successive junctions in waveguide illustrate in Fig.3.4.

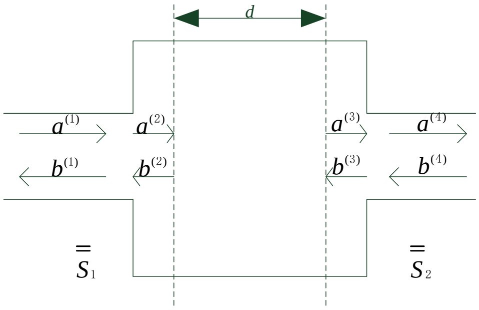

Fig.3.4. Two successive discontinuities of guiding structure.

$\overline{\overline{S}}_1 = \begin{bmatrix} \left[S_{11}^{(1)}\right] & \left[S_{12}^{(1)}\right] \\ \left[S_{21}^{(1)}\right] & \left[S_{22}^{(1)}\right] \end{bmatrix}$ the scattering matrix of first junction;

$\overline{\overline{S}}_2 = \begin{bmatrix} \left[S_{11}^{(2)}\right] & \left[S_{12}^{(2)}\right] \\ \left[S_{21}^{(2)}\right] & \left[S_{22}^{(2)}\right] \end{bmatrix}$ the scattering matrix of second junction;

These two junctions are connected by a waveguide section of the length *d*. The matrix *L* of the transmission line is a diagonal matrix such as

$$\overline{\overline{L}} = \begin{bmatrix} \left[L^{(h)}\right] & 0 \\ 0 & \left[L^{(e)}\right] \end{bmatrix} \tag{3.6}$$

with the diagonal elements of the sub-matrix given by

$$L_n^{(h\,or\,e)} = \exp(-\gamma_m^{(h\,or\,e)} \cdot d)$$

$\gamma_m^{(h\,or\,e)}$ being propagation constants of m^{th} mode. The scattering matrix of two cascaded junctions is joined together as

$$S = \begin{bmatrix} [S_{11}] & [S_{12}] \\ [S_{21}] & [S_{22}] \end{bmatrix} \tag{3.7}$$

with

$$\begin{aligned}
[S_{11}] &= \left[S_{11}^{(1)}\right] + \left[S_{12}^{(1)}\right][L][U_2]\left[S_{11}^{(2)}\right][L]\left[S_{21}^{(2)}\right] \\
[S_{12}] &= \left[S_{12}^{(1)}\right][L][U_2]\left[S_{12}^{(2)}\right] \\
[S_{21}] &= \left[S_{21}^{(2)}\right][L][U_1]\left[S_{21}^{(1)}\right] \\
[S_{22}] &= \left[S_{22}^{(2)}\right] + \left[S_{21}^{(2)}\right][L][U_1]\left[S_{22}^{(1)}\right][L]\left[S_{12}^{(1)}\right]
\end{aligned} \tag{3.8}$$

and

$$\begin{aligned}
[U_1] &= \left([I] - [L]\left[S_{22}^{(1)}\right][L]\left[S_{11}^{(2)}\right]\right)^{-1} \\
[U_2] &= \left([I] - [L]\left[S_{11}^{(2)}\right][L]\left[S_{22}^{(1)}\right]\right)^{-1}
\end{aligned} \tag{3.9}$$

III.2.2 Single mode driven variational formulation

Many works on classical variational methods has been reported in several classical works [III-10]. For the sake of clarity, we separate the *one-port* discontinuities from the *two-port* type in the rest of the discussions. For multi-port type, this will be the subject of the next section.

We note the use of terminology of electrical circuits in a context governed by Maxwell's equations, thus the theory of electromagnetic fields. However, the division in a complex structure of the sections of uniform guides of the junctions serving as a connection makes it possible to assimilate the guides to general transmission lines and the junctions of the multiport, facilitating the analysis and design of the entire structure, since it is treated with known and controlled theories, much less heavy to handle than the rigorous approach developed in this text. This approach is used frequently by engineers and microwave scientists. The interest of our study lies then in the identification of all model elements.

III.2.2.1 Discontinuities considered as one port

The formulations given in [III-10] are based on precise configurations, which gives a better understanding of the problem. For our part, it is preferable to treat a general configuration as above figure. For a guide symmetric to *z*, the fields at a given plane *z* will be given by

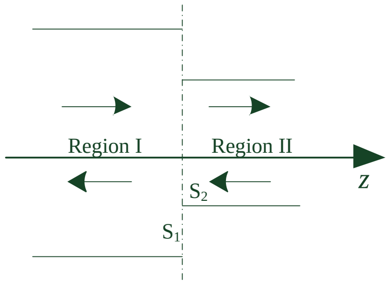

Fig.3.5. One port discontinuities of guiding structure.

$$\mathrm{E}_t\left(x,y,z\right)=\sum\left(A_n^{(p)}e^{-\gamma_n z}+A_n^{(r)}e^{\gamma_n z}\right)\mathrm{e}_{tn}\left(x,y\right)=\sum\frac{v_n\left(z\right)}{\sqrt{\left|N_m\right|}}\mathrm{e}_{tn}\left(x,y\right) \tag{3.10a}$$

$$\mathrm{H}_t\left(x,y,z\right)=\sum\left(A_n^{(p)}e^{-\gamma_n z}-A_n^{(r)}e^{\gamma_n z}\right)\mathrm{h}_{tn}\left(x,y\right)=\sum\frac{i_n\left(z\right)}{\sqrt{\left|N_m\right|}}\mathrm{h}_{tn}\left(x,y\right) \tag{3.10b}$$

From which we can deduce a general admittance operator relation between magnetic and electric field at a same plane by

$$\mathrm{J}\left(x,y,z\right)=\hat{\mathrm{Y}}\mathrm{E}_t\left(x,y,z\right) \tag{3.11}$$

$\hat{Y}=\sum y_n\left(z\right)\hat{Y}_n$ being the admittance operator of a waveguide

$$\hat{Y}_n F=\frac{\mathrm{j}_n\left(x,y\right)}{N_n}\iint_s\hat{\mathrm{j}}_n\left(x,y\right)\cdot\mathrm{F}dS \tag{3.12}$$

$y_n(z)=i_n(z)/v_n(z)$ being the reduced admittance seen at plane z of the mode of order n.

At the discontinuity plane z_0, we have new relation between electric and magnetic field by the following

$$\mathrm{J}_0\left(x,y\right)=\mathrm{J}^{(1)}\left(x,y,z_0\right)+\mathrm{J}^{(2)}\left(x,y,z_0\right)=\left(\hat{Y}^{(1)}+\hat{Y}^{(2)}\right)\mathrm{E}_{t0}\left(x,y\right) \tag{3.13}$$

A variational on $\boldsymbol{E}_{t0}$ is given here:

$$f\left(\mathrm{E}_{t0}\right)=\rangle\mathrm{E}_{t0}\left(x,y\right)\left|\mathrm{J}_0\left(x,y\right)\right\langle=\rangle\mathrm{E}_{t0}\left(x,y\right)\left|\left(\hat{Y}^{(1)}+\hat{Y}^{(2)}\right)\mathrm{E}_{t0}\left(x,y\right)\right\langle \tag{3.14}$$

The junction can be considered as a one port if no mode among those of the output guides propagates. In such cases there will be no energy propagation to the output and the energy contained in the modes of the output guides are of reactive type and are stored around the junction. It is also assumed that only the fundamental mode of the input guide is propagating, which gives

$A_n^{(p1)} = A_m^{(p2i)} = 0$, n=2,3,.... ; m=1, 2, 3,.... ; i=1,2,...,N

The value of the mode admittance is immediately deduced (-1) except that of the input fundamental mode. The stationary form (3.14) then becomes:

$$f\left(\mathrm{E}_{t0}\right) = y_1^{(1)}\left(z_0\right)\rangle \mathrm{E}_{t0}\left|\hat{Y}_1^{(1)}\mathrm{E}_{t0}\right\langle - \rangle \mathrm{E}_{t0}\left|\left(\sum_{n=2}^{\infty}\hat{Y}_n^{(1)} + \sum_{i=1}^{N}\sum_{m=1}^{\infty}\hat{Y}_m^{(2i)}\right)\mathrm{E}_{t0}\right\langle \qquad (3.15)$$

For $\boldsymbol{E}_{t0}$ the exact solution of this problem, the equivalent one port admittance is given by:

$$\begin{aligned} Y_e = y_1^{(1)}\left(z_0\right) &= \frac{\rangle \mathrm{E}_{t0}\left|\left(\sum_{n=2}^{\infty}\hat{Y}_n^{(1)} + \sum_{i=1}^{N}\sum_{m=1}^{\infty}\hat{Y}_m^{(2i)}\right)\mathrm{E}_{t0}\right\langle}{\rangle \mathrm{E}_{t0}\left|\hat{Y}_1^{(1)}\mathrm{E}_{t0}\right\langle} \\ &= jN_1^{(1)}\frac{\iint_S dS \iint_S dS\ \mathrm{E}_{t0}\left(r\right)\cdot G\left(r\middle|r\ \right)\cdot \mathrm{E}_{t0}\left(r\ \right)}{\left(\iint_S \mathrm{j}_1^{(1)}\left(r\right)\cdot \mathrm{E}_{t0}\left(r\right)dS\right)^2} \end{aligned} \qquad (3.16)$$

With $G\left(r\middle|r\ \right) = -j\left\{\sum_{n=2}^{\infty}\frac{\mathrm{j}_n^{(1)}\left(r\right)\mathrm{j}_n^{(1)}\left(r\ \right)}{N_n^{(1)}} + \sum_{i=1}^{N}\sum_{m=1}^{\infty}\frac{\mathrm{j}_m^{(2i)}\left(r\right)\mathrm{j}_m^{(2i)}\left(r\ \right)}{N_m^{(2i)}}\right\}$

The function $G(r|r')$ plays here the role of the Green’s function. When the structure is lossless, $G(r|r')$ is real and Y_e pure imaginary since all normative constants are imaginary. In the case of a single guide at the exit with only modes TE_{n0} on both sides of the discontinuity plane, (3.16) becomes the form given in [[III-10] chap.8] whose stationarity has been demonstrated. The same demonstration can be easy for (3.16) with any modes.

III.2.2.2 Discontinuities considered as two port

Although the discussion can be done with the general case of Fig.3.5, it is preferable, for ease of understanding, to discuss the case of a junction between two guides whose respective fundamental mode is propagating. In this case the relations (3.10) become:

$$\mathrm{E}_{t0} = \frac{v_1^{(1)}}{\sqrt{\left|N_1^{(1)}\right|}}\mathrm{e}_{t1}^{(1)} + \sum_{n=2}^{\infty}A_n^{(r1)}\mathrm{e}_{tn}^{(1)}\left(x,y\right) = \frac{v_1^{(2)}}{\sqrt{\left|N_1^{(2)}\right|}}\mathrm{e}_{t1}^{(2)} + \sum_{m=2}^{\infty}A_m^{(r2)}\mathrm{e}_{tn}^{(2)}\left(x,y\right) \qquad (3.17a)$$

$$\mathrm{J}_0 = \frac{i_1^{(1)}}{\sqrt{\left|N_1^{(2)}\right|}}\,\mathrm{j}_1^{(1)} + \frac{i_1^{(2)}}{\sqrt{\left|N_1^{(2)}\right|}}\,\mathrm{j}_1^{(2)} - \sum_{n=2}^{\infty} A_n^{(r1)}\mathrm{j}_n^{(1)}\left(x,y\right) - \sum_{m=2}^{\infty} A_m^{(r2)}\mathrm{j}_n^{(2)}\left(x,y\right) \qquad (3.17\mathrm{b})$$

Field $\boldsymbol{E}_{\mathrm{t}0}$ depends on the amplitudes of incoming waves on each side of discontinuity and therefore on the current coefficients $i_1^{(1)}$ and $i_1^{(2)}$. We have $E_{t0} = i_1^{(1)}\mathrm{E}_1 + i_1^{(2)}\mathrm{E}_2$. The use of the orthogonality relation (3.11) gives us:

$$v_1^{(1)} = \frac{\sqrt{\left|N_1^{(1)}\right|}}{N_1^{(1)}} \iint_S \mathrm{j}_1^{(1)} \cdot \mathrm{E}_{t0} dS = \sqrt{\left|N_1^{(1)}\right|}\, i_1^{(1)} \left(\frac{1}{N_1^{(1)}} \iint_S \mathrm{j}_1^{(1)} \cdot \mathrm{E}_1 dS \right) + i_1^{(2)} \left(\frac{1}{N_1^{(1)}} \iint_S \mathrm{j}_1^{(1)} \cdot \mathrm{E}_2 dS \right) \qquad (3.18\mathrm{a})$$

$$A_n^{(r1)} = \frac{1}{N_n^{(1)}} \iint_S \mathrm{j}_n^{(1)} \cdot \mathrm{E}_{t0} dS = i_1^{(1)} \left(\frac{1}{N_n^{(1)}} \iint_S \mathrm{j}_n^{(1)} \cdot \mathrm{E}_1 dS \right) + i_1^{(2)} \left(\frac{1}{N_n^{(1)}} \iint_S \mathrm{j}_n^{(1)} \cdot \mathrm{E}_2 dS \right) \qquad (3.18\mathrm{b})$$

$$A_n^{(r1)} = \frac{1}{N_n^{(1)}} \iint_S \mathrm{j}_n^{(1)} \cdot \mathrm{E}_{t0} dS = i_1^{(1)} \left(\frac{1}{N_n^{(1)}} \iint_S \mathrm{j}_n^{(1)} \cdot \mathrm{E}_1 dS \right) + i_1^{(2)} \left(\frac{1}{N_n^{(1)}} \iint_S \mathrm{j}_n^{(1)} \cdot \mathrm{E}_2 dS \right) \qquad (3.18\mathrm{c})$$

$$A_m^{(r2)} = \frac{1}{N_m^{(2)}} \iint_S \mathrm{j}_m^{(2)} \cdot \mathrm{E}_{t0} dS = i_1^{(1)} \left(\frac{1}{N_m^{(2)}} \iint_S \mathrm{j}_m^{(2)} \cdot \mathrm{E}_1 dS \right) + i_1^{(2)} \left(\frac{1}{N_m^{(2)}} \iint_S \mathrm{j}_m^{(2)} \cdot \mathrm{E}_2 dS \right) \qquad (3.18\mathrm{d})$$

We note that $v_1^{(1)}$ and $v_1^{(2)}$ linearly depend on $i_1^{(1)}$ and $i_1^{(2)}$ which corresponds exactly to the definition of a two port whose two inputs with reduced port impedance to 1 at each side. By identification, the elements of the reduced impedance matrix are given by:

$$z_{11} = \frac{\sqrt{\left|N_1^{(1)}\right|}}{N_1^{(1)}} \iint_S \mathrm{j}_1^{(1)} \cdot \mathrm{E}_1 dS, \quad z_{12} = \frac{\sqrt{\left|N_1^{(1)}\right|}}{N_1^{(1)}} \iint_S \mathrm{j}_1^{(1)} \cdot \mathrm{E}_2 dS$$

$$z_{21} = \frac{\sqrt{\left|N_1^{(2)}\right|}}{N_1^{(2)}} \iint_S \mathrm{j}_1^{(2)} \cdot \mathrm{E}_1 dS, \quad z_{22} = \frac{\sqrt{\left|N_1^{(2)}\right|}}{N_1^{(2)}} \iint_S \mathrm{j}_1^{(2)} \cdot \mathrm{E}_2 dS$$

By replacing the coefficients in (3.17b), we have

$$
\begin{aligned}
\frac{i_1^{(1)}}{\sqrt{\left|N_1^{(1)}\right|}}\mathrm{j}_1^{(1)}+\frac{i_1^{(2)}}{\sqrt{\left|N_1^{(2)}\right|}}\mathrm{j}_1^{(2)} &= \sum_{n=2}^{\infty}\left[i_1^{(1)}\left(\frac{1}{N_n^{(1)}}\iint_S \mathrm{j}_n^{(1)}\cdot\mathrm{E}_1 dS\right)+i_1^{(2)}\left(\frac{1}{N_n^{(1)}}\iint_S \mathrm{j}_n^{(1)}\cdot\mathrm{E}_2 dS\right)\right]\mathrm{j}_n^{(1)}(r)\\
&+\sum_{m=2}^{\infty}\left[i_1^{(1)}\left(\frac{1}{N_m^{(2)}}\iint_S \mathrm{j}_m^{(2)}\cdot\mathrm{E}_1 dS\right)+i_1^{(2)}\left(\frac{1}{N_m^{(2)}}\iint_S \mathrm{j}_m^{(2)}\cdot\mathrm{E}_2 dS\right)\right]\mathrm{j}_m^{(2)}(r)\\
&=\iint_S i_1^{(1)}\mathrm{E}_1(r\ )\cdot\left[\sum_{n=2}^{\infty}\frac{1}{N_n^{(1)}}\mathrm{j}_n^{(1)}(r\ )\,\mathrm{j}_n^{(1)}(r)+\sum_{m=2}^{\infty}\frac{1}{N_m^{(2)}}\mathrm{j}_m^{(2)}(r\ )\,\mathrm{j}_m^{(2)}(r)\right]dS\\
&+\iint_S i_1^{(2)}\mathrm{E}_2(r\ )\cdot\left[\sum_{n=2}^{\infty}\frac{1}{N_n^{(1)}}\mathrm{j}_n^{(1)}(r\ )\,\mathrm{j}_n^{(1)}(r)+\sum_{m=2}^{\infty}\frac{1}{N_m^{(2)}}\mathrm{j}_m^{(2)}(r\ )\,\mathrm{j}_m^{(2)}(r)\right]dS
\end{aligned}
\tag{3.19}
$$

We can notice that the two sums between hooks play the role of Green's function and can be noted by:

$$
G(r|r'\ )=-j\left\{\sum_{n=2}^{\infty}\frac{1}{N_n^{(1)}}\mathrm{j}_n^{(1)}(r\ )\,\mathrm{j}_n^{(1)}(r)+\sum_{m=2}^{\infty}\frac{1}{N_m^{(2)}}\mathrm{j}_m^{(2)}(r\ )\,\mathrm{j}_m^{(2)}(r)\right\}
$$

$G(r|r')$ will be real one since all modes are evanescent in our case. As a consequence, all normalization coefficients should be pure imaginary. The choice of the current coefficients being arbitrary, one can obtain from the preceding equation two decoupled equations

$$
\mathrm{j}_1^{(1)}(r)=j\sqrt{\left|N_1^{(1)}\right|}\iint_S \mathrm{E}_1(r\ )\cdot G(r|r'\ )dS \tag{3.20a}
$$

$$
\mathrm{j}_1^{(2)}(r)=j\sqrt{\left|N_1^{(2)}\right|}\iint_S \mathrm{E}_2(r\ )\cdot G(r|r'\ )dS \tag{3.20b}
$$

By multiplying (3.20a) by $\boldsymbol{E}_1(r)$ and integrating it into the cross section, we have

$$
\iint_S \mathrm{E}_1(r)\cdot\mathrm{j}_1^{(1)}(r)dS=j\sqrt{\left|N_1^{(1)}\right|}\iint_S dS\iint_S \mathrm{E}_1(r)\cdot G(r|r\ )\cdot\mathrm{E}_1(r\ )dS
$$

Dividing the two members by $\sqrt{\left|N_1^{(1)}\right|}\left(\iint_S \mathrm{E}_1(r)\cdot\mathrm{j}_1^{(1)}(r)dS\right)^2\Big/N_1^{(1)}$, z_{11} is then given by:

$$
\frac{1}{z_{11}}=jN_1^{(1)}\frac{\iint_S dS\iint_S \mathrm{E}_1(r)\cdot G(r|r\ )\cdot\mathrm{E}_1(r\ )dS}{\left(\iint_S \mathrm{E}_1(r)\cdot\mathrm{j}_1^{(1)}(r)dS\right)^2} \tag{3.21a}
$$

in the same way, we can deduce the other elements of the impedance matrix:

$$\frac{1}{z_{22}} = jN_1^{(2)} \frac{\iint_S dS \iint_S \mathrm{E}_2(r)\cdot G(r|r\,)\cdot \mathrm{E}_2(r\,)dS}{\left(\iint_S \mathrm{E}_2(r)\cdot \mathrm{j}_1^{(2)}(r)dS\right)^2} \tag{3.21b}$$

$$\frac{1}{z_{12}} = \frac{1}{z_{21}} = jN_1^{(1)}N_1^{(2)} \frac{\iint_S dS \iint_S \mathrm{E}_1(r)\cdot G(r|r\,)\cdot \mathrm{E}_2(r\,)dS}{\iint_S \mathrm{E}_1(r)\cdot \mathrm{j}_1^{(1)}(r)dS \iint_S \mathrm{E}_2(r\,)\cdot \mathrm{j}_1^{(2)}(r\,)dS} \tag{3.21c}$$

All the elements given here are stationary with respect to $\boldsymbol{E}_1$ and $\boldsymbol{E}_2$.

III.2.2.3 Numerical resolution

The establishment of variational relations (3.16) and (3.21a) is the starting point for calculating the elements of one port or two ports. We need to approximate the electric fields to the discontinuity plane by using a series of functions, the *trial functions* (or *test functions*). In the case of (3.16), we pose

$$\mathrm{E}_{t0}(r) = \sum_{q=1}^{\infty} c_q \mathrm{f}_q(r) \tag{3.22}$$

From (3.16) and (3.22), by introducing $B_e = -jY_e$ the input susceptance, we have

$$\frac{B_e}{N_1^{(1)}}\left(\sum_{q=1}^{\infty} c_q \iint_S \mathrm{j}_1^{(1)}(r)\cdot \mathrm{f}_q(r)dS\right)^2 = \sum_{p,q=1}^{\infty} c_p c_q \iint_S dS \iint_S dS\, \mathrm{f}_p(r)\cdot G(r|r\,)\cdot \mathrm{f}_q(r\,)$$

By using

$u_q = \iint_S \mathrm{j}_1^{(1)}(r)\cdot \mathrm{f}_q(r)dS,\ g_{pq} = \iint_S dS \iint_S dS\, \mathrm{f}_p(r)\cdot G(r|r\,)\cdot \mathrm{f}_q(r\,), b = B_e / N_1^{(1)}$, we can rewrite the previous equation in a more compact form:

$$b\left(\sum_{q=1}^{\infty} u_q c_q\right)^2 - \sum_{p,q=1}^{\infty} g_{pq} c_p c_q = 0 \tag{3.23}$$

The stationary nature of (3.16) requires that the partial derivative of (3.23) with respect to c_k be zero, $k = 1, 2, ...$, which leads to a system of linear equations:

$$\sum_{q=1}^{\infty}\left(bu_k u_q - g_{kq}\right)c_q = 0 \tag{3.24}$$

With k=1,2,....

The solution $\boldsymbol{E}_t(r)$=0 does not provide any useful information, therefore the development coefficients must not all be zero. (3.24) being homogeneous equation, for which a solution satisfying these conditions leads to the nullity of the determinant of the system, which in turn depends on *b*.

We can write (3.24) in matrix form as follows:

$$b\bar{U}\bar{U}^T\bar{C}-\bar{\bar{G}}\bar{C}=0,\;\; \bar{C}=[c_1\; c_2\; c_3 ...\; c_N]^T, \bar{U}^T=[u_1\; u_2\; u_3 ...\; u_N] \tag{3.25}$$

In the case where the matrix $\bar{\bar{G}}$ is not singular one, the value of *b* will be given directly by:

$$\frac{1}{b}=\bar{U}^T\bar{\bar{G}}^{-1}\bar{U} \tag{3.26}$$

If the eigenmodes of the first guide are used as test functions, we will have $u_1=N_1^{(1)}$, $u_k=0$, $k=2,3,...$, according to the orthogonality relation (3.11). A simple manipulation on the calculation of the determinant allows the computation of *b* in the form of the ratio of two determinants as the following:

$$B_e=\frac{1}{N_1^{(1)}}\begin{vmatrix} g_{11} & \cdots & g_{1N} \\ \cdots & \cdots & \cdots \\ g_{N1} & \cdots & g_{NN} \end{vmatrix} \Bigg/ \begin{vmatrix} g_{22} & \cdots & g_{2N} \\ \cdots & \cdots & \cdots \\ g_{N2} & \cdots & g_{NN} \end{vmatrix} \tag{3.27}$$

The same procedure applies to equation (3.16). Assuming the output is closed by a short circuit, we have:

$$\sum_{q=1}^{\infty}\left(bu_k u_q+g_{kq}^{(11)}\right)c_q-\sum_{q=1}^{\infty}g_{kq}^{(12)}d_q=0 \tag{3.28a}$$

$$\sum_{p=1}^{\infty}g_{pm}^{(12)}c_p+\sum_{p=1}^{\infty}g_{pm}^{(22)}d_p=0 \tag{3.28b}$$

with *k*=1,2,3,..and *m*=1,2,3,...

$$\mathrm{E}_{t1}\left(r\right)=\sum_{q=1}^{\infty}c_q\phi_q\left(r\right),\; \mathrm{E}_{t2}\left(r\right)=\sum_{q=1}^{\infty}d_q\varphi_q\left(r\right)$$

$$g_{pq}^{(11)}=\iint_S dS\iint_S dS\; \phi_p\left(r\right)\cdot G^{(11)}\left(r\middle|r\;\right)\cdot\phi_q\left(r\;\right)$$

$$g_{pq}^{(12)}=\iint_S dS\iint_S dS\; \phi_p\left(r\right)\cdot G^{(12)}\left(r\middle|r\;\right)\cdot\varphi_q\left(r\;\right)$$

$$g_{pq}^{(22)} = \iint_S dS \iint_S dS\ \varphi_p\left(r\right)\cdot G^{(22)}\left(r\,|\,r\ \right)\cdot \varphi_q\left(r\ \right)$$

$$u_q = \iint_S \mathrm{j}_1^{(1)}\left(r\right)\cdot \phi_q\left(r\right)dS,$$

$$b = -j\,\frac{y_1^{(1)}\left(z_1\right)}{N_1^{(1)}}$$

Green's functions are all real and are given by:

$$G^{(11)}\left(r\,|\,r\ \right) = j\sum_{n=2}^{\infty}\frac{\mathrm{j}_n^{(1)}\left(r\right)\mathrm{j}_n^{(1)}\left(r\ \right)}{N_n^{(1)}} - j\sum_{m=1}^{\infty} y_m^{(2d)}\,\frac{\mathrm{j}_m^{(2)}\left(r\right)\mathrm{j}_m^{(2)}\left(r\ \right)}{N_m^{(2)}}$$

$$G^{(22)}\left(r\,|\,r\ \right) = j\sum_{n=1}^{\infty} y_n^{(3)}\left(z_2\right)\frac{\mathrm{j}_n^{(3)}\left(r\right)\mathrm{j}_n^{(3)}\left(r\ \right)}{N_n^{(1)}} + j\sum_{m=1}^{\infty} y_m^{(2d)}\,\frac{\mathrm{j}_m^{(2)}\left(r\right)\mathrm{j}_m^{(2)}\left(r\ \right)}{N_m^{(2)}}$$

$$G^{(12)}\left(r\,|\,r\ \right) = j\sum_{m=1}^{\infty} y_m^{(2o)}\,\frac{\mathrm{j}_m^{(2)}\left(r\right)\mathrm{j}_m^{(2)}\left(r\ \right)}{N_m^{(2)}}$$

It should be noted that $y_\mathrm{n}^{(3)}$ is (-1) except for $n = 1$ for which the admittance is related to the ended short-circuit.

The resolution of (3.28) will be the same as that of (3.24). A similar calculation gives us

$$\frac{1}{b} = \bar{U}^T \bar{\bar{G}}^{-1}\bar{U} \qquad (3.29)$$

with $\bar{\bar{G}} = \bar{\bar{G}}^{(11)} + \bar{\bar{G}}^{(12)}\bar{\bar{G}}^{(22)-1}\bar{\bar{G}}^{(12)T}$.

III.2.3 Multimode variational formulation

The initial idea of this study is as follows: a discontinuity can be modeled by a one-port or a two-ports, provided that:

a) the frequency band in which these models are used verifies the existence of only one or two (for the two-port case) propagating modes;

b) the driving point and the end load are placed theoretically infinitely with respect to the discontinuity plane, in practice far enough so that all the evanescent waves generated by the discontinuity are completely attenuated before reaching the driving source on one side and the end load of the other.

Unfortunately, these conditions are not satisfied for devices operating in multimode or for those using multiple discontinuities close each other. A more general study is therefore necessary, by taking a certain number of "accessible" modes on either side of the discontinuity, that is to say modes that can be coupled with adjacent discontinuities. These considerations culminated in the development of the multimodal variational method whose initial form dealing only with discontinuities consisting of homogeneous guides was presented in [III-11] and [III-12]. Much work has been done since [III-13]-[III-21]. We will give a revision of this formulation and some extensions in the continuation of this section.

III.2.3.1 Discontinuities formed by two constituent guides

We take again the stationary form (3.14) with a guide on each side of the discontinuity:

$$f\left(\mathrm{E}_{t0}\right) = \rangle \mathrm{E}_{t0} \left| \left(\sum_{n=1}^{\infty} y_n^{(1)}\left(z_0\right) \hat{Y}_n^{(1)} + \sum_{m=1}^{\infty} y_m^{(2)}\left(z_0\right) \hat{Y}_m^{(2)} \right) \mathrm{E}_{t0} \right\langle$$

Contrary to the hypothesis leading to the establishment of one port and two port models, we consider *L* modes accessible at the input and *K* modes at the output. Accessible modes can be propagating or just below their cutoff frequency; but in any case, everyone is considered a generalized transmission line. The modes being classified according to their increasing cutoff frequency, we then have

$A_n^{(p1)} = A_m^{(p2)} = 0$, $n=L+1, L+2, \ldots ; m=K+1, K+2, \ldots$

From which $y_n^{(1)} = y_m^{(2)} = -1$ for the same index

$$\begin{aligned} f\left(\mathrm{E}_{t0}\right) = \rangle \mathrm{E}_{t0} & \left| \left(\sum_{n=1}^{L} y_n^{(1)}\left(z_0\right) \hat{Y}_n^{(1)} + \sum_{m=1}^{K} y_m^{(2)}\left(z_0\right) \hat{Y}_m^{(2)} \right) \mathrm{E}_{t0} \right\langle \\ & - \rangle \mathrm{E}_{t0} \left| \left(\sum_{n=L+1}^{\infty} \hat{Y}_n^{(1)} + \sum_{m=K+1}^{\infty} \hat{Y}_m^{(2)} \right) \mathrm{E}_{t0} \right\langle \end{aligned} \tag{3.30}$$

By decomposing the field at the discontinuity plane ***E***$_{t0}$ on a given basis,

$$\mathrm{E}_{t0}\left(r\right)=\sum_{q=1}^{\infty}c_q\mathrm{f}_q\left(r\right)$$

(3.30) now depends on the coefficients c_q. The stationary nature of (3.30) then leads to the following system of linear equations:

$$\sum_{q}B_{pq}c_q=0 \tag{3.31}$$

with p=1,2,3,....

$$jB_{pq}=\sum_{n=1}^{L}y_n^{(1)}\left(z_0\right)\rangle f_p\left|\hat{Y}_n^{(1)}f_q\right\langle+\sum_{m=1}^{K}y_m^{(2)}\left(z_0\right)\rangle f_p\left|\hat{Y}_m^{(2)}f_q\right\langle-\sum_{n=L+1}^{\infty}\rangle f_p\left|\hat{Y}_n^{(1)}f_q\right\langle-\sum_{m=K+1}^{\infty}\rangle f_p\left|\hat{Y}_m^{(2)}f_q\right\langle$$

We want to separate in (3.31) the "unknowns" from the "known" ones. For this we define the following matrices:

$$Q_{pq}=-j\left\{\sum_{n=L+1}^{\infty}\rangle\mathrm{f}_p\left|\hat{Y}_n^{(1)}\mathrm{f}_q\right\langle+\sum_{m=K+1}^{\infty}\rangle\mathrm{f}_p\left|\hat{Y}_m^{(2)}\mathrm{f}_q\right\langle\right\}$$

$$U_{pn}^{(1)}=\rangle\mathrm{f}_p\left|\mathrm{j}_n^{(1)}\right\langle,\quad n=1,\ 2,..,\ L$$

$$U_{pm}^{(2)}=\rangle\mathrm{f}_p\left|\mathrm{j}_m^{(2)}\right\langle,\quad m=1,\ 2,...,\ K$$

$$\overline{\overline{N}}^{(\nu)}=\begin{bmatrix}N_1^{(\nu)} & 0 & 0\\ 0 & ... & 0\\ 0 & 0 & N_{L\text{ ou }K}^{(\nu)}\end{bmatrix},\quad \overline{\overline{Y}}^{(\nu)}=\begin{bmatrix}y_1^{(\nu)}\left(z_0\right) & 0 & 0\\ 0 & ... & 0\\ 0 & 0 & y_{L\text{ ou }K}^{(\nu)}\left(z_0\right)\end{bmatrix},\quad \nu=1\text{ or }2$$

The matrix $\overline{\overline{B}}$ is written in the following form:

$$\overline{\overline{B}}=-j\left(\overline{\overline{U}}^{(1)}\overline{\overline{Y}}^{(1)}\overline{\overline{N}}^{(1)-1}\overline{\overline{U}}^{(1)T}+\overline{\overline{U}}^{(2)}\overline{\overline{Y}}^{(2)}\overline{\overline{N}}^{(2)-1}\overline{\overline{U}}^{(2)T}\right)-\overline{\overline{Q}} \tag{3.32}$$

We can rearrange (3.31) using the decomposition of $\overline{\overline{B}}$:

$$-j\left(\overline{\overline{U}}^{(1)}\overline{\overline{Y}}^{(1)}\overline{\overline{N}}^{(1)-1}\overline{\overline{U}}^{(1)T}+\overline{\overline{U}}^{(2)}\overline{\overline{Y}}^{(2)}\overline{\overline{N}}^{(2)-1}\overline{\overline{U}}^{(2)T}\right)\overline{C}=\overline{\overline{Q}}\overline{C} \tag{3.33}$$

By making use of the following matrices:

$$\overline{T} = \begin{bmatrix} \overline{\overline{U}}^{(1)T} \\ \overline{\overline{U}}^{(2)T} \end{bmatrix} \overline{C},\ \ \overline{\overline{N}} = \begin{bmatrix} \overline{\overline{N}}^{(1)} & 0 \\ 0 & \overline{\overline{N}}^{(2)} \end{bmatrix},\ \ \overline{\overline{Y}} = \begin{bmatrix} \overline{\overline{Y}}^{(1)} & 0 \\ 0 & \overline{\overline{Y}}^{(2)} \end{bmatrix}$$

We have

$$\left(j\overline{\overline{\Gamma}}.\overline{\overline{Y}}.\overline{\overline{N}}^{-1} + \overline{\overline{I}} \right)\overline{T} = \overline{0},\ \ \overline{\overline{\Gamma}} = \begin{bmatrix} \overline{\overline{U}}^{(1)T}\overline{\overline{Q}}^{-1}\overline{\overline{U}}^{(1)} & \overline{\overline{U}}^{(1)T}\overline{\overline{Q}}^{-1}\overline{\overline{U}}^{(2)} \\ \overline{\overline{U}}^{(2)T}\overline{\overline{Q}}^{-1}\overline{\overline{U}}^{(2)} & \overline{\overline{U}}^{(2)T}\overline{\overline{Q}}^{-1}\overline{\overline{U}}^{(2)} \end{bmatrix} = \begin{bmatrix} \overline{\overline{\mathrm{A}}} & \overline{\overline{\mathrm{B}}} \\ \overline{\overline{\mathrm{B}}}^{T} & \overline{\overline{\mathrm{A}}} \end{bmatrix} \quad (3.34)$$

Let's go back to our initial concern, which is the definition of a multiport model. Assume that all multiport accesses are normalized by the impedance characteristics of the respective lines, the reduced admittance matrix will be defined by:

$$\overline{I} = \overline{\overline{y}}\overline{V},\ \overline{I}^{T} = \begin{bmatrix} i_1^{(1)} & \dots & i_L^{(1)} & i_1^{(2)} & \dots & i_K^{(2)} \end{bmatrix},\ \overline{V}^{T} = \begin{bmatrix} v_1^{(1)} & \dots & v_L^{(1)} & v_1^{(2)} & \dots & v_K^{(2)} \end{bmatrix} (3.35)$$

Now, there is a relationship between the voltage coefficients and the vector *T*:

$$\overline{T} = \overline{\overline{N}} \left| \overline{\overline{N}} \right|^{-1/2} \overline{V}$$

From (3.34), we write, using the relation $\overline{I} = \overline{\overline{Y}}\overline{V}$:

$$j\overline{\overline{N}}^{-1} \left| \overline{\overline{N}} \right|^{1/2} \overline{\overline{\Gamma}}. \left| \overline{\overline{N}} \right|^{-1/2} \overline{\overline{Y}}\overline{V} = j\overline{\overline{N}}^{-1} \left| \overline{\overline{N}} \right|^{1/2} \overline{\overline{\Gamma}} \left| \overline{\overline{N}} \right|^{-1/2} .\overline{I} = -\overline{V} \quad (3.36)$$

We can immediately identify the reduced impedance matrix of the multiport

$$\overline{\overline{z}} = -j\overline{\overline{N}}^{-1} \left| \overline{\overline{N}} \right|^{1/2} .\overline{\overline{\Gamma}}. \left| \overline{\overline{N}} \right|^{-1/2} \quad (3.37)$$

Other matrices associated with a multiport, such as scattering matrices, can be easily deduced from that of impedance. We can easily verify that, if we put $L = 1$ and $K = 0$, (3.37) will be identical to (3.26), we return to the case of classical variational formulations.

III.2.3.2 Cascade discontinuity

Let's start with a double discontinuity (Fig.3.6) with continuity relation at two discontinuity planes

$$J_d(z_1) = J^{(1)}(z_1) + J^{(2d)}(z_1) = \left(\sum y_n^{(1)}(z_1) Y_n^{(1)} + \sum \frac{i_m^{(2d)}(z_1)}{v_m^{(2d)}(z_1)} Y_m^{(2)} \right) E_t(z_1) \quad (3.38a)$$

$$J_d(z_2) = J^{(2f)}(z_2) + J^{(3)}(z_2) = \left(\sum \frac{i_m^{(2f)}(z_2)}{v_m^{(2f)}(z_2)} Y_m^{(2)} + \sum y_n^{(1)}(z_1) Y_n^{(3)} \right) E_t(z_2) \quad (3.38b)$$

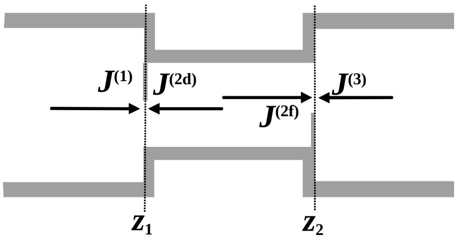

Fig.3.6. Double discontinuity with a guide section in the centre.

By using the relations between the coefficients of currents and voltages at two ends of the guide in the center part, one can get the following equation:

$$\begin{bmatrix} \mathrm{J}_d(z_1) \\ \mathrm{J}_d(z_2) \end{bmatrix} = \begin{bmatrix} \hat{Y}^{(11)} & \hat{Y}^{(12)} \\ \hat{Y}^{(21)} & \hat{Y}^{(22)} \end{bmatrix} \begin{bmatrix} E_t(z_1) \\ E_t(z_2) \end{bmatrix} \quad (3.39)$$

With

$$\hat{Y}^{(11)} = \sum y_n^{(1)}(z_1) \hat{Y}_n^{(1)} + \sum y_m^{(2d)}(l) \hat{Y}_m^{(2)}$$

$$\hat{Y}^{(22)} = \sum y_n^{(3)}(z_2) \hat{Y}_n^{(3)} + \sum y_m^{(2d)}(l) \hat{Y}_m^{(2)}$$

$$\hat{Y}^{(12)} = \hat{Y}^{(21)} = \sum y_m^{(2o)}(l) \hat{Y}_m^{(2)}$$

The corresponding variational form is then

$$f\left(\mathrm{E}_t(z_1), \mathrm{E}_t(z_2)\right) = \rangle \left[\mathrm{E}_t(z_1) \ \mathrm{E}_t(z_2) \right] \begin{bmatrix} \hat{Y}^{(11)} & \hat{Y}^{(12)} \\ \hat{Y}^{(21)} & \hat{Y}^{(22)} \end{bmatrix} \begin{bmatrix} \mathrm{E}_t(z_1) \\ \mathrm{E}_t(z_2) \end{bmatrix} \langle \quad (3.40)$$

By decomposing $\boldsymbol{E}_{t1}$ and $\boldsymbol{E}_{t2}$ on two bases of the test functions as following:

$$\mathrm{E}_{t1} = \sum_{\mathrm{q}} c_q^{(1)} \mathrm{g}_q^{(1)} \ ; \ \mathrm{E}_{t1} = \sum_{\mathrm{q}} c_q^{(2)} \mathrm{g}_q^{(2)}$$

we obtain the following system of linear equations:

$$\sum_q B_{pq}^{(11)} c_q^{(1)} + B_{pq}^{(12)} c_q^{(2)} = 0, \;\; p = 1,2,3... \tag{3.41a}$$

$$\sum_q B_{pq}^{(21)} c_q^{(1)} + B_{pq}^{(22)} c_q^{(2)} = 0, \;\; q = 1,2,3... \tag{3.41b}$$

with:

$$jB_{pq}^{(11)} = \sum_{n=1}^{\infty} y_n^{(1)}(z_1) \rangle g_p^{(1)} \left| \hat{Y}_n^{(1)} g_q^{(1)} \right\langle + \sum_{m=1}^{\infty} y_m^{(2d)}(l) \rangle g_p^{(1)} \left| \hat{Y}_m^{(2)} g_q^{(1)} \right\langle$$

$$jB_{pq}^{(22)} = \sum_{n=1}^{\infty} y_n^{(3)}(z_2) \rangle g_p^{(2)} \left| \hat{Y}_n^{(3)} g_q^{(2)} \right\langle + \sum_{m=1}^{\infty} y_m^{(2d)}(l) \rangle g_p^{(2)} \left| \hat{Y}_m^{(2)} g_q^{(2)} \right\langle$$

$$jB_{pq}^{(12)} = \sum_{m=1}^{\infty} y_m^{(2o)}(l) \rangle g_p^{(1)} \left| \hat{Y}_m^{(2)} g_q^{(2)} \right\langle \; ; \; jB_{pq}^{(21)} = \sum_{m=1}^{\infty} y_m^{(2o)}(l) \rangle g_p^{(2)} \left| \hat{Y}_m^{(2)} g_q^{(1)} \right\langle = jB_{qp}^{(12)}$$

The corresponding overall impedance matrix can be deduced easily as for the one discontinuity case.

III.3 NUMERICAL RESULTS

In last section, mode-matching and multimodal variational methods are presented to characterize the single and multiple discontinuities between uniaxial guiding structures. These methods will be used to direct analysis of two main structures for dielectric material characterization: enlarged coaxial cell and multi-layered microstrip cell. The numerical results will be introduced to inverse modelling of each measurement cells for the purpose of dielectric permittivity extraction from scattering parameter measurement.

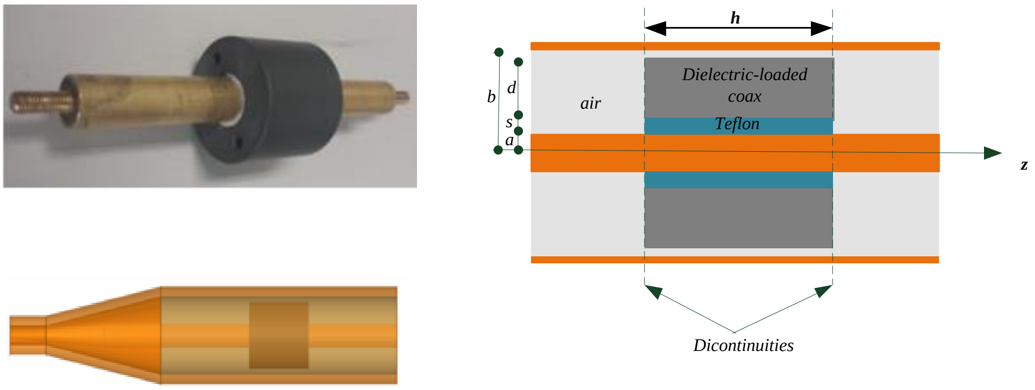

Fig.3.7. Longitudinal discontinuities in the enlarged coaxial line (three-layered).

III.3.1 Discontinuity analysis of coaxial structures discontinuity

This part is devoted to the application of discontinuity analysis methods to enlarged coaxial cell. In the following we show a photo of the centre part of coaxial measurement cell without outer conductor, a figure of the overall measurement cell including the standard N connector to enlarged coaxial line transition, and the discontinuity between empty enlarged coaxial line and sample loaded coaxial structure. The last structure will be studied by methods described in the last section. Comparison will be also taken with commercial software simulation results.

III.3.1.1 Calculation of coupling matrices

When eigenmode based discontinuity analysis technique is chosen, the cross-coupling element between eigenmodes at each side of discontinuity interface is the key element. Before this calculation we will first study the field distribution at each side.

- Field distribution at empty coaxial line

The studied enlarged coaxial cell is homogeneous and uniform guide according to the direction of propagation (o-z). As the measurement cell has azimuthally symmetry and the driven source is TEM mode, electromagnetic field having no φ variation, ∂/∂φ = 0. Then the modal expansion will be effectuated with *TEM*, TM_{m0} and TE_{n0} modes. The expressions of the corresponding basic functions are analytical and available in the literatures, whose basic transverse electric functions are expressed, separately, by

$$\begin{aligned} e_\rho(\rho) &= \frac{V_0}{ln(b/a)}\frac{1}{\rho} \\ h_\varphi(\rho) &= \frac{1}{Z_0}\frac{V_0}{ln(b/a)}\frac{1}{\rho} \end{aligned} \tag{3.55}$$

$$\begin{aligned} e_\rho^{(e)}(\rho) &= \frac{\gamma_m^{(e)}}{k_c}\left(AJ_1(k_c\rho)+BY_1(k_c\rho)\right) \\ h_\varphi^{(e)}(\rho) &= \frac{j2\pi f\varepsilon_0}{k_c}\left(AJ_1(k_c\rho)+BY_1(k_c\rho)\right) \end{aligned} \tag{3.56}$$

$$\begin{aligned} h_\rho^{(h)}(\rho) &= \frac{\gamma_n^{(h)}}{k_c}\left(AJ_1(k_c\rho)+BY_1(k_c\rho)\right) \\ e_\varphi^{(h)}(\rho) &= \frac{-j2\pi f\mu_0}{k_c}\left(AJ_1(k_c\rho)+BY_1(k_c\rho)\right) \end{aligned} \tag{3.57}$$

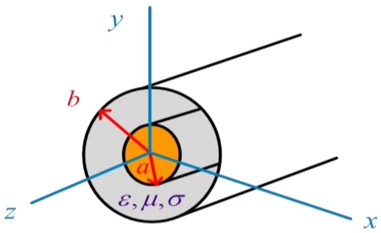

Fig.3.8. Cross-section of enlarged coaxial line geometry.

here V_0 is potential (volts) at the outer conductor; and Z_0 the characteristic impedance of *TEM* mode. (*e/h*) denote mode type for *TM/TE* modes and subscript being m^{th}/n^{th} modes. γ represents the propagation constants of fundamental mode and evanescent modes, and k_c denotes the wave number of each mode defined by the transcendental equations

$J_0(k_ca)Y_0(k_cb)=J_0(k_cb)Y_0(k_ca)$ for higher-order modes TM_{m0}

$J_0'(k_ca)Y_0'(k_cb)=J_0'(k_cb)Y_0'(k_ca)$ for TE_{n0} modes.

- *Field distribution at partially filled coaxial structure*

Again, we consider only azimuthally symmetry solutions. To ensure that the analytical results be correct, all the numerical results of the propagation constants and field distributions of the higher order modes are compared with that of simulation results by COMSOL.

The calculation on cut off frequencies obtained from TOM has been already successfully compared to those of COMSOL in the chapter II as well as the dispersion relations. For the need of discontinuity study, we will show the numerical result on the radial variation of field component in partially filled coaxial structure.

For TM modes, when we found out the 3 components of the electromagnetic field E_ρ, H_φ and E_z by calculating the relative matrix **M** as a function of radius $\rho\boldsymbol{\rho}$, and at the same time, H_ρ, E_φ and H_z are always zero. For TE modes, when we calculate the second function in terms of matrix **N**, the 3 components of the electromagnetic field H_ρ, E_φ and H_z are as a function of radius ρ, and at the same time, E_ρ, H_φ and E_z are always be zero.

For TM_{01} and TE_{01} modes, we first choose to work at 3GHz. By transverse operator method, we obtained the propagation constants, γ/k_0 = 0.554i for TM_{01} mode and γ/k_0 = 0.519i for TE_{01} mode. In mode analysis by simulator COMSOL, effective mode indexes are n=0.553998 for TM_{01} mode and n=0.519502 for TE_{01} mode. For TM_{01} mode, the field components have been calculated and compared in the Fig.3.9. All the field components are normalized by H_φ at the inner conductor, obtained by each method so H_φ in the inner conductor is equals to 1.

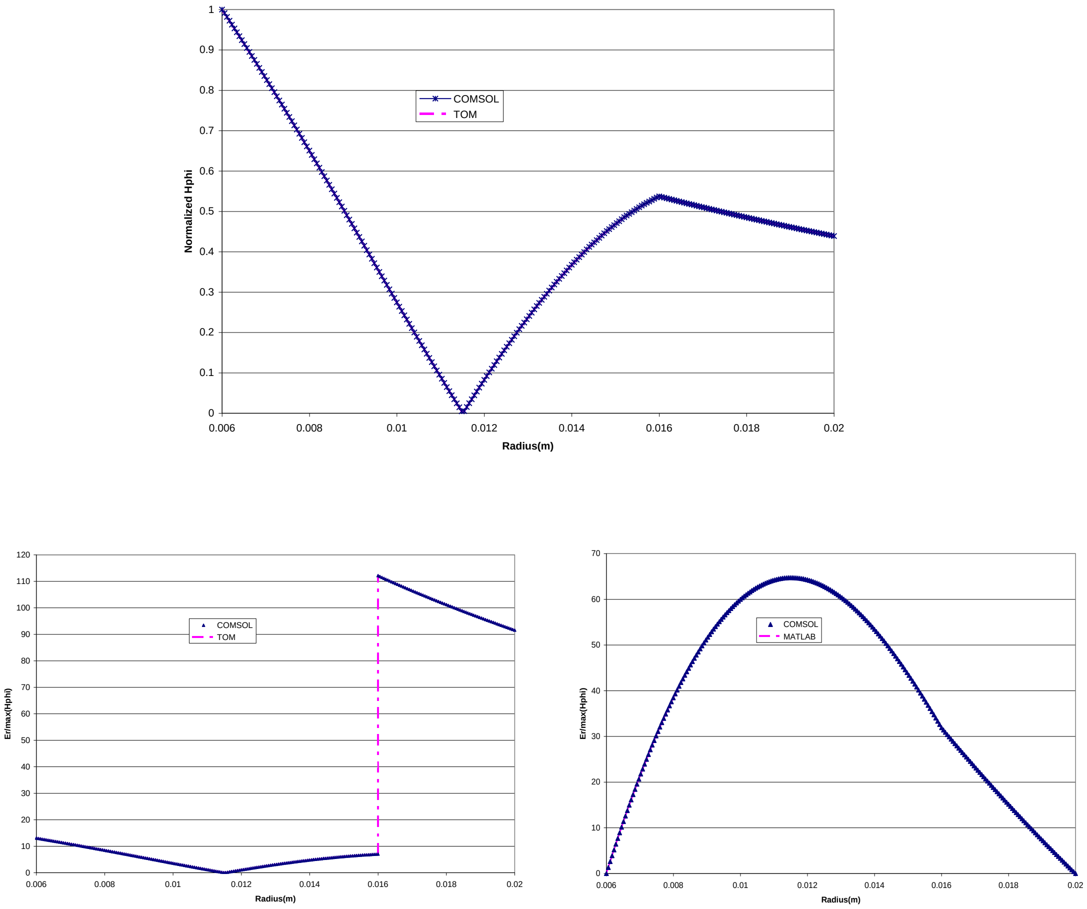

Fig.3.9. Field distributions of TM_{01}.

For TE_{01} mode, we normalized all the field components by H_z to be 1. All the field distributions compared with the results from COMSOL in Fig.3.10.

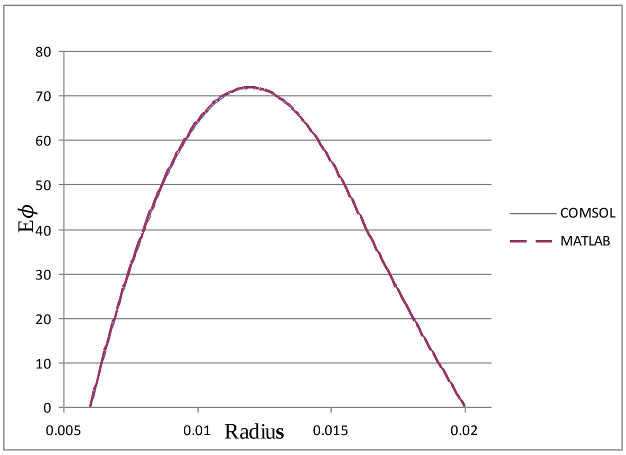

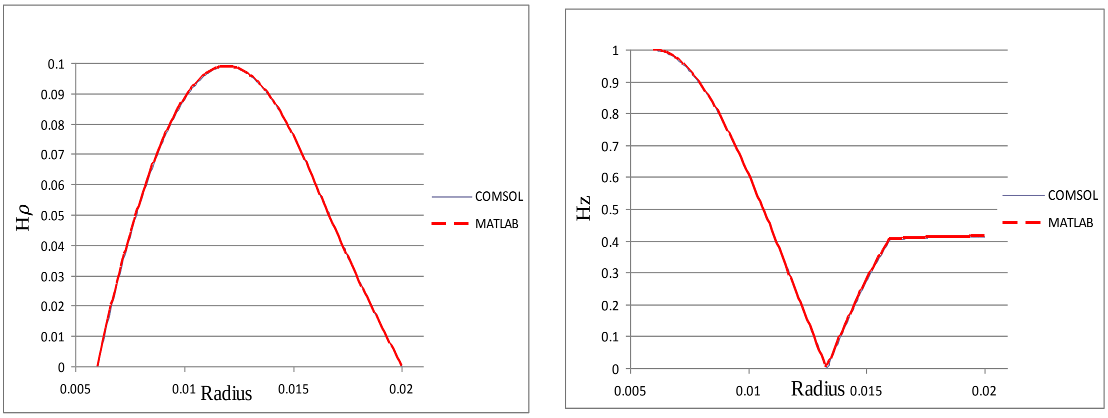

Fig.3.10. Field distributions of TE_{01}.

For TM_{02} and TE_{02} modes, these two modes propagated at the frequency f = 7GHz. By transverse operator method, we obtained the propagation constants, $\gamma/k_0 = 0.861i$ for TM_{02} mode and $\gamma/k_0 = 1.708i$ for TE_{02} mode. In mode analysis, the effective mode indexes are n = 0.861483 for TM_{02} mode and n = 1.707719 for TE_{02} mode. For TM_{02} mode, we normalized all the field components by H_φ, which means H_φ in the inner conductor is equals to 1. All the field distributions compared with the results from COMSOL in Fig.3.11.

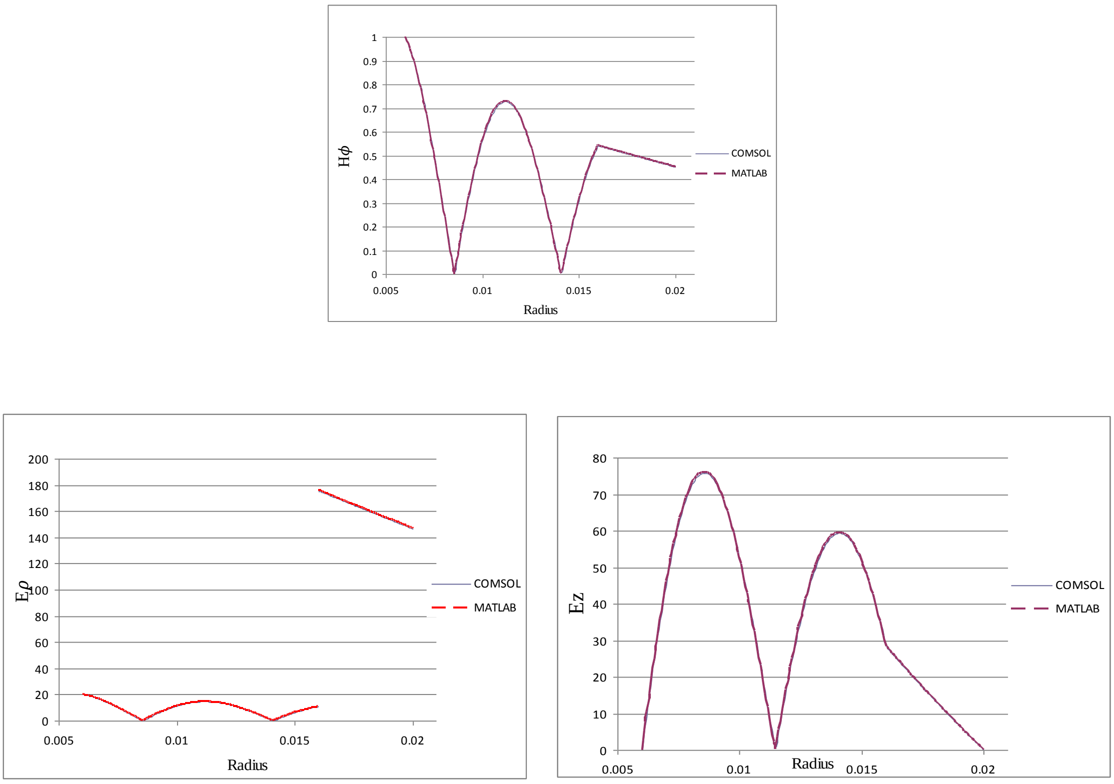

Fig.3.11. Field distributions of TM_{02}.

For TE_{02} mode, we normalized all the field components by H_z. All the field distributions compared with the results from COMSOL in Fig.3.12.

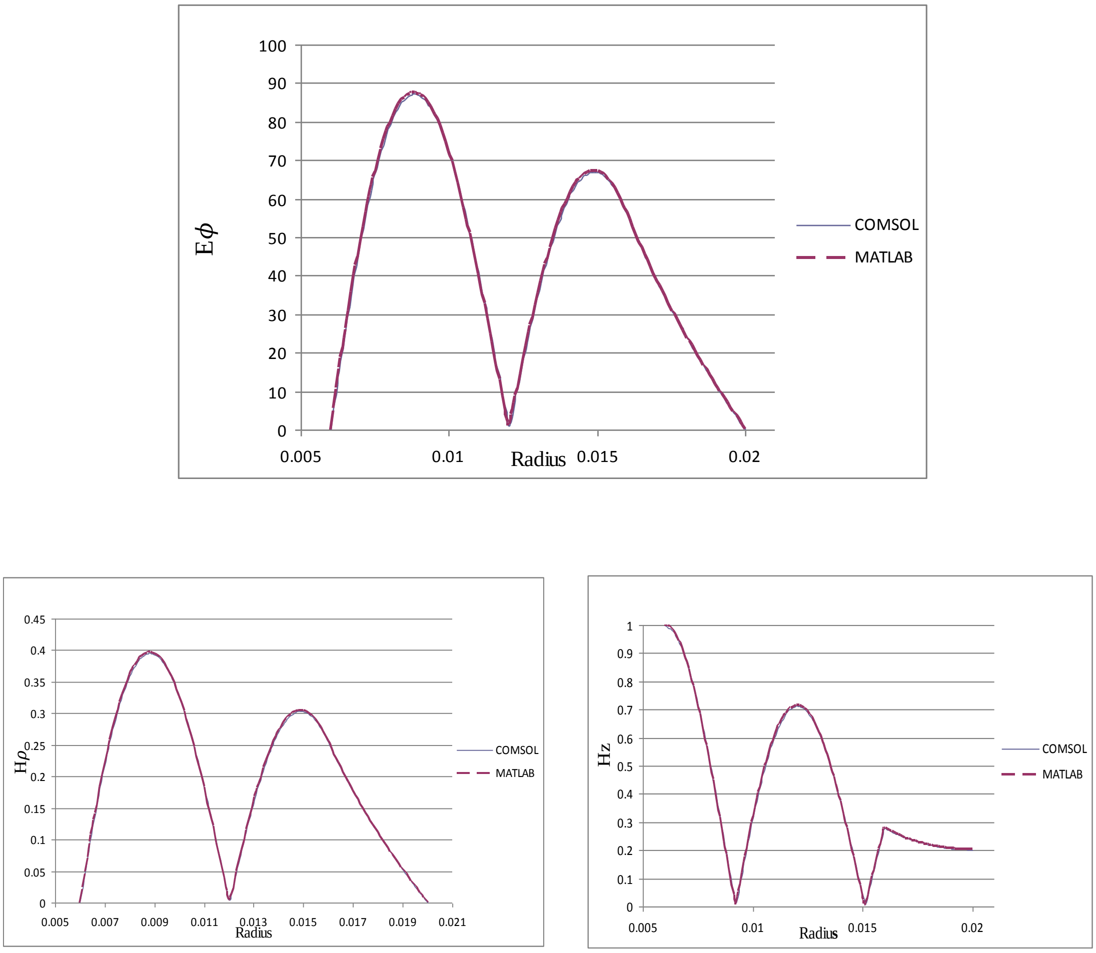

Fig.3.12. Field distributions of TE_{02}.

- *Coupling matrices formulation*

Here we give the coupling matrices for mode-matching analysis in cylindrical coordinates, with first guide being the empty coaxial line.

TM/TM coupling

$$\overline{\overline{HE}}_{mp}^{(12)} = 2\pi \int \vec{e}_{\rho m}^{(2)} \vec{h}_{\varphi p}^{(1)*} \rho d\rho$$

$$\overline{\overline{EH}}_{nq}^{(12)} = 2\pi \int \vec{e}_{\rho n}^{(1)} \vec{h}_{\varphi q}^{(2)*} \rho d\rho$$

TE/TE coupling

$$\overline{\overline{HE}}^{(12)}_{mp} = 2\pi\int \vec{e}^{(2)}_{\varphi m}\vec{h}^{(1)*}_{\rho p}\,\rho d\rho$$

$$\overline{\overline{EH}}^{(12)}_{nq} = 2\pi\int \vec{e}^{(1)}_{\varphi n}\vec{h}^{(2)*}_{\rho q}\,\rho d\rho$$

The coupling between modes of different nature will be zero for azimuthally symmetry case. As the cross section is the same for two structures, the self-coupling terms give two diagonal matrices as following

$$\overline{\overline{EH}}^{(11)}_{np} = \iint \bar{u}_z \cdot \left(\vec{e}^{(1)}_{tn} \times \vec{h}^{(1)*}_{tp}\right) ds = N^{(1)}_{p}\delta_{np}$$

$$\overline{\overline{EH}}^{(22)}_{mq} = \iint \bar{u}_z \cdot \left(\vec{e}^{(2)}_{tm} \times \vec{h}^{(2)*}_{tq}\right) ds = N^{(2)}_{q}\delta_{mq}$$

$$\overline{\overline{N}}^{(1)}_{p} = \iint \bar{u}_z \cdot \left(\vec{e}^{(1)}_{tn} \times \vec{h}^{(1)*}_{tp}\right) ds$$

$$\overline{\overline{N}}^{(2)}_{q} = \iint \bar{u}_z \cdot \left(\vec{e}^{(2)}_{tm} \times \vec{h}^{(2)*}_{tq}\right) ds$$

For multimodal variational method we choose the electric field of eigenmode in partially filled coaxial structure as trial function, so

$$Q_{pq} = -j\left\{ \sum_{n=L+1}^{\infty} \left\langle e_{tp}{}^{(2)} j^{(1)}_{tn} \right\rangle \left\langle j_{tn}{}^{(1)} e^{(2)}_{tq} \right\rangle + N^{(2)}_{p}\delta_{pq>K} \right\}$$

$$U^{(1)}_{pn} = \left\langle e_{tp}{}^{(2)} \middle| \mathbf{j}^{(1)}_{tn} \right\rangle, \quad n = 1,\ 2,..,\ L\ ;$$

$$U^{(2)}_{pm} = N^{(2)}_{m}\delta_{pm}, \quad m = 1,\ 2,...,\ K\,;$$

III.3.1.2 Single discontinuity analysis

In this part we consider two situations, in the first an empty coaxial line is connected to a two layers coaxial structure (with *s* = 0 in Fig.3.13); the second corresponds to a three layers case. All used data are given here:

a = 6mm, inner conductor radius

b = 20mm, outer conductor radius

d = 10mm, thickness of ceramic layer, with estimated relative permittivity of 16.

For two layers case, *s* = 0; for three layers case, *s* = 2mm corresponding to air- or Teflon- layer thickness.

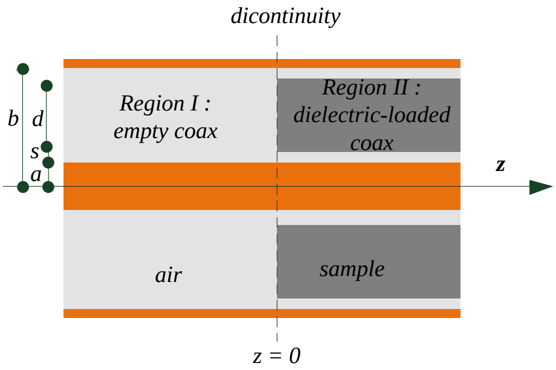

Fig.3.13. Single discontinuity (longitudinal) between empty and dielectric-loaded (two-layered) enlarged coaxial line.

Only mode matching method analysis results are shown in the single discontinuity case, and compared to commercial HFSS software results. For two layers case as for three layers case we can observe from the following figures (Fig.3.14) that the use of only dominate mode (the TEM like) leads to less accurate results. The reason is that the reactive energy in the vicinity of discontinuity plane is not taken into account, as only propagating modes are considered.

To improve the results and take into account the higher order modes, simulation has been taken for three-layer case with number of modes great to one. We observe that the convergence will be obtained with 10 modes in each part. The following figures (air-layered in Fig.3.15; Teflon-layered in Fig.3.16) show the comparisons between HFSS simulation (solid line) and converged results of mode matching simulation.

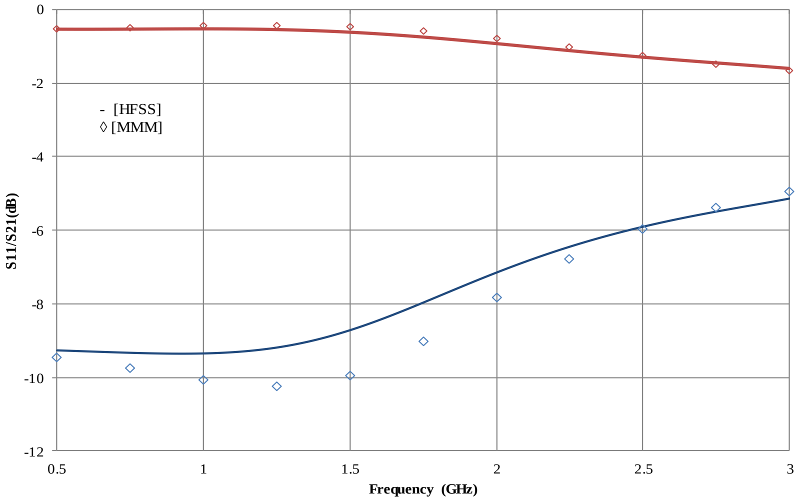

Fig.3.14. Comparison S11/S21 (dB) from Mode-Matching method ('◊') and HFSS simulation for two layers case.

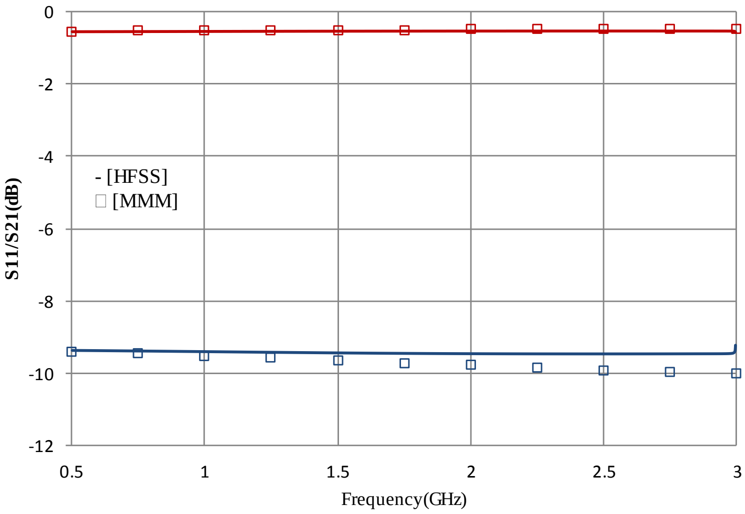

Fig.3.15. Comparison S11/S21 (dB) from mode matching ('□') and HFSS simulation for three layers case (air-layered structure).

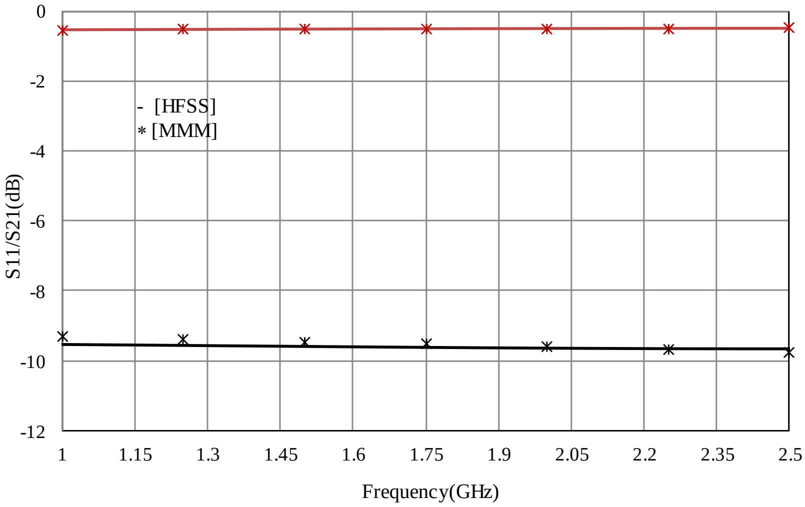

Fig.3.16. Comparison S11/S21 (dB) from our method ('*') and HFSS simulation of Single discontinuity of enlarged coaxial line (Teflon-layered structure).

III.3.1.3 Double discontinuity analysis

Now we will study the double discontinuity consisting of an enlarged coaxial cell partially filled the multi-dielectric layers in the centre part. In our study, a ceramic material is the object of dielectric measurement. To reduce the gap effect well known in hard material measurement a Teflon layer will fill the space between the centre conductor and the ceramic ring. In this part, the electric field is the most important. Then the control of this space by using known loss permittivity material will reduce significantly the extraction error.

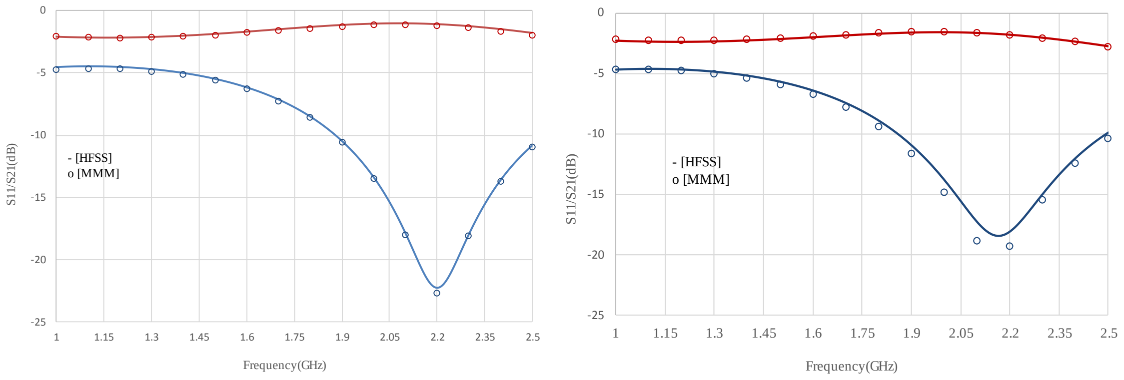

Fig.3.17. Double discontinuity between empty and dielectric-loaded (three-layered) coaxial line geometry. For Teflon layer $\varepsilon_r = 2.1(1-0.001i)$. At the left $tan\delta=0.2$; at the right $tan\delta=0.3$.

To validate our direct analysis, we use an estimate relative permittivity of 16, and several loss tangent values will be used. The ring height is chosen to be 60mm that is the real sample height in the experimental part which will be described in chapter 4. In the Fig.3.17 we observe that the agreements are good for a trial loss tangent of 0.2, while there is a small difference near the minimum transmission for loss tangent of 0.3. The mode matching method (MMM) has been used for these comparisons.

For the need of convergence study the double discontinuity formulation of MVM is applied to a lossless case by varying the number of modes in the partially filled section. The results obtained with HFSS for transmission coefficient in the following figure Fig.3.18 show a resonant effect near 1.7GHz. The MVM analysis has been taken on a limited frequency samples. But we can see the grand influence of number of modes in the centre part of the overall structure.

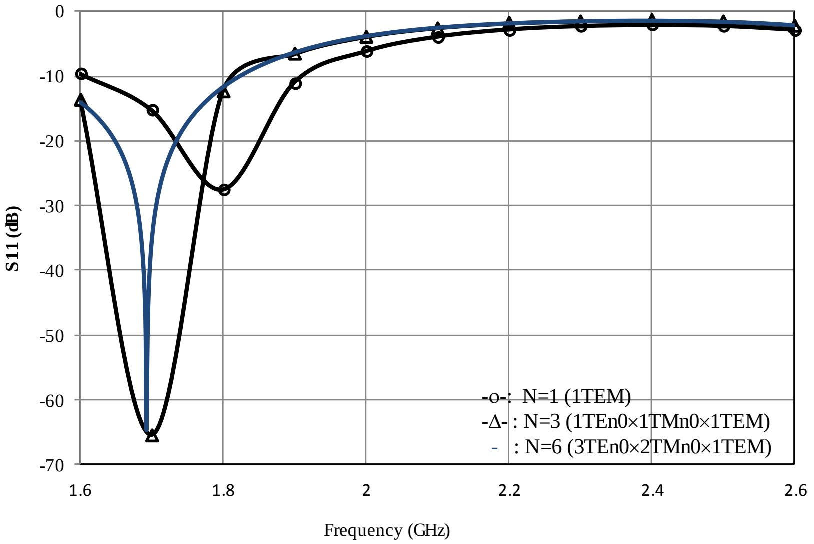

Fig.3.18. Comparison S11 (dB) versus the field expansion number N from our method of double discontinuity of enlarged coaxial line filled with sample without loss.

By using 6 modes in the central part, we can observe good agreement between results obtained by MVM and those from HFSS for both reflection and transmission coefficient in Fig.3.19.

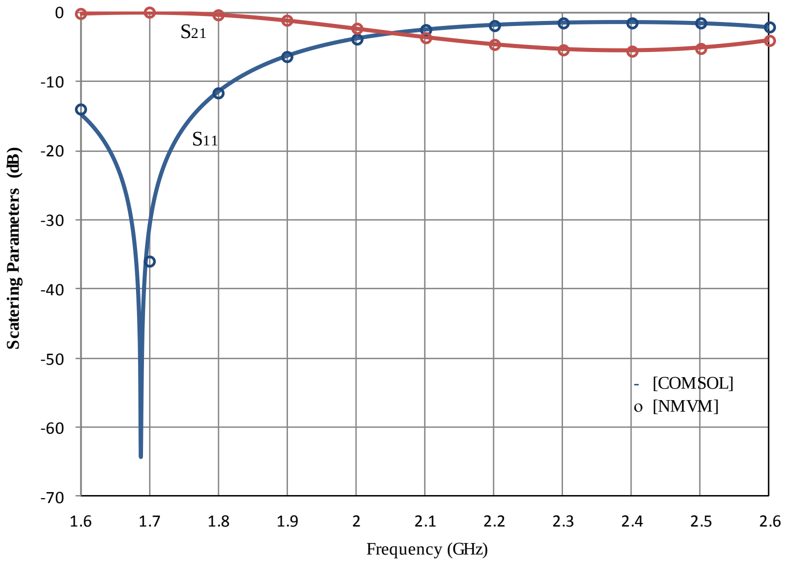

Fig.3.19. Comparison S11/S21 (dB) from our method ('o') (N = 6) and COMSOL simulation of double discontinuity of enlarged coaxial line filled with sample without loss.

The lossy ceramic cases have been now studied by MVM and by COMSOL which is another FEM based software. We can see that good agreements have been obtained for both 0.2 (on the left) and 0.3 (on the right) loss tangent cases.

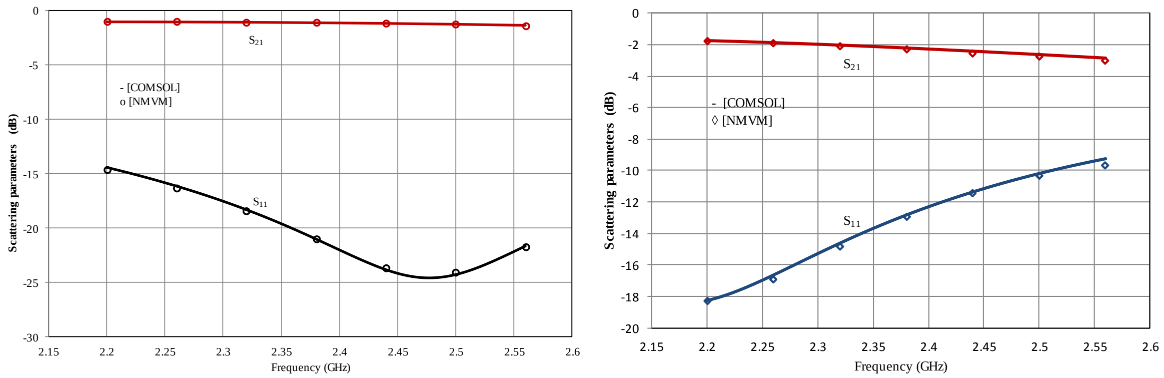

Fig.3.20. Comparison S11/S21 (dB) from our method ('o') and COMSOL simulation of double discontinuity of enlarged coaxial line. The left with sample of loss tangent (tanδ) 0.2 sandwiched both by air; and the right with sample of loss tangent (tanδ) 0.3 sandwiched by Teflon and air.

We can conclude that the application of both mode matching method and multimodal variational method to coaxial type discontinuity give reasonably accurate results, and its use in the inverse modelling of coaxial dielectric measurement cell will be presented in the next chapter.

III.3.2 Discontinuity analysis of multilayered microstrip discontinuity

Multilayer planar structure used in dielectric measurement setup is given in the Fig.3.21, with the right side the microstrip loaded by thin layer unknown dielectric sample. In this part will do the direct analysis to obtain the scattering matrix for inverse modelling in the next chapter.

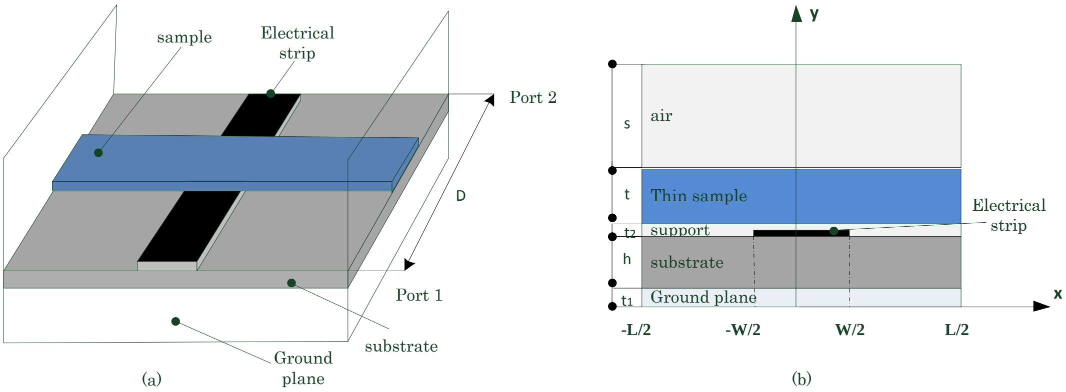

Fig.3.21. Discontinuity involving multilayered microstrip (a) three-dimension view. (b) cross section view.

<u>III.3.2.1 Coupling matrices</u>

As for the coaxial type discontinuities, the determination of coupling matrices is also essential for carrying scattering matrix calculation for both single or double discontinuities involving multi-layered planar structures

<u>III.3.2.2 Numerical results</u>

We will consider only double discontinuity case in this chapter. The use of single discontinuity analysis in modified Nicholson-Ross-Weir algorithm will be discussed in the next chapter.

- *<u>Plexiglas filled multilayer structures</u>*

The Plexiglas slab is of 10mm thickness and 22.9mm length. We take 3.2 as relative permittivity. We use the reduced symmetric T network to represent the double discontinuity at the two discontinuities planes. Our analysis has been carried with respectively 2 and 7 modes in the Plexiglas filled centre part, with results shown in Fig.3.22 for imaginary part of series impedance and Fig.3.23 for imaginary part of shunt impedance.

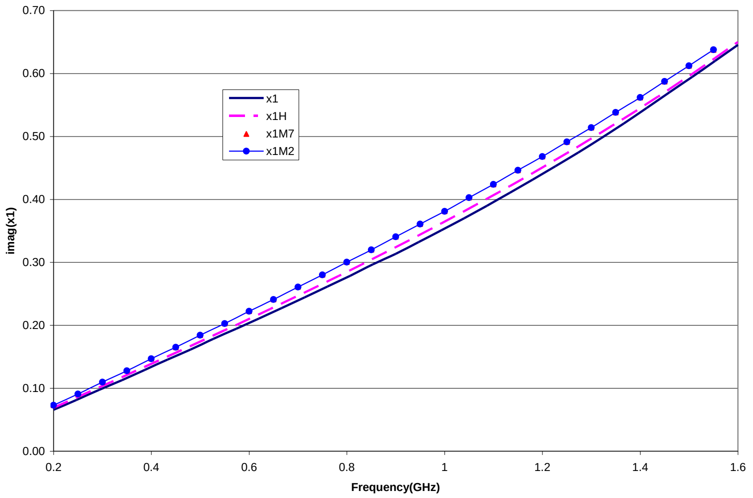

Fig.3.22. Comparison on imag(z_1) from our method ('o' for 2 modes and triangle for 7) and those from HFSS (strait line with max(ΔS)=0.05, dotted one with max(ΔS)=0.001).

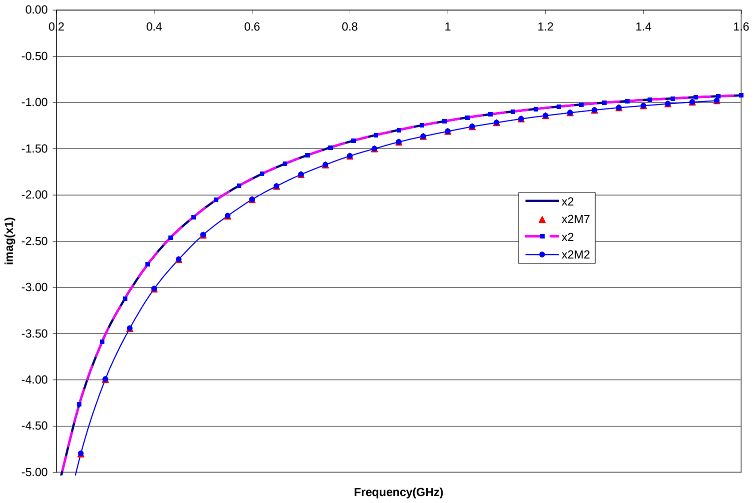

Fig.3.23. Comparison on imag(z_2) from our method ('o' for 2 modes and triangle for 7) and those from HFSS (strait line with max(ΔS)=0.05, dotted one with max(ΔS)=0.001).

The same simulation has been taken with commercial software HFSS, with two different convergence criteria. The results are also reported in Fig.3.22 and Fig.3.23. We can see in Fig.3.22 the same variation tendency for all case in the imaginary part of z_1. We observe also an appreciable difference between 2 HFSS results, one with Maximum Delta S of 0.05, and another with 0.001.

The difference on imaginary part of z_2 is more noticeable but we have always the same variation tendency. The possible explanation of these difference will be the difference in wave port impedance definition which can influence the final simulation results.

- *Alumina filled multilayer structures*

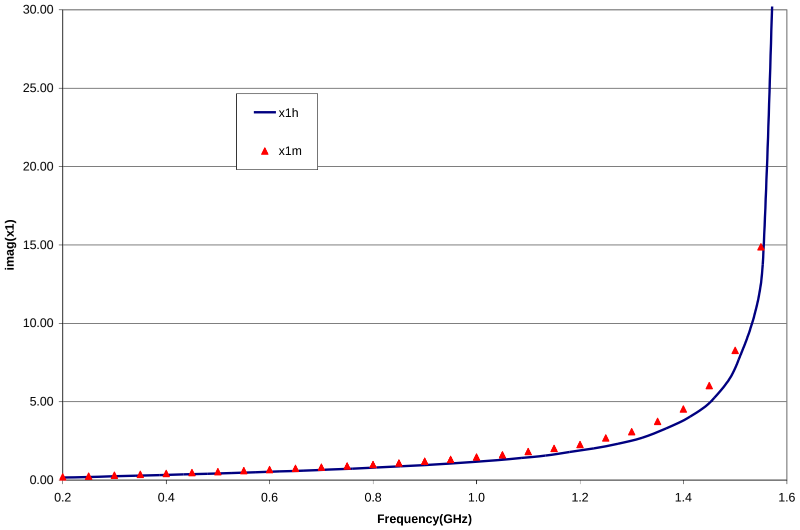

Fig.3.24. Comparison on imag(z_1) from our method (triangle mark) and those from HFSS ($\max(\Delta S)=0.002$).

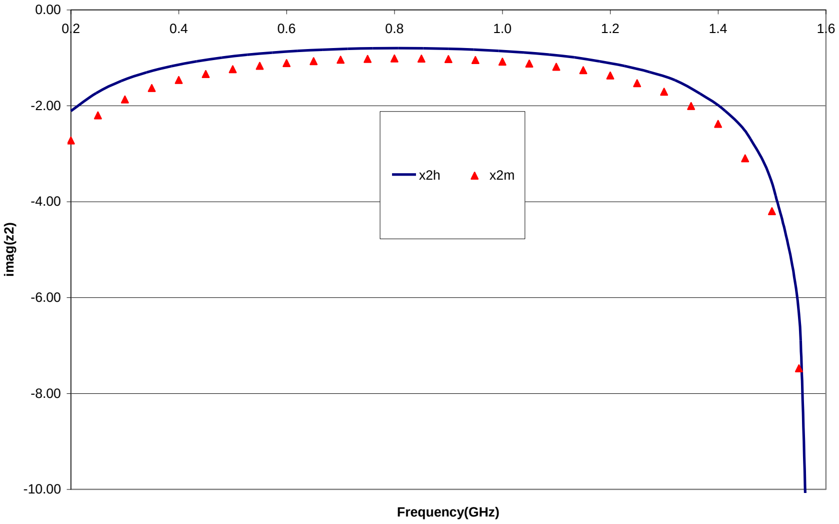

Fig.3.25. Comparison on imag(z_2) from our method (triangle mark) and those from HFSS ($\max(\Delta S)=0.002$).

Now for an alumina slab of 2mm thickness and 50.8mm length, the discontinuity effect will be more important with higher relative permittivity. We choose 9.5 as the trial relative permittivity. Again we compare our results with those obtained from HFSS with maximum delta S of 0.002. The comparison on imaginary part of series impedance is given in Fig.3.24 while that for imaginary part of shunt impedance in Fig.3.25.

Once again more difference has been observed on the shunt impedance value. The probable reason is the manner to define the excitation source at HFSS wave port. Additional efforts are needed to clarify this situation.

III.4 CONCLUSION

In this chapter we have given a description of three eigenmode based waveguide discontinuity analysis method. Both mode matching method and multimode variational method have been applied to discontinuities involved in coaxial dielectric measurement cell. Both lead to comparable results to finite element method based commercial software like HFSS or COMSOL.

In the case of multilayer planar structure discontinuities, the symmetric double discontinuity has been modeled by its equivalent reduced T network, and the corresponding frequency variation of network elements has been obtained by both MVM analysis and HFSS simulation. Agreement has been observed in the tendency of both series and shunt impedance, but the difference on the shunt impedance value are more important. Even with different convergence study the difference remain important. More efforts are needed to clarify this situation.

References of chapter III

[III-1]. Marcuvitz, Nathan. *Waveguide handbook*. No. 21. Iet, 1951.

[III-2]. Itoh, Tatsuo. "Recent advances in numerical methods for microwave and millimeter-wave passive structures." *IEEE transactions on magnetics* 25.4 (1989): 2931-2934.

[III-3]. A. Wexler, "*Solution of waveguide discontinuities by modal analysis*," *IEEE Trans on Microwave Theory and Tech*, vol.15, no.9, pp: 508-517, 1967.

[III-4]. S. Lee, and R. Mittra. "*Radiation from dielectric-loaded arrays of parallel-plate waveguides*," *IEEE Trans on Antennas and Propagation*, vol. 16, no.5 pp: 513-519,1968.

[III-5]. R. Mittra, Y. Hou, and V. Jamnejad. "*Analysis of open dielectric waveguides using mode-matching technique and variational methods*," *IEEE Trans on Microwave Theory and Tech*., vol. 28, no.1, pp: 36-43, 1980.

[III-6]. T. S. Chu, T. Itoh, and Y. Shih. "*Comparative study of mode-matching formulations for microstrip discontinuity problems*," *IEEE trans on microwave theory and tech*, vol. 33, no.10, pp: 1018-1023, 1985.

[III-7]. R. Sorrentino, et al. "*Full-wave modeling of via hole grounds in microstrip by three-dimensional mode matching technique*." *IEEE trans on Microwave Theory and Tech.* vol. 40, no.12, pp: 2228-2234,1992.

[III-8]. N. Aknin, A. EI Moussaoui, and M. Essaaidi. "*Analyse des résonateurs diélectriques anisotropes uniaxiaux par la méthode du raccordement modal*." *Annals of Telecommunications*, vol. 53, no.7, pp: 311-315, 1998.

[III-9]. R. Mittra and W. W. Lee, *Analytical techniques in the theory of guide waves*, Macmillan, New York, 1971.

[III-10]. R. E. Collin, *Field Theory of Guided Waves*, McGraw-Hill, New York, 1960 (aussi 2ème édition en 1991).

[III-11]. J. W. Tao, *Contribution à la Caractérisation des Discontinuités en Microondes et Application à la Synthèse des Filtres*, Thèse de doctorat INP de Toulouse, Déc. 1988

[III-12]. P. Couffignal, *Contribution à l'Etude de Filtres en Guides d'Ondes Métalliques,* Thèse de doctorat INP de Toulouse, Nov. 1992

[III-13]. J. W. Tao, H. Baudrand & P. Espes, "Variational analysis and synthesis of stepped ridged waveguide transformer," *Microwave & Optical Tech. Lett.*, vol.2, pp.103-110, March 1989

[III-14]. J. W. Tao, H. Baudrand, B. Théron & J. C. Nanan, "Conception de filtre passe-bande en guide nervuré par l'approche variationnelle," *6es JNM*, Juin 1989, pp.316-317

[III-15]. J. W. Tao, H. Baudrand, "New design procedure for evanescent-mode ridged waveguide filters," 1989 *URSI EM Theory Symposium, Stockholm*, Aug.1989, pp.458-460

[III-16]. J. W. Tao, H. Baudrand, "Multimodal variational analysis of uniaxial waveguide discontinuities," *IEEE Trans.on MTT*, Vol.39, pp.506-516, March 1991

[III-17]. J. W. Tao, P. Couffignal, J. C. Nanan, H. Baudrand & B. Théron, "Method for characterization of waveguide discontinuities; applications to filter optimization," *Mikrowellen und Optronik 90*, Stuttgart, Apr. 1990,pp.333-338

[III-18]. J. W. Tao, H. Baudrand, B. Théron & J. C. Nanan, "Analyse et conception de filtre passe-bande en guide nervuré par l'approche variationelle," *Annales des Télécommunications*, Tome 45, N°5-6, pp.344-350, May/Juin 1990

[III-19]. P. Couffignal, J. C. Nanan, J. W. Tao, H. Baudrand & B. Théron, "A multimodal variational approach for the characterization of waveguide discontinuities for microwave filter design," 20th *European Microwave Conference*, Budapest, Sept. 1990, pp.919-924

[III-20]. J. C. Nanan, J. W. Tao, H. Baudrand, B. Théron & S. Vigneron, "A two-step synthesis of broadband ridged waveguide bandpass filters with improved performances," *IEEE Trans. on MTT*, Vol.39, pp.2192-2197, Dec. 1991

[III-21]. J. W. Tao , G. Angénieux, B. Flechet & H. Baudrand, "Multimodal variational analysis of quasiplanar waveguide discontinuities," *23th European Microwave Conference*, Madrid, Sept. 1993, pp.662-664

CHAPTER IV APPLICATION TO DIELECTRIC MEASUREMENT CELL

IV.1 INTRODUCTION

This chapter discusses the application of coaxial cell and planar transmission line in the measurement of the electromagnetic properties of materials, including ring form samples inserted in the enlarged coaxial cell, and thin films or block samples upon the microstrip line. The calculation of materials properties from S-parameters measurement mainly includes two steps: direct problems and inverse problem. The direct problem computes the S-parameters of measurement cell under test propagating only quasi-TEM mode, according to the cell dimensions and the frequency. From a given complex permittivity ε_r and permeability μ_r values, a given frequency range, and knowing the cell structure parameters, we can calculate the complex propagation constant, and its corresponding field distributions, then the effective permittivity and permeability. After that, the S parameters can be deduced numerically from the discontinuity analysis, which is discussed in Chapter II and III for coaxial cell and multi-planar structure. The inverse problem is based on an iterative technique to carry out the ε_r and μ_r computation and the convergence between measured values (of input impedance in coaxial cell or effective constants in microstrip line) and those values from numerical analysis.

After an introduction on the procedures of materials property characterization, we discuss their numerical results of these applications on coaxial cell and microstrip line. Compared to the resonant methods for material property characterizations, in our research, non-resonant method based on coaxial cell and microstrip line is introduced to characterize, respectively, the complex permittivity for high-loss dielectric materials and the complex permittivity and permeability for low-conductive artificial composite powder block samples.

In the non-resonant method mentioned in the literature [IV-1], the properties of materials are deduced from their impedance and wave velocities in a propagating structure filled with a given materials. When an electromagnetic wave propagates from one structure to another, both the characteristic wave impedance and the wave velocity will change, resulting in a partial reflection of electromagnetic wave from the interface between two propagating structures. Measurement of the reflection from interface and the transmission through the interface can provide information for the deduction of permittivity and permeability [IV-2]-[IV-4]. Non-resonant methods mainly include reflection methods and transmission/reflection methods [IV-5].

✓ *Reflection method*

Reflection method is the technique that the properties of a sample are obtained from the reflection due to the impedance discontinuity caused by the presence of the sample in a transmission structure. Among several types of transmission lines, due to its wide working frequency range, coaxial line is widely used in the reflection method for material property characterization. In our study, the ring sample is inserted into a certain position of the enlarged multi-layered coaxial cell Fig.1, which affects the characteristic impedance. The properties of sample are derived from the short-circuit reflection due to the impedance discontinuity. The measurement fixture of enlarged coaxial cell is designed to satisfy special measurement requirement to increase the accuracy and sensitivity.

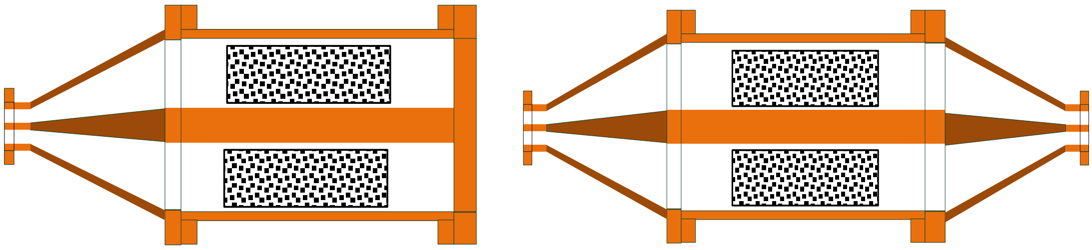

(a)

(b)

Fig.1. Coaxial measurement cells. (a) Reflection cell; (b) Reflection/transmission cell.

✓ *Transmission/reflection method*

Transmission/reflection method is the technique that the sample under test (SUT) is inserted into a segment of transmission line, and the permittivity and permeability of the sample are derived from the reflection and transmission of the sample-loaded unit. Planar circuit transmission/reflection method is based on the Nicolson-Ross-Weir method algorithm which is elaborated for microstrip line structure Fig.2. The characteristic impedance and propagation constant are functions of dielectric and magnetic properties of substrate and materials. If there is the SUT inserted into a segment of transmission line, characteristic impedance and propagation constants of the transmission line will be changed. Because of reflectance at discontinuity plane, electromagnetic properties of SUT can be derived.

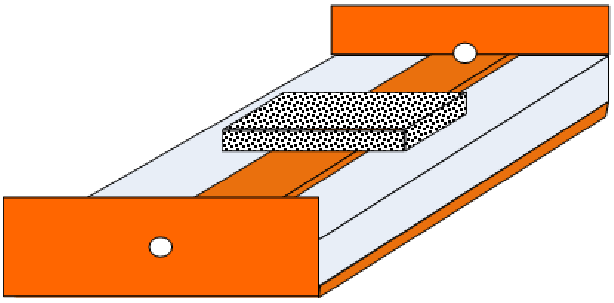

Fig.2. Microstrip measurement cell.

IV.2 DIRECT PROBLEM

IV.2.1 Direct analysis of coaxial measurement cells

When choosing finite element method based electromagnetic analysis tools, the entire measurement cell will be modeled first in the software framework before the definition of physical problem and the choose of all parameters related to the use of FEM analysis. With the eigenmode based electromagnetic analysis the entire structure will be decomposed in separate elements, and each one can be described by its equivalent ***multiport network*** with the "accessible modes" number adjusted according to the circumstance as described in last chapter in multimode variational analysis. For the coaxial dielectric measurement cells, we propose the decomposition for our two measurement cells as following (Fig.3):

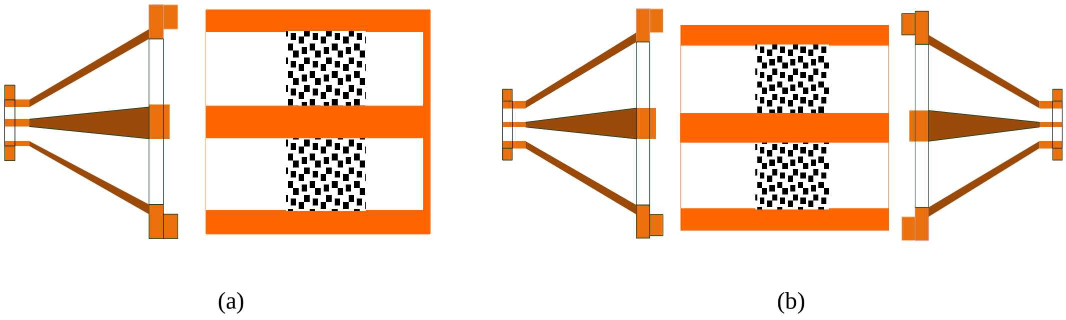
(a) (b)

Fig.3. (a) Reflected cell. (b)Reflection/transmission cell.

The central part will be studied by eigenmode based analysis methods as described in the chapter 3. The input (and the output for reflection/transmission cell) corresponds to a transition section between the standard male N connector and the enlarged coaxial line. If the unknown sample is placed sufficiently far from the input side, we can model the transition as a two port. Once the equivalent elements of this two-port circuit are obtained, the overall scattering matrix of the measurement cell can be easily deduced by cascading the scattering matrices of all part.

We will first focus on the modeling of the transition section in the following.

- ***<u>Transition section modeling</u>***

We suppose that the higher order modes in the central section are all evanescent and the distance between the input plane and the empty/loaded guide interface is sufficient so the higher mode part can be neglected compared to reflection of coaxial TEM mode. In this case an equivalent two port is suggested with its T-equivalent circuit shown in Fig.4.4 (b) for the conical transition shown in Fig.4.4 (a).

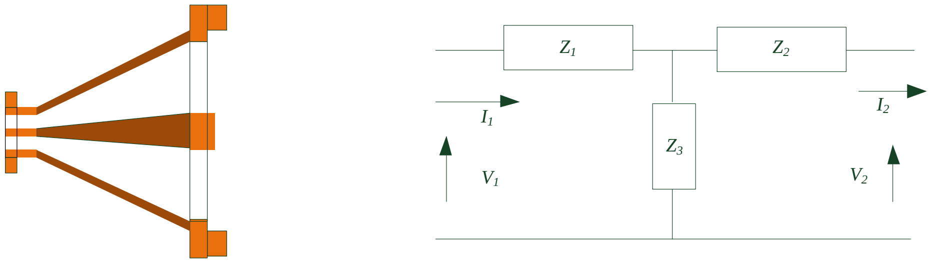

(a)

(b)

Fig.4.4. (a) Conical transition. (b) T-equivalent circuit of conical transition.

According to our previous work [[IV-6], [IV-7]] the equivalent *T*-form network can be determined by using reflection calculation with three particular known terminations to deduce the three unknown equivalent elements (Z_1, Z_2 and Z_3). This is a kind of calibration for asymmetric two ports. By either full wave electromagnetic modeling or experimental vector network analyzer measurement, we can get three input impedances noted Z_{sc}, Z_{oc} and Z_{load} corresponding respectively to three terminations at the enlarged coaxial line side, short, opens and load. By identification the two port elements are as the following:

$$Z_1 = Z_{oc} - Z_3 \text{, } \quad Z_2 = K - Z_3 \quad \text{and} \quad Z_3 = \sqrt{(Z_{oc} - Z_{load})(K + Z_L)} \tag{4.1}$$

Where $K = Z_L(Z_{oc} - Z_{load})/(Z_{load} + Z_{sc})$.

As explained in [IV-6], [IV-7] the accurate electromagnetic modeling of the transition section is very difficult because of the inaccuracies in the mechanic data. So the experiments are preferred in this work. As calibration standards for enlarged coaxial lines are not commercial available, our previous work is used here. For a chosen frequency range from 2.2 to 3GHz, the calibration kit (short, open, and load) is used to take reflection measurement at input N connector plane.

The calibration procedure consists in the measurement of three given situation with transition terminated respectively by charge of 'short', 'open' and 'load' types, and the deduction of the equivalent complex impedances of frequency-dependent variation. Note that standard 'short' should provide good electrical contact to both inner and outer conductors; and a small gap may result in large errors.

Contrary to [IV-6], [IV-7] in which the load type termination is realized by lump resistor usable only in very low frequency, we take a shorted enlarged coaxial line with its length controlled by a sliding short plate. Here we show the modulus and arguments of reflection coefficient for three measurements in Fig.4.5.

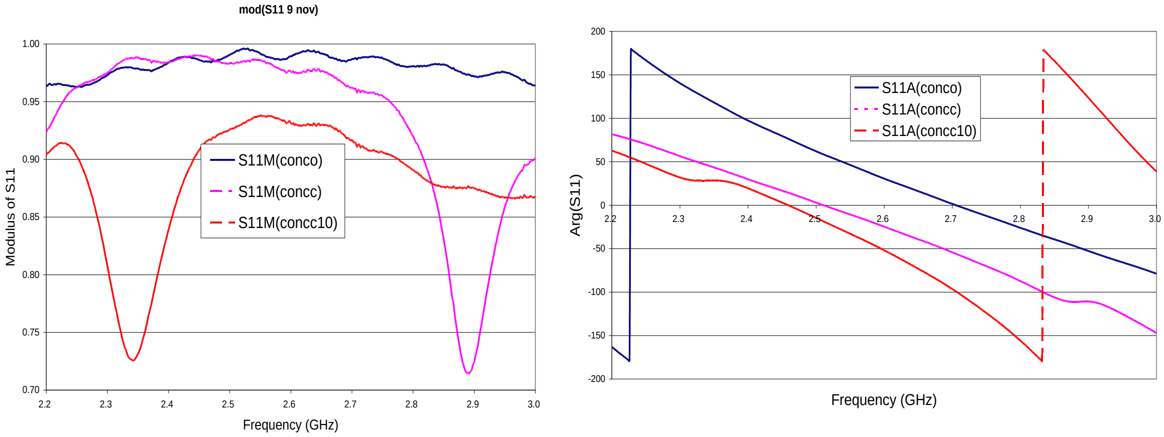

(a) (b)

Fig.4.5. Modulus (a) and argument (b) of reflection coefficients for transition terminated with three "known" charges: OPEN, SHORT and SHORT with 10mm extra length.

From these measurements, the frequency variation law for three equivalent complex impedances is calculated and shown in Fig.4.6. These frequency-dependent impedances within the chosen frequency range show their real parts much less than the imaginary parts in the first three figures. By using now an inverse formulation to deduce the terminal impedance from the VNA measured input impedance, the arguments variation shown in Fig.4.6 (d) confirmed that the phases of short and open circuit are π and 0 and the phase of load circuit varied linearly as a function of frequency.

Another validation has been taken with two transitions and an enlarged empty coaxial line of 120mm length. The following figure compares the measured reflection coefficient and the calculated one with the transitions modeled by data given in Fig.4.7. We can observe a reasonably good agreement between these two curves.

Nevertheless, the determination of accurate discontinuity plane is difficult for our home-made measurement cell. Indeed, the inner conductor is not fixed with precision and its longitudinal position may change in several millimeters. To obtain matched first resonance position the central length is adjusted to 112mm instead of 120mm. This can cause measurement uncertainty in our future permittivity extraction, and should be considered in error analysis.

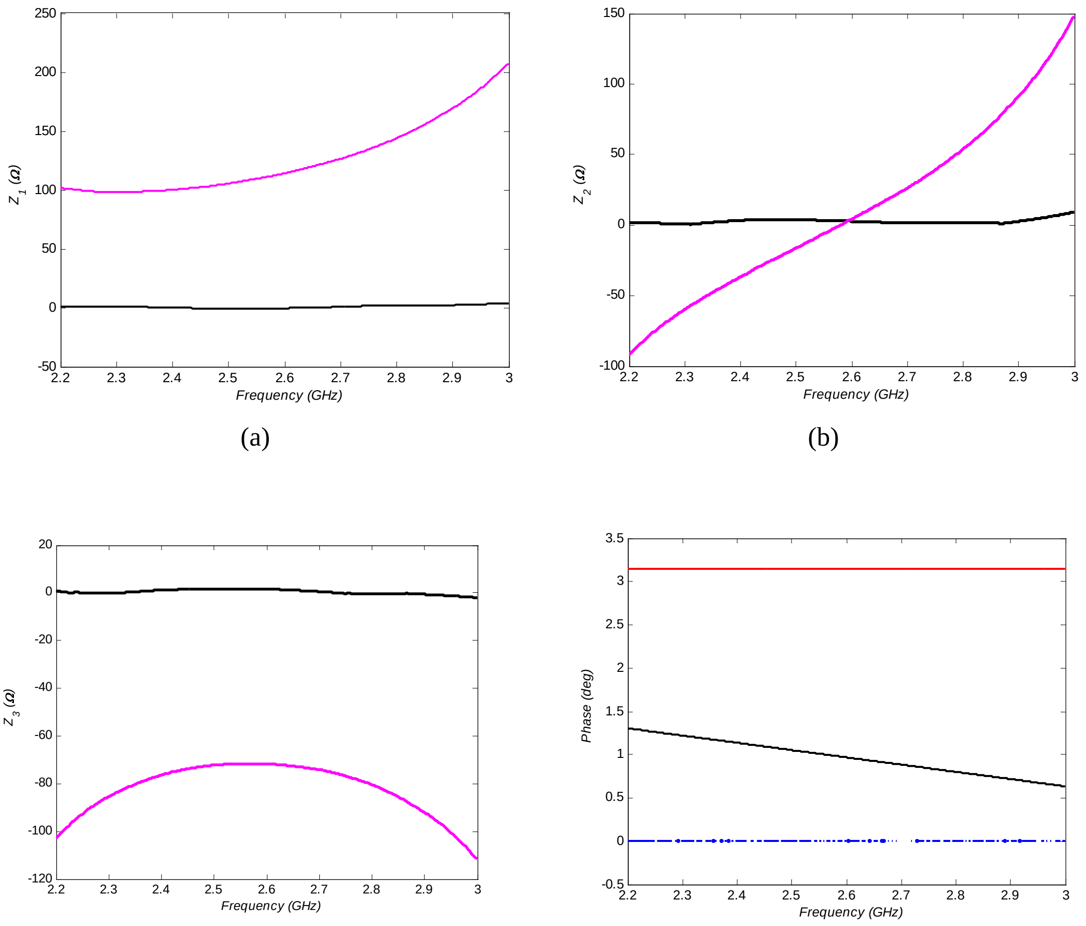

(a)

(b)

(c)

(d)

Fig.4.6. Variation law of three equivalent complex impedances. (a) Real/imag parts of Z_1 (b) Real/ imaginary parts of Z_2 (c) Real imaginary parts of Z_3 (d) Phase validation of three inverse modeled complex impedances.

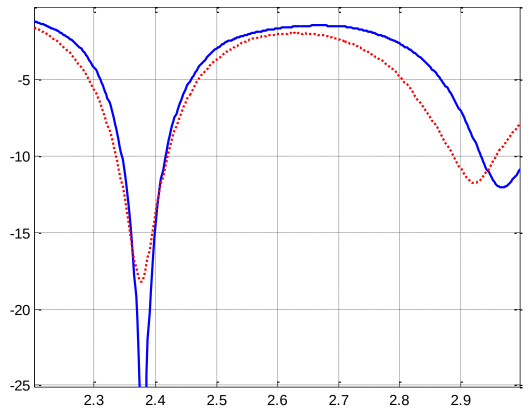

Fig.4.7. Measured (in blue) and simulated (in red) return loss of experimental setup with two transitions and 120mm length enlarged coaxial line.

IV.2.2 Direct analysis of multi-layered planar structure

We will work on a planar transmission line based dielectric measurement cell. Among diverse types of planar transmission circuits, microstrip is the most widely used in the characterization of the electromagnetic properties of materials, especially thin films. A microstrip based dielectric measurement setup has been realized in our research team at LAPLACE. Several dielectric property extraction methods will be considered, and for each method a different direct analysis will be presented in the following.

- ***Description of measurement cell***

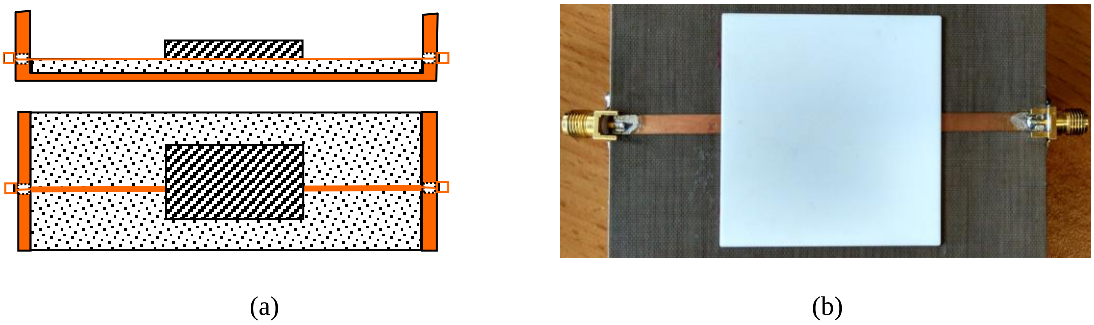
(a) (b)

Fig.4.8. Microstrip measurement setup. (a) Schematic and (b) real structure with alumina plate.

Part of microstrip dielectric measurement setup is shown in Fig.4.8, with its photo at the right side, and the front and top views at the left side. Input and output are connected to VNA via female SMA connector of 50Ω impedance. So the empty microstrip line has been designed to have 50Ω characteristic impedance. The substrate (AD255C) is chosen for its low dielectric constant, low cost and excellent low-loss. The relative permittivity at working frequency range is 2.55, with loss tangent of 0.0011 at 1MHz and 0.0014 for 10GHz. The stability over wide frequency and temperature ranges makes it ideal for variety microwave and RF applications in telecom infrastructure. All geometry data are given in Table.4.1, except the total microstrip line length which is 101.5mm from one SMA connector to another.

Table.4.1 Structure parameters of microstrip line.

Properties	Dimensions
width (w)	4.257mm
height (h)	1.524mm
thickness of ground conductor (t_1)	35μm
thickness of strip conductor (t_2)	35μm

- ***TRL calibration***

Even with equal characteristics impedance the transition between SMA connector and microstrip line introduce reflection and insertion loss. The well-known TRL calibration will be taken to eliminate effect of transition. For these two other elements are realized on the same dielectric substrate, a second microstrip line of 46mm length, and a third line terminated by an open circuit. According to the suggestion formulated by VNA manufacturer the corresponding measurement frequency range usable will be between 200MHz and 1.6GHz.

- ***3D Direct analysis***

Three-dimensional direct analysis of a microstrip line filled partly by sample under test at its middle position can be carried out by finite element method based commercial software or eigenmode based methods as described in the last chapter. Its use in inverse modeling will be presented in the next section.

- ***2D Direct analysis for NRW algorithm use***

Nicholson-Ross-Weir algorithm is widely used in simultaneously extraction of relative permittivity and relative permeability of unknown material in transmission line based or waveguide based measurement cell. All relations will be given in the next section. Here we need to point out that the use of NRW algorithm depends on the explicit relations between electric property of sample, characteristic impedance and phase velocity of corresponding guiding structure.

Unfortunately explicit relations between the propagation constant, the characteristic impedance of a TEM line and the parameters of the constituent material no longer exist in the cases of planar structures. If for the conventional lines such as simple strip, coplanar line, the approximate explicit formulations exist; for the others, a numerical simulation tool is necessary, especially for the multilayered structures. As discussed in Chapter II, the propagation constants of the multilayered planar structures can be obtained by transverse resonance method based on the given permittivity and permeability of the sample, and in our study frequency range, only the fundamental mode propagates through the test fixture. The product of the effective permittivity and permeability of inserted section of microstrip cell is a square of propagation constants of propagating mode.

A series of design curves will be obtained, in a given frequency range, corresponding respectively to the effective relative permittivity and permeability, and the characteristic impedance, with each curve obtained with a trial value for sample's permittivity and permeability. These curves constituent a data basis from which explicit relation can be obtained *numerically* by using interpolation techniques.

The cell loaded with alumina plate (shown in Fig.4.8) has been designed to operate between 200MHz and 1.6GHz when the relative permittivity of the material does not exceed 15. This central part will then be modeled as a section of multilayer planar transmission line including the sample to be characterized by using the full-wave modified transverse resonance method (MTRM) [IV-8]. The application of MTRM to this structure with trial relative permittivity varying between 7 and 16 leads to the effective relative permittivity of the center section loaded with plate as shown in Fig.4.9.

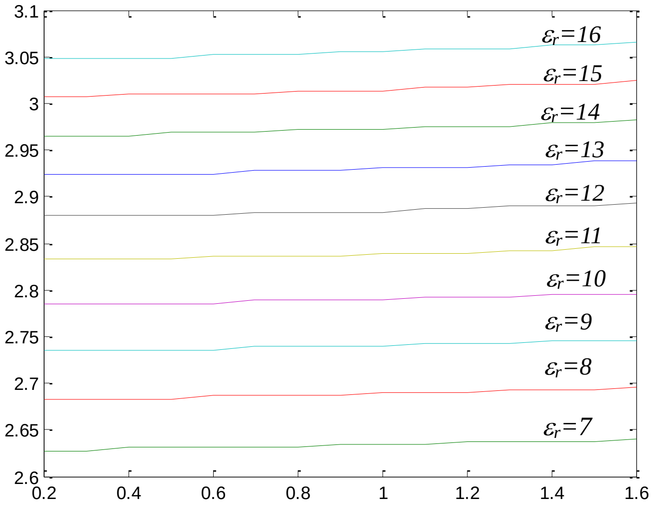

Fig.4.9. Characteristics of multi-layered microstrip line. Estimated effective relative permittivity by MTRM for alumina covered microstrip line

IV.3 INVERSE PROBLEM

The inverse problem is the second step for material property characterization. The complex permittivity and permeability of under-test material are extracted by comparing theoretical and measurement results by choosing those values which may minimizing the error function.

In this section the direct electromagnetic analysis will be taken by using commercial software COMSOL for its facility to interface with MATLAB environment in which the use of MATLAB optimization toolbox is needed.

IV.3.1 Inverse modeling of coaxial measurement cell

We will work with the reflection method in which the sample under test is placed in an enlarged coaxial line in COMSOL Multiphysics with a guest value of relative complex permittivity for a given frequency. Fig.4.10 shows a cutting view in which we see the sample is placed near the center conductor with a Teflon ring who fills the space between them. One end of the coaxial line is short ended, and the input port in the other end is excited with the TEM coaxial mode.

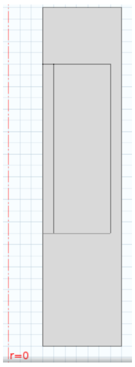

Fig.4.10. COMSOL model of sample loaded enlarged coaxial structure ended by short

For a measurement effectuated with a given configuration, we will first deduce the complex input impedance seeing from the feeding plane of enlarged coaxial line, by make use of the calibration procedure described in IV.2.1. In Fig.4.11, we show the real and imaginary part of measured input impedance at the N connector plane, Z_{meas}, and the deduced impedance at the enlarged coaxial line input, noted $Z_{\text{meas\_new}}$.

The COMSOL simulation with a trial vector x=[real(epsr) imag(epsr)] leads to estimated enlarged coaxial line input $Z_{\text{COMSOL}}(x)$. We can define the following error function

$$error(x) = \left\{ \mathrm{Re}\left(Z_{COMSOL}(x) - Z_{meas\_new} \right) \right\}^2 + \left\{ \mathrm{Im}\left(Z_{COMSOL}(x) - Z_{meas\_new} \right) \right\}^2 \qquad (4.2)$$

The minimization of error function will be taken with *fminsearch* function in MATLAB environment. With appropriate choice of initial value for complex relative permittivity reasonable good convergence can be obtained.

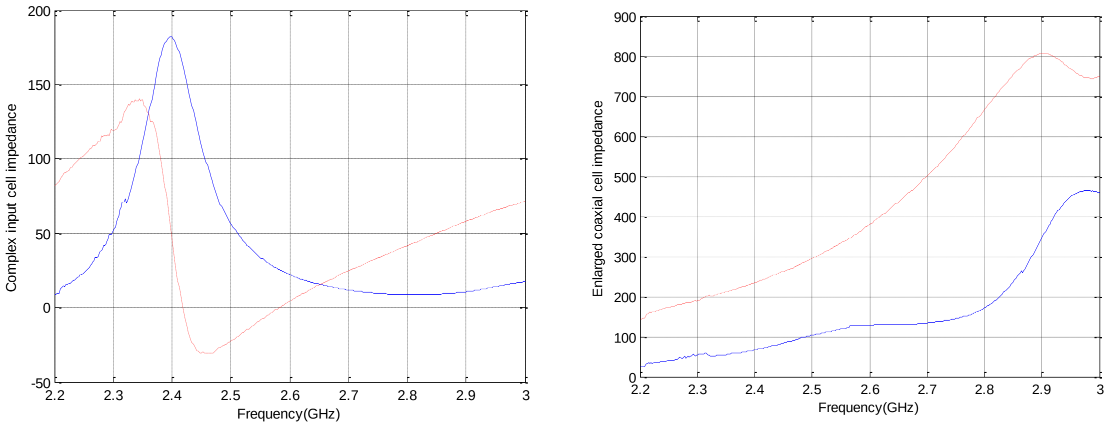

(a) (b)

Fig.4.11. Complex input impedance for (a) real cell; (b) equivalent enlarged cell.

IV.3.2 Inverse modeling of planar measurement cell

In this section, after introduction of the characteristic impedance and velocity change caused by the sample-loaded discontinuity, calculation algorithm will be discussed for the extraction of electric properties of SUT. Calculation algorithm, Nicolson-Ross-Weir algorithm (NRW) [IV-9]-[IV-12], will be applied to the scattering parameters measured with VNA on a microstrip transmission line cell upon which a rectangular slab sample is added. The effective complex permittivity and permeability of central part consisting of the plate on a reference planar line will be deduced.

➢ ***3D Inverse modeling***

For parameters after TRL calibration, and the full wave electromagnetic analysis results using trial permittivity and permeability of unknown material, an optimization is applied to the following error function in which c_1 and c_2 are weighting factors to be adjusted to a given measurement setup.

Error! Objects cannot be created from editing field codes. (4.3)

As the number of full wave analysis can be very important during optimization procedure, the computation time will be very important. It is for this reason the following 2D inverse modeling is introduced, using a modified version of the well-known NRW algorithm.

➢ ***2D Inverse modeling***

We call this work 2D inverse modeling because of the necessary 2D simulation to obtain the propagation characteristics of multilayered planar structure. Before the discussion in the manner to take inverse modeling we will give a short description of the NRW algorithm which will be a part of our inverse modeling tool.

- **Ideal junction between homogeneous TEM Transmission lines**

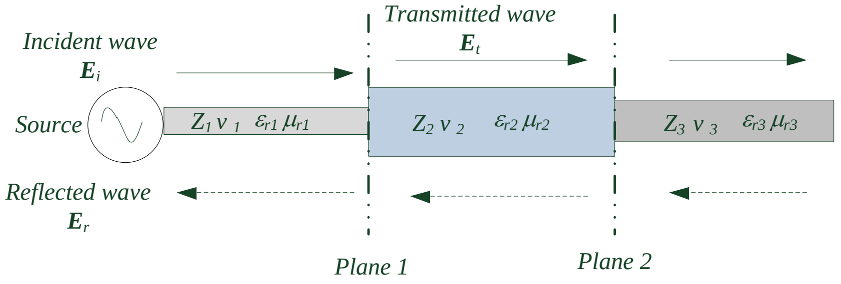

Fig.4.12. Discontinuities in transmission lines. Z_1, Z_2 and Z_3 are wave impedances in region I, II and III. Solid arrows and the dashed line indicate represent incident and reflected waves.

We will consider the situation shown in Fig.4.12 in which each section corresponds to homogeneous TEM transmission line filled with different materials. The characteristic impedance of TEM mode is the same as plane wave impedance in an infinite space of relative permittivity ε_r and relative permittivity μ_r. In free-space, speed of light and wave impedance are $c_0 = 1/\sqrt{\mu_0\varepsilon_0}$ and $\eta_0 = \sqrt{\mu_0/\varepsilon_0}$ respectively. For the homogeneous medium filled in the regions as shown in Fig.4.12, $\upsilon_i = 1/\sqrt{\mu_{ri}\varepsilon_{ri}}$ and $Z_i = \sqrt{\mu_{ri}/\varepsilon_{ri}}Z_0$, where i = 1,2 and 3, are the phase velocities and characteristic impedances of region I, II and III, respectively. At the interface between two sections of TEM transmission line with characteristic impedances Z_1 and Z_2 respectively, the reflection coefficient seeing from transmission Z_1 is given by

$$\Gamma = \frac{Z_2 - Z_1}{Z_2 + Z_1} \tag{4.4}$$

As only TEM modes are considered in this situation the junction between two lines are called "ideal" one.

- **Nicholson-Ross-Weir (NRW) algorithm**

The work of Nicholson, Ross and Weir addresses the fully filled TEM line or rectangular waveguide between know TEM or waveguide of same dimension for the dielectric measurement purpose. A typical configuration for transmission/reflection measurement is shown in Fig.4.13. The sample under test constitutes the filling material in the region II. Incident waves travel through the three sections with different propagation constants γ_1, γ_2 in region I and II, respectively, which are defined as

$$\gamma_i = j\sqrt{\frac{\omega\mu_{ri}\varepsilon_{ri}}{c_0^2} - \left(\frac{2\pi}{\lambda_c}\right)^2} \tag{4.5}$$

where i = 1, 2; ω is the angular frequency, c_0 is the speed of light in free space, λ_c is the cutoff wavelength of each waveguide. For TEM or quasi-TEM mode, $\lambda_c = \infty$.

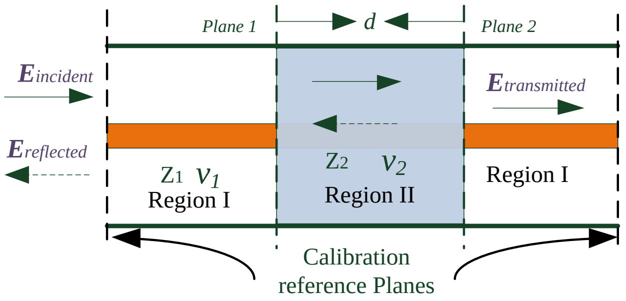

Fig.4.13. Measurement cell with region II fully filled with under-test.

At the interface of impedance discontinuity, the reflection coefficient Γ and propagation factor p can be rewritten as

$$\Gamma = \frac{\left(\sqrt{\mu_{r2}/\varepsilon_{r2}} - \sqrt{\mu_{r1}/\varepsilon_{r1}}\right)}{\sqrt{\mu_{r2}/\varepsilon_{r2}} + \sqrt{\mu_{r1}/\varepsilon_{r1}}} \tag{4.6}$$

$$p = e^{-rd} \tag{4.7}$$

with d the length of sample.

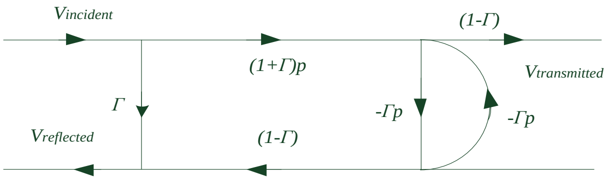

Fig.4.14. A signal-flow graph for the waveguides.

To deduce simultaneously material permittivity and permeability of the unknown sample, the relationship between the scattering parameters and reflected/transmitted parameters are needed. According to signal flow Fig.4.14, the scattering parameters S_{11} and S_{21} of the measuring setup, are obtained by

$$S_{11} = \frac{\Gamma\left(1-p^2\right)}{1-\Gamma^2 p^2} \tag{4.8}$$

$$S_{21} = \frac{p\left(1-\Gamma^2\right)}{1-\Gamma^2 p^2} \tag{4.9}$$

To write the formulation conveniently, the sum and difference of the scattering parameters are given by

$$V_1 = S_{21} + S_{11} \quad , \quad V_2 = S_{21} - S_{11}$$

let $x = \frac{1 - V_1 * V_2}{V_1 - V_2}$

By substituting measured scattering parameters from vector network analyzer into the signal flow formulation, the reflected/transmitted coefficient can be obtained. The direct inversion of this system of equations leads to the following relationships:

$$\Gamma = X + s_1\sqrt{X^2 - 1} \tag{4.10}$$

where s₁ = ±1, the choose of its sign requires the module of reflected coefficient $|\Gamma| \leq 1$. The transmitted coefficient is given by

$$p = \frac{V_1 - \Gamma}{1 - V_1 \Gamma} \tag{4.11}$$

Because of equation (4.6), the characteristic impedance in region II can be calculated from the measured reflection coefficient Γ, which is deduced as

$$Z_2 = Z_0 \sqrt{\frac{\mu_{r2}}{\varepsilon_{r2}}} = \frac{1+\Gamma}{1-\Gamma} Z_1 \tag{4.12}$$

$$\frac{\mu_{r2}}{\varepsilon_{r2}} = \frac{1+\Gamma}{1-\Gamma} \frac{Z_1}{Z_0} = \left(\frac{1+\Gamma}{1-\Gamma} \right)^2 \frac{\mu_{r1}}{\varepsilon_{r1}} \tag{4.13}$$

Since $p = e^{-\gamma d}$, the complex propagation constant γ will be find out

$$\gamma = \frac{1}{d} ln \frac{1}{p} \tag{4.14}$$

$$\gamma^2 = -\left(k_0^2 \mu_{r2} \varepsilon_{r2} - k_c^2 \right) \tag{4.15}$$

For TEM mode, $k_c = 0$. Based on the relationship above, the permittivity and permeability can then be derived. When very low losses assumption is used, we have the following relations

$$\sqrt{\frac{\mu_{r2} \varepsilon_{r1}}{\varepsilon_{r2}}} = \frac{1+\Gamma}{1-\Gamma} \tag{4.16}$$

$$\sqrt{\varepsilon_{r2} \mu_{r2}} = \frac{-\mathrm{j} * \arg(p) - \ln|p|}{k_0 d} \tag{4.17}$$

Where $k_0 = 2\pi f \sqrt{\mu_0 \varepsilon_0}$ is the propagation constant in free space. As ε_{r1} is a given design parameter, permittivity and permeability can be easily deduced from the above equations.

- **Modified Nicholson-Ross-Weir (NRW) algorithm for planar transmission line**

As discussed in IV.2.2, explicit relations between the propagation constant, the characteristic impedance of a TEM line and the parameters of the constituent material no longer exist in the cases of planar transmission line. Instead we use effective relative permittivity ε_e and permeability μ_e for a given planar line at a precise frequency.

The use of NRW algorithm gives the following parameters:

$$\varepsilon_2 = \varepsilon_0\left(\varepsilon_{reff\,2}' - j\varepsilon_{reff\,2}''\right) = \varepsilon_0\varepsilon_{reff\,2}\tan\delta_{\varepsilon ff}\,,\quad \mu_2 = \mu_0\left(\mu_{reff\,2}' - j\mu_{reff\,2}''\right) = \mu_0\mu_{reff\,2}\tan\delta_{\mu eff}$$

To obtain the sample relative permittivity and permeability a 2D inverse modeling is necessary with partially filled multilayered central section analyzed by a full wave 2D software so the accurate material electric properties lead to NRW algorithm deduced effective parameters. For this we define the following error function

$$error(x) = \left|\frac{\Gamma(x)|_{theo}}{\Gamma|_{meas}} - 1\right|^2 + \left|\frac{p(x)|_{theo}}{p|_{meas}} - 1\right|^2 \tag{4.18}$$

here the trial vector is given by $x = (\varepsilon', \varepsilon'', \mu', \mu'')$.

IV.4 NUMERICAL RESULTS

IV.4.1 Application to coaxial measurement cell

The inverse modeling procedure described in section IV.3.1 is applied to the measurement of a lossy ceramic ring. In our measurement setup, the total length of enlarged coaxial cell is 55.2 mm, with first 25.2 mm filled by air and last 30mm by SIC material. The SIC sample is ended by a short circuit plate. The inner and outer radius are respectively 8mm and 18mm for the ring sample, and the enlarged coaxial cell the inner and outer radius are respectively 6mm and 20mm. So we use 2mm thick Teflon to fill gap between ceramic ring and the inner conductor of coaxial cell.

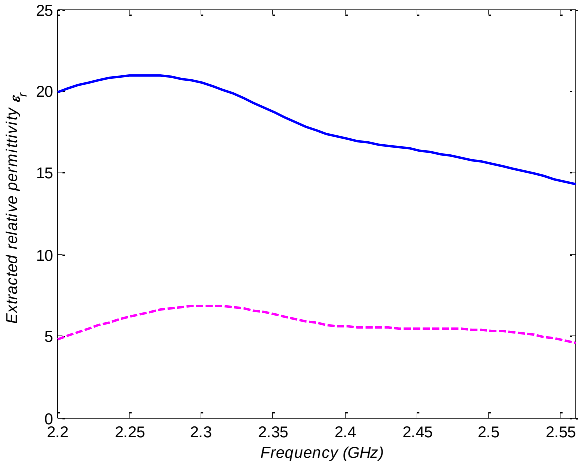

Fig.4.15. Real and imaginary (--) parts of extracted relative permittivity of sample under test.

A reflection measurement has been taken with the sample mounted in a 55.2mm length enlarged coaxial structure, with ring sample in touch with the shorting plate. The measured input impedance is that already obtained. By introducing the measured results in the inverse modeling, we have the extracted complex relative permittivity as shown in Fig.4.15.

We can observe the important imaginary part indicating the lossy nature of ceramic material under study. Extraction results for materials of same type obtained with different measurement cell are given in the following figures for comparison. As the latter sample is a ceramic cube with 6 faces difference may be important between extracted permittivity by using different face during measurement. Our results are certainly different compared to those of reference but within the variation range of this reference [IV-13].

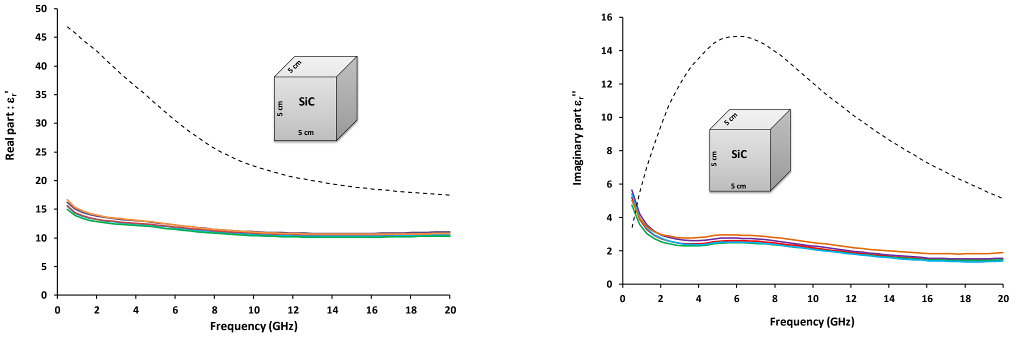

(a) (b)

Fig.4.16. Real (a) and imaginary (b) parts of relative permittivity published in [IV-13] with same ceramic material.

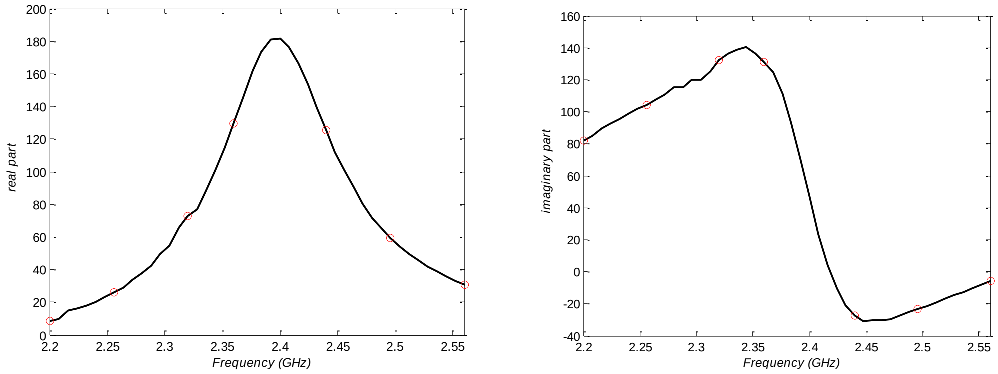

(a) (b)

Fig.4.17. Comparison of real (a) and imaginary (b) parts of input impedance between simulated data ('o') and measured results.

In order to validate further the inverse modeling results the extracted complex relative permittivity has been reintroduced to COMSOL simulation and the resulting reflection coefficient is used to determine new input impedance seeing from N connector by using equivalent network of transition section. Fig.4.17 compares the real and imaginary part obtained by respectively measurement and COMSOL simulation. Very good agreement can be observed.

IV.4.2 Applications to microstrip based measurement cell

First, the scattering parameters of test fixture are measured from VNA, then the transformations are needed to obtain the S-parameters between two ends of sample loaded part by making use of Thru-Reflect-Line (TRL) calibration procedure. Additionally, NRW algorithm allows the deduction of effective relative permittivity and permeability of sample loaded multilayered transmission line in a wide frequency range. Finally, the complex permittivity and permeability of materials can be extracted by using the inverse modeling described in IV.3.2.

- ***Alumina plate***

To illustrate this procedure, we consider the measurement of a two-inch square thin alumina slab. The application of NRW algorithm to the measurement results obtained in 200MHz-1.6GHz frequency range permits us to deduce the effective permittivity as in the following Fig.4.18.

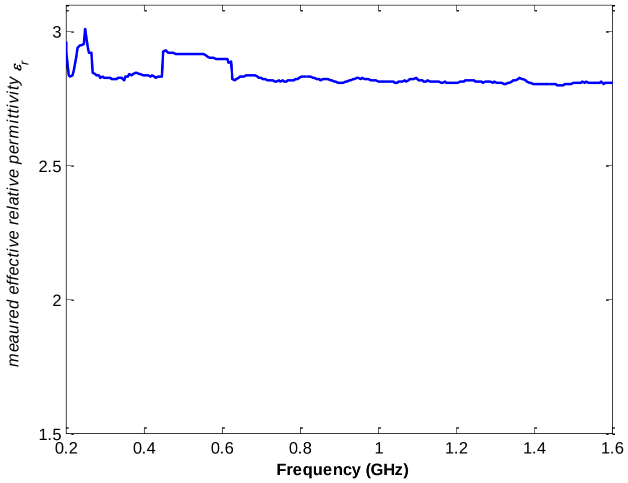

Fig.4.18. Effective relative permittivity of alumina covered microstrip line.

When introducing these results in the 2D inverse modeling program the frequency dependent relative permittivity is obtained and given in the following Fig.4.19.

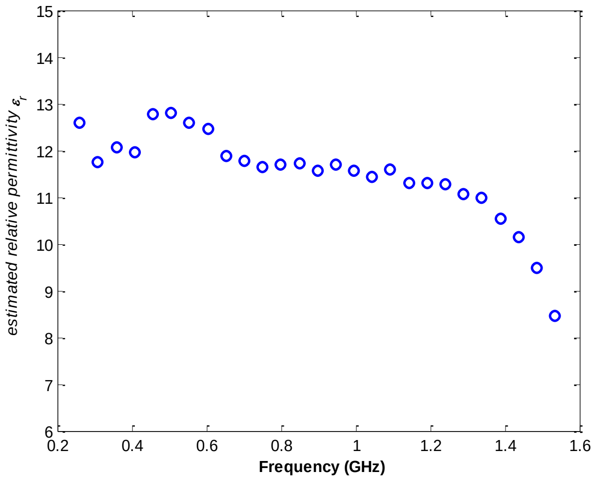

Fig.4.19. Relative permittivity of alumina slab obtained with inverse modeling.

We can note that in the center of frequency range the estimated relative permittivity is more important than that published in the most datasheet. To find the origin of this difference we should to reconsider the NRW algorithm. Indeed in the configuration studied by Nicholson, Ross and Weir no reactive electromagnetic energy in the discontinuities regions exist as the experimental setup does not give rise to higher order modes. This is unfortunately not the case with inhomogeneous transmission line such as the microstrip line. This reactive energy contributes to modifying the effective length of the central section, thus introducing a potentially large source of error. We propose an iterative procedure to minimize the error induced by the presence of this reactive energy by modeling it as a lumped reactive element, deduced from a 3D electromagnetic simulation of a simple junction. This procedure will be presented in the following.

◆ ***Modification of the NRW formulation with discontinuity effect correction***

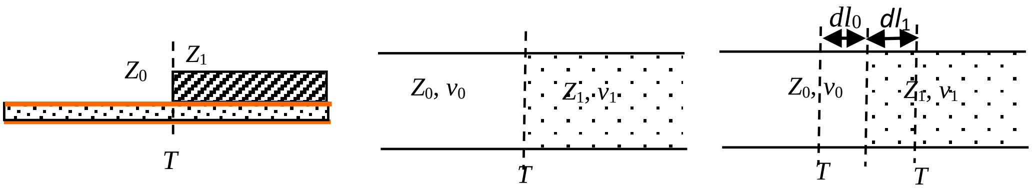

(a) (b) (c)

Fig.4.20. Junction model. (a) Real junction. (b) Ideal TEM junction. (c) Proposed junction model with presence of higher order modes.

The measurement cell using planar transmission line with introduction of the sample above the central strip line naturally leads to the presence of evanescent modes. This will introduce reactive energy accumulation in the vicinity of the discontinuities planes. In accordance with the nature of reactive energy, the length of the central section seen by fundamental mode will be different from the actual length. Instead of the actual value *d*, it is necessary to introduce d_{eff} as a function of the frequency (Fig.4.20(c)).

For each frequency, after the simulation by one of the numerical methods, the equivalent length will be deduced as function of the geometry and the relative permittivity value proposed for the material to be measured.

In the alumina slab measurement, junction model shows the evolution of the length dl_1 seeing from center part side, as a function of frequency and of the estimated relative permittivity in the case of alumina sample (Fig.4.21 (a)). This extra length can be great than 3mm in some case. Compared to 50.8mm, the real length of the central section, the influence may be important in the extraction results. The new estimated values ('+') of the sample are given in Fig.4.21(b) compared to those derived directly from the NRW formulations ('o'). These new values better correspond to those expected in the range between 9 and 11 as expected.

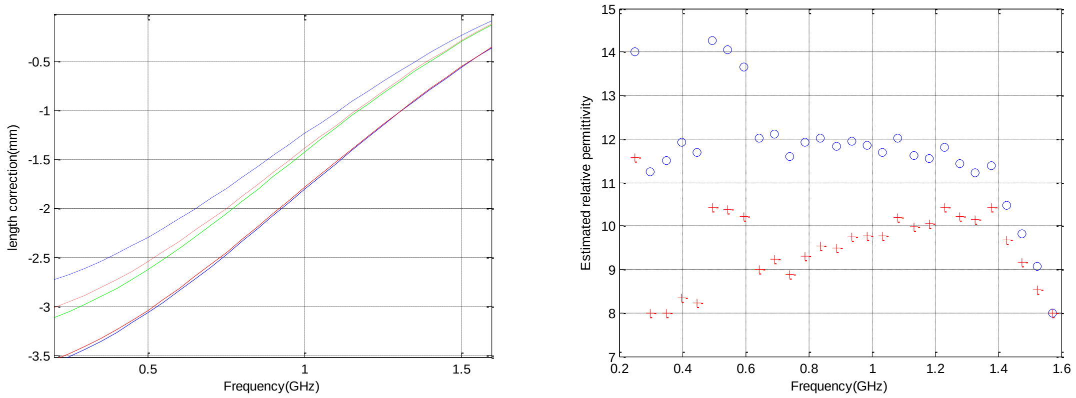

Fig.4.21. (a) Length correction. (b) Comparison between new values ('+') and old ones ('o').

- ***Transtech ceramic material***

Another example is presented here with the dielectric D-16 (Mg-Ti from Trans-Tech Company). The sizes of dielectric slab are of 30.94mm length and 1.02mm thickness.

Contrary to the above case we use 3D inverse modeling in which the entire measurement cell has been introduced in HFSS software. For low losses case, the reflection coefficient S_{11} is not very sensitive to the change of trial relative permittivity, so for simplify the numerical computation only S_{21} is considered in this study. This situation corresponds to c_1=0 case in equation (4.3).

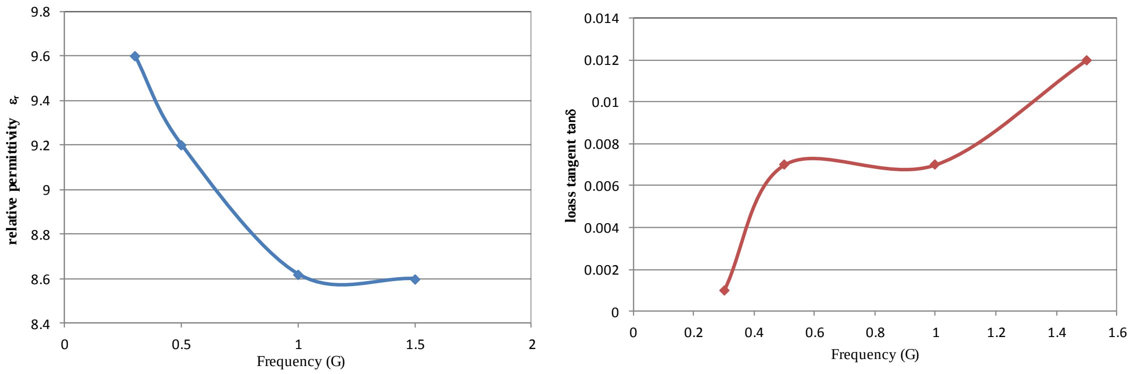

Fig.4.22. Extracted relative Permittivity ε_r and loss tangent tanδ of the sample.

The inverse modeling has been taken for four discrete frequencies, 0.3, 0.5,1, 1.5GHz, and the extracted real and imaginary parts of relative permittivity are shown in Fig.4.22. Table.4.2 compares the simulated and measurement S_{21} parameters for all 4 frequencies. We can note the relative good agreement.

Table.4.2 Frequency to frequency extraction.

f (G)	$\lvert S_{21}\rvert$_mes	ang (S_{21})_ mes(deg)	$\lvert S_{21}\rvert$_simu	ang(S_{21})_ simu (deg)	$\lvert S_{21}\rvert$_mes-$\lvert S_{21}\rvert$_simu |^2	|ang(S_{21})_mes - ang (S_{21}) _simu|^2
0.3	0.9997	-19.7	0.998483	-19.633	1.48109E-06	0.004548423
0.5	0.9974	-32.8	0.994978	-32.794	5.86608E-06	3.6E-05
1	0.99129	-64.969	0.988312	-64.965	8.86848E-06	1.6E-05
1.5	0.9925	-96.36	0.9903	-96.11	4.84E-06	0.0625

◆ *Uncertainty analysis*

For measurement accuracy, the three dimensions fixture should be designed carefully. Even though, its uncertainty analysis should be conducted systematically which includes algorithm uncertainty, air gap, sample positions. An air layer below sample slab should be taken into consideration for accurate simulation including when air gap between sample and substrate exist because of strip thickness (between 5μm and 35μm in our case). Also the determination of position of discontinuity planes may introduce error. All these error sources will be discussed in the following.

In the case of the D-16 material whose relative permittivity is given by TransTech Company which will be 16 at 9 GHz, and with low loss tangent less than 10^{-3}, there is a great difference between values from the datasheet and those from inverse modeling. The air gap can be the principal cause of measurement errors. One simple solution is to introduce a layer of air with given thickness between conducting strip and sample under test. The extracted relative permittivity with several air gap thicknesses is given in Fig.4.23. We can note that the choice of 0.1mm air gap produces results close to that of Company's datasheet. As the microstrip line is realized with soft substrate and the D-16 is hard material, the air gap of this value is not completely impossible. Other data are given in Table.4.3.

Table.4.3 Dimensions of support layer composition.

symbol	property	Value (mm)
t_1	Ground plane height	0.031
t_2	Support height	$\tau + \zeta$
τ	Strip thickness	0.031
ζ	Air gap between strip and sample	0～0.1

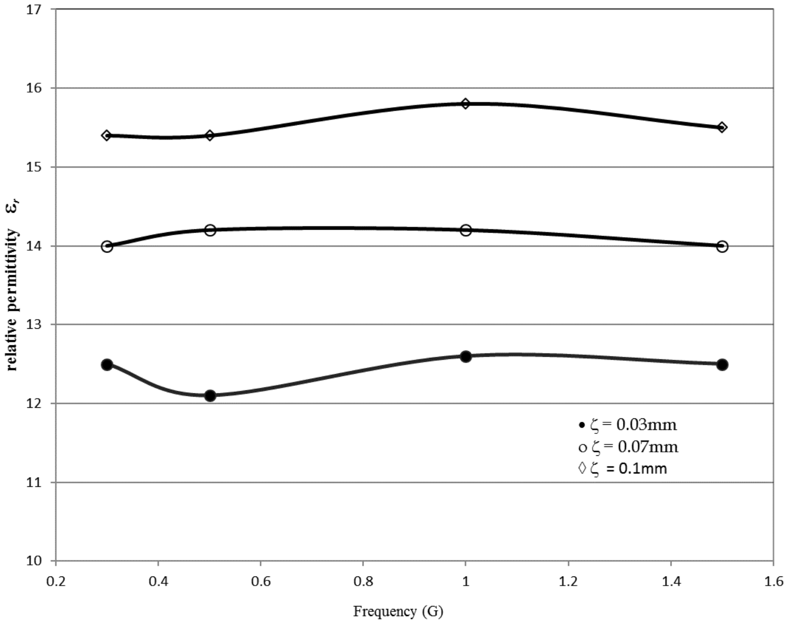

Fig.4.23. Relative Permittivity of the sample under study as function of frequency when the thickness of air gap ζ varies.

➢ ***Nanostructure composite sample***

In the precedent studies all materials have unit relative permeability that is no magnetic material has been studied. Here we consider several Fe-Al_2O_3 composite nanostructure samples (detail expressed in Appendix III) realized by CIRIMAT at Toulouse University (Fig.4.24(b)). All samples are metalized on one side. The rectangular plate of sizes 1.5mm × 28.51mm ×21.54mm was the subject of our research here. A square metal block with size ($28 \times 28 \times 15 mm^3$) is placed on the under-test sample for eliminating the air gap between strip line and sample. After applying the NRW algorithm to the measurement results, the raw results of complex effective relative permittivity and permeability of region loaded with sample are shown in Fig.4.25.

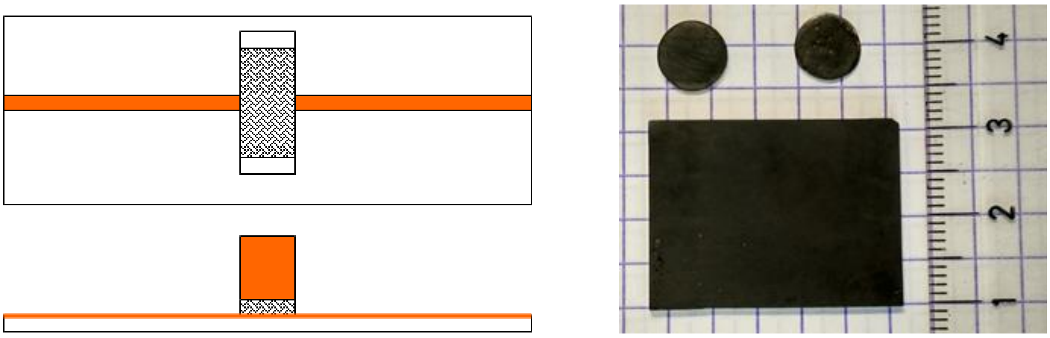

(a) (b)

Fig.4.24. (a) Measurement setup loaded by composite material. (b) Fe-Al2O3 composite prepared by spark plasma sintering (SPS).

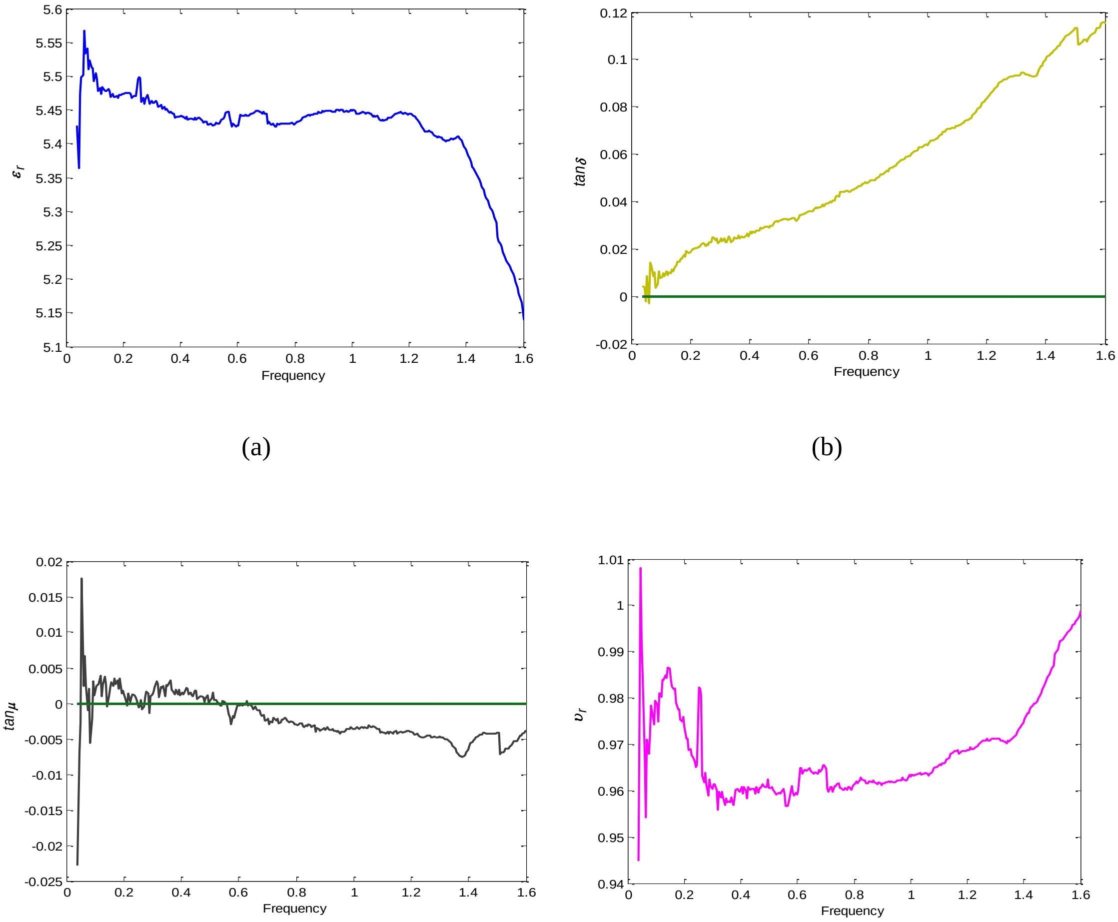

(a) (b)

(c) (d)

Fig.4.25. (a) Real part and (b) imaginary part of effective relative permittivity. (c) Real part and (d) imaginary part of effective relative permeability

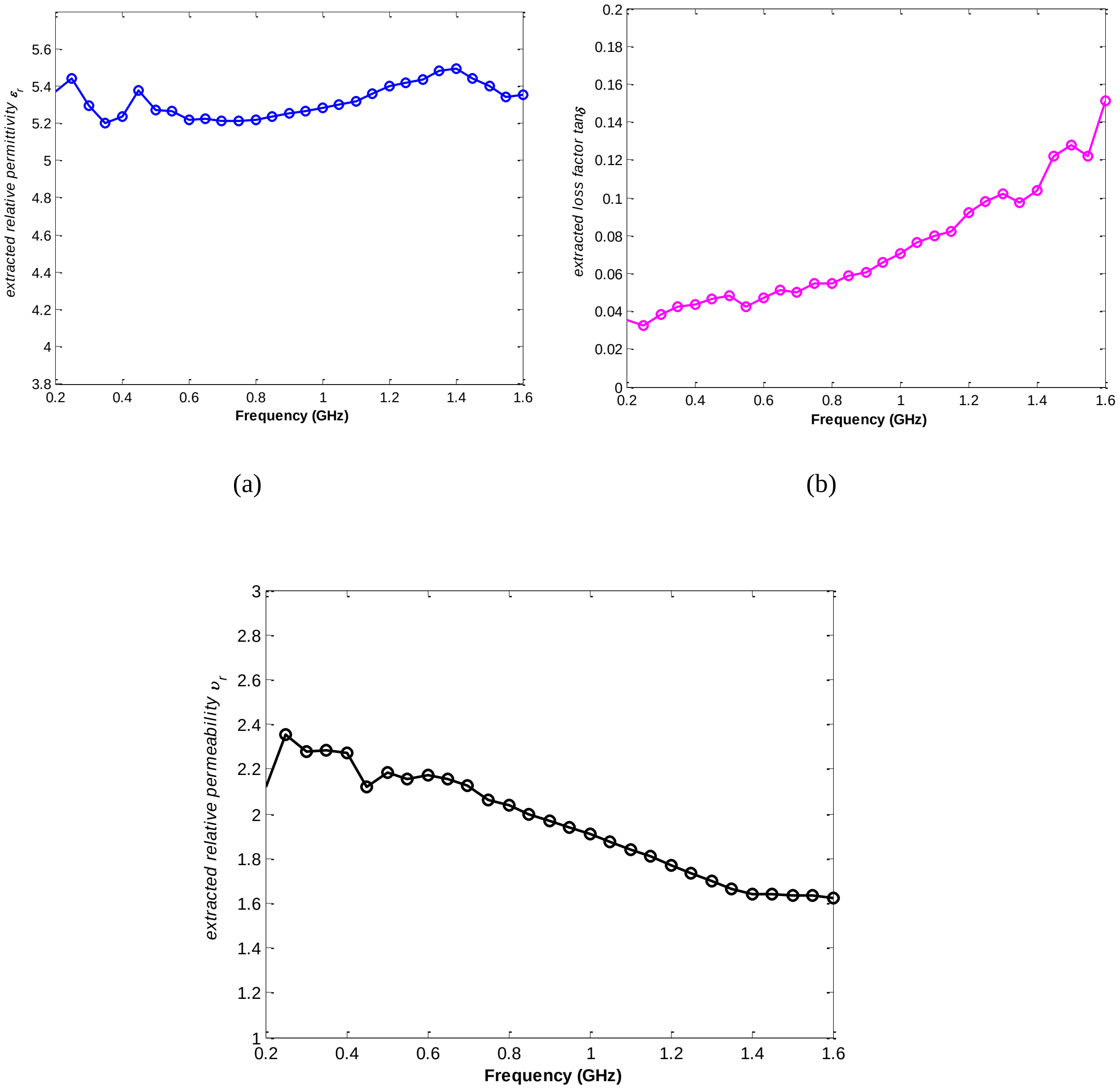

(a)

(b)

(c)

Fig.4.26. Electromagnetic properties of the sample. (a) Real part and (b) imaginary part of relative permittivity. (c) relative permeability.

The 2D inverse modelling procedure has been extended for magnetic material case. The extracted relative permittivity and the relative permeability of this nanostructured composite material are shown in Fig.4.26. We can remark that the sample under test shows significant losses and has magnetic properties.

IV.5 CONCLUSION

All theoretical formulations developed in the precedent chapters find their use in the practical dielectric measurement activity in this chapter, with two measurement cells used in LAPLACE laboratory: the coaxial one for large sample with ring forms, and the microstrip based one for smaller thin slab. Specific inverse modeling technique has been presented for each kind of material with appropriate corresponding measurement cell.

It is worth to note that the accurate electromagnetic modeling is not always possible for every situation. Face to this difficulty the experimental solution will be used instead. This is the case with conical transition used in coaxial measurement cell, and the same situation is present with SMA connector to straight microstrip line. With appropriate calibration techniques, the measurement results from experimental setup can be transformed to an equivalent problem in much simpler forms. For each case, the direct electromagnetic analysis requires much less computation resources. Moreover, simpler structure means much less error source and more quickly convergent numerical solution.

The extracted complex relative permittivity for ring form lossy ceramic sample has been obtained in frequency range between 2.3 and 2.5GHz. As the huge raw material is not perfectly homogeneous, comparison between our results and those obtained from other measurement techniques shows some dispersion. Nevertheless, our results are in the variation range of other published values.

For the low loss ceramic slabs both 2D and 3D inverse modeling procedures have been used to obtain relative permittivity comparable to values given in different datasheet. However, the air gap due to the conducting strip thickness can influence greatly the inverse modeling results. Attention must be paid for new material for which the dielectric constant range is by definition unknown.

A nanostructured Fe-Al_2O_3 composite has also studied in this work. The first results show some magnetic property as expected by Fe-Al_2O_3 inclusion. We can then conclude that our inverse modeling technique can be applied to magnetic materials also.

References of chapter IV

[IV-1]. L.F. Chen, C. K. Ong, C. P. Neo, V. V. Varadan, & V. K. Varadan. Microwave electronics: measurement and materials characterization. John Wiley & Sons, 2004.

[IV-2]. M. N. Afsar, "The measurement of the properties of materials." Proceedings of the IEEE 74.1 (1986): 183-199.

[IV-3]. J. Krupka, and C. Weil. "Recent advances in metrology for the electromagnetic characterization of materials at microwave frequencies." *Microwaves and Radar, 1998. MIKON'98., 12th International Conference on*. Vol. 4. IEEE, 1998.

[IV-4]. J. Baker-Jarvis, et al, "Measuring the permittivity and permeability of lossy materials: Solids, liquids, metals, building materials and negative-index materials," 2005.

[IV-5]. J. Baker-Jarvis, Transmission/reflection and short-circuit line permittivity measurements. Colorado: National Institute of Standards and Technology, 1990.

[IV-6]. S. Mumbongo-Kamboko, J. Tao, T.-H. Vuong, "Méthode de calibration d'une transition pour cellule de mesure des caractéristiques diélectriques des matériaux naturels," 10èmes Journées de Caractérisation Microondes et Matériaux - Limoges - 2 au 4 avril 2008.

[IV-7]. S. Mumbongo-Kamboko *et al.,*"Original calibration method for dielectric property measurement cell of natural materials," 12th International Conference on Microwave and High Frequency Heating, 7-10 September 2009, Karlsruhe, Germany

[IV-8]. J. W. Tao, G Angenieux, B. Flechet, "Accurate and fast characterization of a class of quasi planar structures," 23rd European Microwave Conference, 1993, Madrid, Spain

[IV-9]. A. M. Nicolson, and G. F. Ross. "Measurement of the intrinsic properties of materials by time-domain techniques." *IEEE Transactions on instrumentation and measurement* 19.4 (1970): 377-382.

[IV-10]. W. B. Weir, "Automatic measurement of complex dielectric constant and permeability at microwave frequencies." *Proceedings of the IEEE* 62.1 (1974): 33-36.

[IV-11]. E. J. Rothwell, *et al.* "Analysis of the Nicolson-Ross-Weir Method for Characterizing the Electromagnetic Properties of Engineered Materials." *Progress in Electromagnetics Research*157 (2016): 31-47.

[IV-12]. A. L. de Paula, M. C. Rezende, and J. J. Barroso. "Modified Nicolson-Ross-Weir (NRW) method to retrieve the constitutive parameters of low-loss materials." *Microwave & Optoelectronics Conference (IMOC), 2011 SBMO/IEEE MTT-S International*. IEEE, 2011.

[IV-13]. I. Polaert, et al., "Dielectric properties measurement methods for solids of high permittivity under microwave frequencies and between 20 and 250°C," Chemical Engineering and Processing Intensification, 2017.

[IV-14]. Z. C. Shi, et al. "Random composites of nickel networks supported by porous alumina toward double negative materials," *Advanced Materials* 24.17 (2012): 2349-2352.

[IV-15]. Z. D. Zhang, et al. "Tunable negative permittivity behavior and conductor–insulator transition in dual composites prepared by selective reduction reaction." *Journal of Materials Chemistry C* 1.1 (2013): 79-85.

[IV-16]. Z. C. Shi, et al. "Experimental realization of simultaneous negative permittivity and permeability in $Ag/Y_3Fe_5O_{12}$ random composites." *Journal of Materials Chemistry C* 1.8 (2013): 1633-1637.

[IV-17]. V. G. Veselago, "The electrodynamics of substances with simultaneously negative values of ε and μ." Sov. Phys. Usp., vol. 47, pp. 509–514, 1968.

[IV-18]. J. B. Pendry, "Negative refraction makes a perfect lens." *Physical review letters* 85.18 (2000): 3966.

[IV-19]. R. Marqués, F. Martin, and M. Sorolla, *Metamaterials with negative parameters: theory, design and microwave applications*. Vol. 183. John Wiley & Sons, 2011.

[IV-20]. X. Devaux, Ch. Laurent, and A. Rousset. "Chemical synthesis of metal nanoparticles dispersed in alumina." *Nanostructured Materials* 2.4 (1993): 339-346.

[IV-21]. Ch. Laurent, et al. "Reduction behaviour of $Fe_{3+/}Al_2O_3$ obtained from the mixed oxalate precursor and the formation of the Fe^0–Al_2O_3 metal–ceramic composite." *Journal of Materials Chemistry* 3.5 (1993): 513-518.

GENERAL CONCLUSION

This dissertation is to measure the materials' electromagnetic properties in the two transmission structures in LAPLACE laboratory, involving two measurement system, multilayered coaxial cell and multilayered planar structure. To obtain accurate parameters of samples under test in the material characterization, the enlarged coaxial cell is used for dielectric samples with ring forms, and the microstrip line is employed for the thin films over a broad frequency band by reflection method and transmission/ reflection method.

Material characterization composes of two essential parts: the direct problem and inverse problem. Numerical analysis of direct problem is carried out by programming codes in Matlab for the determination of propagation constants of multilayered guiding structures and the characterization of electromagnetic dispersion of uniaxial discontinuities compared with the simulated results from HFSS and COMSOL in chapters II and III. The inverse problem is implanted in Matlab framework based on an iterative optimization technique by comparing the measured and computed parameters from non-resonant methods for corresponding structures in chapter IV.

1. Transverse operator method is used for propagation constants of fundamental and higher-order modes in the stratified structure – coaxial cell. We studied the two-layered and three-layered enlarged coaxial cell considering the sample under test without and with loss.

2. Transverse resonance method is applied to the multilayered planar structure – microstrip line loaded different kinds of the samples for propagation constants without loss.

3. Mode matching method and multimodal variational methods are utilized for simple and multiple discontinuities in the two-layered coaxial cell filled with the ring-formed sample and the three-layered cell inserted with Teflon or filled with air near the inner conductor.

4. Multimodal variational method is also applied to the multiplanar structure discontinuity to obtain the series and shunt impedance of its corresponding equivalent T network of the double discontinuity.

5. The complex permittivity of the ring-formed ceramic sample with high loss has been extracted in the frequency range from 2.2 to 2.56 GHZ.

6. The complex permittivity and permeability of a nanostructured composite has been measured by the inverse modelling technique from 0.2 to 1.6 GHz.

Numerical formulations have been implanted in Matlab framework for corresponding structures used in the measurement cell. Numerical results have been obtained by the numerical methods and compared with those results from simulation software. Good agreements have been obtained for all cases, allowing the possibility to extract the materials' complex permittivity and permeability.

Perspective:

Some future work can be done:

1. For enlarged coaxial cell, the temperature-dependent complex permittivity of ceramic can be analyzed.
2. For microstrip line, the complex permittivity and complex permeability of double negative materials can be figured out.

APPENDIX I

Transverse Operator Method (TOM)

i. Definitions of the relative permeability tensor

$$\overline{\mu}_{tx}=\begin{bmatrix}0\\ jk\end{bmatrix},\ \ \overline{\mu}_{xt}=\begin{bmatrix}0 & -jk\end{bmatrix},\ \ \mu_{xx}=\mu_r\,,\overline{\overline{\mu}}_t=\begin{bmatrix}1 & 0\\ 0 & \mu_r\end{bmatrix}$$

$$\overline{\overline{\mu}}_E=\begin{bmatrix}1 & 0\\ 0 & \mu_r\end{bmatrix}-\frac{1}{\mu_r}\begin{bmatrix}0\\ jk\end{bmatrix}\begin{bmatrix}0 & -jk\end{bmatrix}=\begin{bmatrix}1 & 0\\ 0 & \mu_{eff}\end{bmatrix}$$

Where $\mu_{eff}=\dfrac{\mu_r^2-k^2}{\mu_r}$

The transverse operator in rectangular waveguide:

$$\overline{\overline{\mathcal{L}}}=\begin{bmatrix}\overline{\overline{\mathcal{L}}}_{11} & \overline{\overline{\mathcal{L}}}_{12}\\ \overline{\overline{\mathcal{L}}}_{21} & \overline{\overline{\mathcal{L}}}_{22}\end{bmatrix}=\begin{bmatrix}k_0\varepsilon_r-\dfrac{1}{k_0\mu_r}\begin{bmatrix}-\gamma\\ -j\alpha\end{bmatrix}\begin{bmatrix}\gamma & j\alpha\end{bmatrix} & -\begin{bmatrix}-\gamma\\ -j\alpha\end{bmatrix}\dfrac{\begin{bmatrix}0 & -jk\end{bmatrix}}{\mu_r}\\ -\dfrac{1}{\mu_r}\begin{bmatrix}0\\ jk\end{bmatrix}\begin{bmatrix}\gamma & j\alpha\end{bmatrix} & k_0\begin{bmatrix}1 & 0\\ 0 & \mu_{eff}\end{bmatrix}-\dfrac{1}{k_0\varepsilon_r}\begin{bmatrix}-\gamma\\ -j\alpha\end{bmatrix}\begin{bmatrix}\gamma & j\alpha\end{bmatrix}\end{bmatrix}$$

$$\overline{\overline{\mathcal{L}}}_{11}=\frac{1}{k_0\mu_r}\begin{bmatrix}k_0^2\varepsilon_r+\gamma^2 & j\alpha\gamma\\ j\alpha\gamma & k_0^2\varepsilon_r\mu_r-\alpha^2\end{bmatrix}$$

$$\overline{\overline{\mathcal{L}}}_{12}=-\frac{1}{\mu_r}\begin{bmatrix}0 & jk\gamma\\ 0 & -k\alpha\end{bmatrix}$$

$$\overline{\overline{\mathcal{L}}}_{21}=-\frac{1}{\mu_r}\begin{bmatrix}0 & 0\\ jk\gamma & -k\alpha\end{bmatrix}$$

$$\overline{\overline{\mathcal{L}}}_{22}=\frac{1}{k_0\varepsilon_r}\begin{bmatrix}k_0^2\varepsilon_r+\gamma^2 & j\alpha\gamma\\ j\alpha\gamma & k_0^2\varepsilon_r\mu_{eff}-\alpha^2\end{bmatrix}$$

ii. Transverse operator in polar coordinate

$$\overline{\overline{\mathcal{L}}} = \begin{bmatrix} \overline{\overline{\mathcal{L}}}_{11} & \overline{\overline{\mathcal{L}}}_{12} \\ \overline{\overline{\mathcal{L}}}_{21} & \overline{\overline{\mathcal{L}}}_{22} \end{bmatrix} = \begin{bmatrix} k_0\varepsilon_r - \frac{1}{k_0\mu_r}\begin{bmatrix} -\gamma \\ 0 \end{bmatrix}\begin{bmatrix} \gamma & 0 \end{bmatrix} & 0 \\ 0 & k_0\mu_r - \frac{1}{k_0\varepsilon_r}\begin{bmatrix} -\gamma \\ 0 \end{bmatrix}\begin{bmatrix} \gamma & 0 \end{bmatrix} \end{bmatrix}$$

with

$$\overline{\overline{\mathcal{L}}}_{11} = \begin{bmatrix} k_0\varepsilon_r + \gamma^2 / k_0\mu_r & 0 \\ 0 & k_0\varepsilon_r \end{bmatrix}$$

$$\overline{\overline{\mathcal{L}}}_{22} = \begin{bmatrix} k_0\mu_r + \gamma^2 / k_0\varepsilon_r & 0 \\ 0 & k_0\mu_r \end{bmatrix}$$

Definitions of the variables:

$$k_\varepsilon = k_0\varepsilon_r$$

$$k_{\varepsilon r} = k_0\varepsilon_r + \gamma^2 / k_0\mu_r$$

$$k_\mu = k_0\mu_r$$

$$k_{\mu r} = k_0\mu_r + \gamma^2 / k_0\varepsilon_r$$

$$\lambda = k_0^2\varepsilon_r\mu_r + \gamma^2$$

Definitions of the K matrix:

$$\overline{\overline{K}} = \begin{bmatrix} \overline{\overline{K}}_{11} & \overline{\overline{K}}_{12} \\ \overline{\overline{K}}_{21} & \overline{\overline{K}}_{22} \end{bmatrix}$$

With

$$\overline{\overline{K}}_{11}=\begin{bmatrix}0 & \sqrt{\lambda}J_0^{'}\left(\sqrt{\lambda}\rho\right)/k_{\varepsilon r}\\ \sqrt{\lambda}J_0^{'}\left(\sqrt{\lambda}\rho\right)/k_{\mu r} & 0\end{bmatrix}$$

$$\overline{\overline{K}}_{12}=\begin{bmatrix}0 & \sqrt{\lambda}Y_0^{'}\left(\sqrt{\lambda}\rho\right)/k_{\varepsilon r}\\ \sqrt{\lambda}Y_0^{'}\left(\sqrt{\lambda}\rho\right)/k_{\mu r} & 0\end{bmatrix}$$

$$\overline{\overline{K}}_{21}=\begin{bmatrix}J_0\left(\sqrt{\lambda}\rho\right) & 0\\ 0 & J_0\left(\sqrt{\lambda}\rho\right)\end{bmatrix}$$

$$\overline{\overline{K}}_{22}=\begin{bmatrix}Y_0\left(\sqrt{\lambda}\rho\right) & 0\\ 0 & Y_0\left(\sqrt{\lambda}\rho\right)\end{bmatrix}$$

$$\begin{bmatrix}e_\varphi(\rho)\\ h_\varphi^{'}(\rho)\\ e_z(\rho)\\ h_z^{'}(\rho)\end{bmatrix}=\begin{bmatrix}0 & \sqrt{\lambda}J_0^{'}\left(\sqrt{\lambda}\rho\right)/k_{\varepsilon r} & 0 & \sqrt{\lambda}Y_0^{'}\left(\sqrt{\lambda}\rho\right)/k_{\varepsilon r}\\ \sqrt{\lambda}J_0^{'}\left(\sqrt{\lambda}\rho\right)/k_{\mu r} & 0 & \sqrt{\lambda}Y_0^{'}\left(\sqrt{\lambda}\rho\right)/k_{\mu r} & 0\\ J_0\left(\sqrt{\lambda}\rho\right) & 0 & Y_0\left(\sqrt{\lambda}\rho\right) & 0\\ 0 & J_0\left(\sqrt{\lambda}\rho\right) & 0 & Y_0\left(\sqrt{\lambda}\rho\right)\end{bmatrix}\begin{bmatrix}c_1\\ c_2\\ c_3\\ c_4\end{bmatrix}$$

iii. Definition of the matrices by making used of the boundary conditions

I. Surface $\rho=a$,

$$\Psi_m\Big|_{(\rho=a)}=\begin{bmatrix}J_{sa}\\ 0\end{bmatrix}=\overline{\overline{M}}_1\begin{bmatrix}d_1\\ d_2\end{bmatrix}$$

II. Interface $\rho=a+d$ and $\rho=a+d+\xi$

$$\Psi_m\Big|_{(\rho=a+d)}=\overline{\overline{M}}_2\begin{bmatrix}d_1\\ d_2\end{bmatrix}=\overline{\overline{M}}_2\overline{\overline{M}}_1^{-1}\begin{bmatrix}J_{sa}\\ 0\end{bmatrix}$$

$$\Psi_m \Big|_{(\rho=a+d+\xi)} = \overline{\overline{M}}_3 \begin{bmatrix} d_3 \\ d_4 \end{bmatrix}$$

$$\Psi_m \Big|_{(\rho=a+d)} = \Psi_m \Big|_{(\rho=a+d+\xi)}$$

$$\begin{bmatrix} d_3 \\ d_4 \end{bmatrix} = \overline{\overline{M}}_3^{-1} \overline{\overline{M}}_2 \overline{\overline{M}}_1^{-1} \begin{bmatrix} J_{sa} \\ 0 \end{bmatrix}$$

III. Surface $\rho=b$

$$\Psi_m \Big|_{(\rho=b)} = \begin{bmatrix} J_{sb} \\ 0 \end{bmatrix} = \overline{\overline{M}}_4 \begin{bmatrix} d_3 \\ d_4 \end{bmatrix}$$

$$\begin{bmatrix} J_{sb} \\ 0 \end{bmatrix} = \overline{\overline{M}}_4 \overline{\overline{M}}_3^{-1} \overline{\overline{M}}_2 \overline{\overline{M}}_1^{-1} \begin{bmatrix} J_{sa} \\ 0 \end{bmatrix}$$

APPENDIX II

Mode matching method (MMM)

$$\iint_{Su} \vec{u}_z \cdot \left((3.1) \times \vec{h}_{tp}^{(1)*} \right) ds \xrightarrow{yield} \sum_{i=1}^{n} \overline{\overline{N}}_p^{(1)} \left(a_p^{(1)} + b_p^{(1)} \right) = \sum_{i=1}^{m} \overline{\overline{HE}}_{mp}^{(12)} \left(a_m^{(2)} + b_m^{(2)} \right)$$

$$\iint_{Su} \vec{u}_z \cdot \left((3.1) \times \vec{h}_{tq}^{(2)*} \right) ds \xrightarrow{yield} \sum_{i=1}^{n} \overline{\overline{EH}}_{nq}^{(12)} \left(a_n^{(1)} + b_n^{(1)} \right) = \sum_{i=1}^{m} \overline{\overline{N}}_q^{(2)} (a_q^{(2)} + b_q^{(2)})$$

$$\iint_{Sc} \vec{u}_z \cdot \left(\vec{e}_{tp}^{(1)*} \times (3.2) \right) ds \xrightarrow{yield} \sum_{i=1}^{n} \overline{\overline{EH}}_{pn}^{(11)*} \left(a_n^{(1)} - b_n^{(1)} \right) = \sum_{j=1}^{m} \overline{\overline{EH}}_{pm}^{(12)*} \left(a_m^{(2)} - b_m^{(2)} \right)$$

$$\iint_{Sc} \vec{u}_z \cdot \left(\vec{e}_{tq}^{(2)*} \times (3.2) \right) ds \xrightarrow{yield} \sum_{i=1}^{n} \overline{\overline{HE}}_{qn}^{(12)*} \left(a_n^{(1)} - b_n^{(1)} \right) = \sum_{i=1}^{m} \overline{\overline{EH}}_{qm}^{(22)*} \left(a_m^{(2)} - b_m^{(2)} \right)$$

where

$$\overline{\overline{EH}}_{np}^{(11)} = \iint \bar{u}_z \cdot \left(\vec{e}_{tn}^{(1)} \times \vec{h}_{tp}^{(1)*} \right) ds$$

$$\overline{\overline{HE}}_{mp}^{(12)} = \iint \bar{u}_z \cdot \left(\vec{e}_{tm}^{(2)} \times \vec{h}_{tp}^{(1)*} \right) ds$$

$$\overline{\overline{EH}}_{nq}^{(12)} = \iint \bar{u}_z \cdot \left(\vec{e}_{tn}^{(1)} \times \vec{h}_{tq}^{(2)*} \right) ds$$

$$\overline{\overline{EH}}_{mq}^{(22)} = \iint \bar{u}_z \cdot \left(\vec{e}_{tm}^{(2)} \times \vec{h}_{tq}^{(2)*} \right) ds$$

$$\overline{\overline{N}}_p^{(1)} = \iint \bar{u}_z \cdot \left(\vec{e}_{tn}^{(1)} \times \vec{h}_{tp}^{(1)*} \right) ds$$

$$\overline{\overline{N}}_q^{(2)} = \iint \bar{u}_z \cdot \left(\vec{e}_{tm}^{(2)} \times \vec{h}_{tq}^{(2)*} \right) ds$$

APPENDIX III

Nanostructured Material

Nanostructured materials and nanocomposites have specific properties thanks to their nanoscale and are serious candidates in mechanical, electrical, chemical and environmental applications. Among their many physical properties, their capacity to interact with electromagnetic waves is particularly interesting because potentially source of new functionalities [IV-14]-[IV-16]. The composite magnetic powder is one of the artificial material, also called metamaterial. The metamaterial is usually assembled from composite materials such as metals or plastics for manipulating electromagnetic properties. One of the most popular artificial materials is negative index material first described theoretically by Victor Veselago [IV-17]. A left-handed metamaterial was identified by John Pendry as a practical realization of such media [IV-18]. In the last decades, the number of papers related to metamaterials such as negative refraction, or cloaking has grown exponentially which is explicated in the book [IV-19]. It is a common sense that if both permittivity ε and permeability μ are positive, wave propagation travels in the forward direction; if both ε and μ are negative, known as left-handed media, a backward wave comes into existence which only exhibit in metamaterials. In other words, these two parameters determine the propagation of electromagnetic waves in matter, and they are controlled and altered by adjusting the shape, size and configuration of the unit cells in the construction. So, the composite materials by the researchers are produced in the labs including our patterner-CIRIMAT (short for Centre Interuniversitaire de Recherche et d'Ingénierie des Matériaux).

Many of the most pressing scientific problems are currently due to the limits of the materials that are available. Thus, breakthroughs in materials science are likely to affect the future of technology significantly. So, the emphasization to the understanding of processing-structure-properties correlation helps to develop new and advance materials, including nanomaterials. Nanostructured materials are that its elements – clusters, crystallites or molecules – have dimensions in the 1 to 100 nanometers (10^{-9} meter) range, and they exhibit many unique electrical, magnetic, optical, and mechanical properties. It is a subject of intense research in the material science community and its explosion in both academic and industrial interest arises dramatically in support of manufacturing processes.

Nanostructured materials and nanocomposites have specific properties thanks to their nanoscale and are serious candidates in mechanical, electrical, chemical and environmental applications. Among their many physical properties, their capacity to interact with electromagnetic waves is particularly interesting because potentially source of new functionalities. Random composite materials combining a ferromagnetic metal within an oxide matrix have demonstrated their potential as double negative materials (DNM). DNM exhibit both negative electric permittivity and negative magnetic permeability leading to unique properties in terms of wave propagation with high breakthrough potential, especially in fields such as optics (superlenses) or electromagnetic cloaking (invisibility cloaking). Such composites are bulk 3D materials with isotropic electromagnetic properties originating from their composition and microstructure. An Fe-Al_2O_3 composite powder was prepared by a method involving the selective reduction of an oxide solid solution. First, the mixed oxalate $(NH_4)_3Al_{0.8}Fe_{0.2}(C_2O_4)_3$, nH_2O is obtained by precipitation in alcohol. Heat-treatment in air (400 °C, 2 h) leads to the decomposition of the oxalate and the formation of the amorphous $(Al_{0.8}Fe_{0.2})_2O_3$ solid solution [IV-20]. Heat-treatment in H_2 (1100°C, 5h) then produces the reduction of the ferric ions to metallic iron, forming the Fe-Al_2O_3 composite powder [IV-21]. The iron content in the composite is equal to 12.0 vol.%, well below percolation threshold evaluated at about 30 vol.%. The specimen is thus an insulating material. The so-obtained powder was consolidated by spark plasma sintering (SPS) (1400 °C, 3 min, 50 MPa) to obtain pellets 8 mm and 50 mm in diameter and 1.5 mm thick (PNF^2-Toulouse, Dr. Sinter 2080, SPS Syntex Inc., Japan). Then, the 50-mm pellet was cut into rectangle 28.5 x 21.5 mm for the electromagnetic measurements. A typical FEG-SEM image (recorded in backscattered electron chemical composition mode to enhance contrast) of a cross-section of the Fe-Al_2O_3 composite reveals that the Fe particles (appearing as white dots on the image) are homogeneously dispersed into the Al_2O_3 matrixThe diameter of the Fe particles was measured on hundreds of particles on such images and the distribution (inset in Fig.4.27) lies in the range 0.2 µm to 5.7 µm in diameter, with a median value of 0.7 µm.

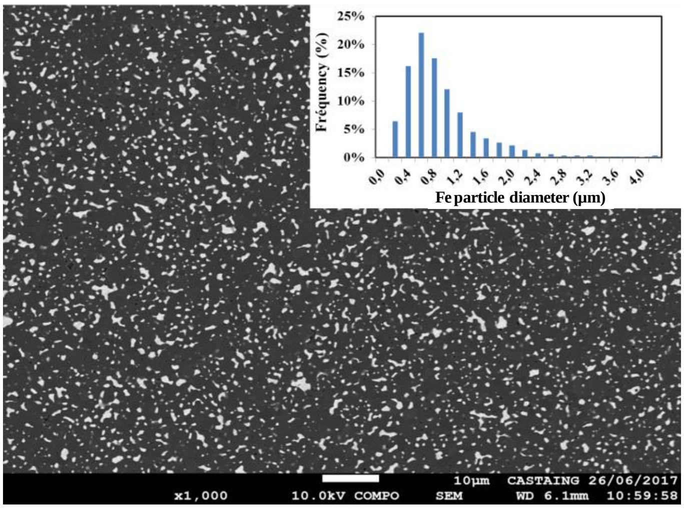

Fig.4.27. FEG-SEM image of a cross-section of the 12 vol.% Fe-Al2O3 composite and the corresponding Fe particle diameter distribution.

Résumé en française

INTRODUCTION

Aujourd'hui, les matériaux hyperfréquences ont été largement utilisés dans les diverses applications dans les domaines de radiofréquences et hyperfréquences. La connaissance précise de leurs propriétés est une condition indispensable au développement de dispositifs dans la bande de fréquence d’application. Cependant pour un certain nombre de matériaux, les propriétés électriques ne sont pas aussi précises qu'elles ne devraient l'être, ou ne sont pas à la bonne fréquence pour laquelle l'application fonctionne. C'est pour cela que les activités de caractérisation des propriétés des matériaux occupent toujours une place importante que ce soit en recherche fondamentale ou dans beaucoup de secteurs industriels.

Pour la caractérisation des matériaux hyperfréquences, les méthodes de mesure ont été développées et appliquées à la caractérisation des matériaux au cours des dernières décennies. Néanmoins la mesure précise des propriétés des matériaux hyperfréquences reste toujours un défi à relever malgré l’abondance de méthodes développées et employées pour la mesure de la perméabilité et de la permittivité publiées dans beaucoup de revues scientifiques ainsi que de nombreux ouvrages spécialisés. Pour chaque cas, une ou plusieurs techniques peuvent être utilisées en fonction de la configuration expérimentale. Dans la plupart des cas, il n'existe pas de relations directes entre les paramètres mesurables et les propriétés électriques. Par conséquent l'extraction des propriétés matériaux doit être menée par des modélisations inverses basées le plus souvent sur l'analyse électromagnétique rigoureuse des cellules spécifiques de mesure et les mesures expérimentales des paramètres liés aux effets de propagation ou résonance des ondes électromagnétiques dans ces cellules.

Le cadre de ces travaux est présenté en quatre chapitres :

- Le premier chapitre présente l'introduction générale de la problématique de caractérisation des matériaux. Le choix des méthodes de mesure est basé sur les exigences de précision et de structures de mesure, et les méthodes numériques donnent les bases de l'analyse électromagnétiques rigoureuse, efficace et précise des cellules de mesure utilisées dans ce travail.

- Le deuxième chapitre est consacré à la description des méthodes bidimensionnelles (2D) pour caractériser la propagation des ondes dans des structures de propagation en présence des matériaux inconnus. On présentera en particulier la méthode de l’opérateur transverse et celle des résonances transverses, qui ont permis de déterminer les différents modes, propagatifs ou évanescents, dans des structures coaxiales et des structures planaires.

- Le troisième chapitre introduit la caractérisation des discontinuités par les méthodes tridimensionnelles (3D) dans les cellules de mesure de formes coaxiales et planaires. Ces analyses théoriques ont été validées par comparaison avec les résultats simulés par logiciel commercial basé sur la méthode des éléments finis.
- Le quatrième chapitre met en application les méthodes 2D et 3D dans l’objectif d’extraire les propriétés matériaux à partir des mesures réalisées à l’aide d’analyseur de réseaux vectoriels (VNA). La résolution des problèmes directs et inverses sera décrite et validée par des études de différents matériaux à pertes modérées et fortes ainsi qu’un exemple de matériau composite nano structuré.

Méthodes de mesure

Dans les bandes de fréquences RF et hyperfréquences, la caractérisation des matériaux implique le choix de méthodes de mesure. Les plus utilisés peuvent être classés en méthodes non résonnantes et en méthodes résonantes. Les méthodes non-résonnantes sont souvent utilisées pour obtenir une connaissance générale des propriétés électromagnétiques sur une large gamme de fréquences, tandis que les méthodes résonantes sont utilisées pour obtenir des connaissances précises à une seule fréquence ou à plusieurs fréquences discrètes. Les méthodes non-résonnantes et la méthode résonante sont complémentaires et souvent combinées pour obtenir une connaissance plus précise des propriétés du matériau.

Pour les *méthodes résonnantes*, nous pouvons considérer la cellule de mesure comme un circuit résonant généralisé, souvent matérialisé par une cavité résonnante. Les fréquences de résonance et le facteur de qualité associé à chaque fréquence de résonance sont deux quantités qui peuvent être déterminées avec un instrument de mesure hyperfréquence tel qu'un analyseur de réseau vectoriel (VNA) ou un impédance mètre pour un coût beaucoup plus modeste. Si une cavité métallique est utilisée, le facteur de qualité peut être très élevé, ce qui conduit à une détermination très précise des fréquences de résonance. La précision sera moindre avec les résonateurs planaires car le facteur de qualité sera beaucoup moindre. Quand un matériau à forte pertes est considéré, en fonction de la taille de l'échantillon, la résonance peut complètement disparaître. C’est pourquoi ce type de méthodes n'est pas adapté à la mesure de matériaux à forte perte.

Avec les *méthodes non-résonnantes*, les propriétés des matériaux sont fondamentalement déduites de l'impédance caractéristique et des vitesses d'onde d'une structure guidante remplie de matériaux à mesurer. Lorsqu'une onde électromagnétique se propage d'une structure à une autre, l'impédance d'onde caractéristique et la vitesse d'onde changent, entraînant une réflexion partielle de l'onde électromagnétique à partir de l'interface entre deux structures remplies de matériaux différents. La mesure de la réflexion et de la transmission peut fournir des informations à partir desquelles la déduction des relations de permittivité et de perméabilité sera faite.

Cellules de mesure

Dans notre étude, l'échantillon annulaire est inséré dans une certaine position de la cellule coaxiale multicouche élargie (Fig.1), ce qui affecte l'impédance caractéristique. L'appareil de mesure de la cellule coaxiale élargie est conçu pour satisfaire aux exigences de mesure spéciales afin d'augmenter la précision et la sensibilité. La méthode de transmission/réflexion sur circuit planaire est basée sur l'algorithme de la méthode de Nicolson-Ross-Weir qui a été adapté pour la structure de la ligne micro-ruban (Fig.2). L'impédance caractéristique et la constante de propagation sont des fonctions des propriétés diélectriques et magnétiques du substrat de référence et des matériaux à mesurer. Si l’échantillon sous test (EST) est inséré dans un segment de ligne de transmission, les constantes de propagation et l’impédance caractéristique de la ligne de transmission seront modifiées. A partir de la réflexion au plan de discontinuité, les propriétés électromagnétiques de l’EST peuvent être déduites.

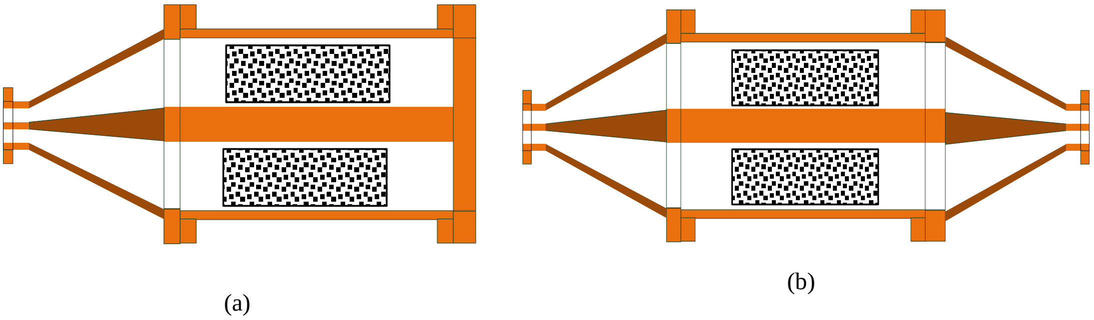
(a)

(b)

Fig.1. Cellules de mesure coaxiales. (a) Cellule en réflexion ; (b) Cellule en réflexion/transmission.

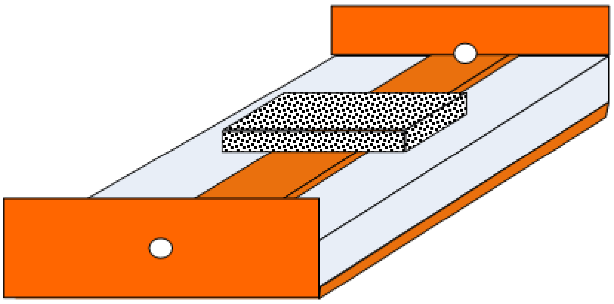

Fig.2. Cellule de mesure micro-ruban.

Méthodes numérique d’analyse électromagnétique

La caractérisation des propriétés matériau à partir des paramètres mesurés comprend principalement deux étapes : problème direct et problème inverse. Dans le problème direct, une analyse électromagnétique précise sera effectuée sur une cellule de mesure dans laquelle des valeurs estimées de permittivité et de perméabilité seront utilisées, conduisant à la solution complète de l'équation de Maxwell avec des conditions aux limites fixes. A partir de la solution de Maxwell, tous les paramètres physiques tels que les fréquences de résonance, les facteurs de qualité, la réflexion et la transmission peuvent être déduits en utilisant des techniques de post-traitement. Toutes sont fonction de la valeur d'essai de la permittivité et de la perméabilité à une fréquence donnée. En raison de la complicité des cellules de mesure dans la plupart des cas, aucune expression analytique n'est disponible pour la résolution des équations de Maxwell. Des techniques numériques seront utilisées pour obtenir des solutions approximatives.

Méthodes basées sur la discrétisation spatiale. La complexité des structures de propagation d'ondes rend la solution analytique aux équations de Maxwell irréalisable, par conséquent, des méthodes numériques prennent de l'importance et deviennent plus attrayante avec l'avènement de l'ordinateur. Pour convertir des équations différentielles ou intégrales en système d'équations linéaires, le champ électromagnétique inconnu sera exprimé comme une combinaison linéaire d'un ensemble de fonctions mathématiques connues de type scalaire ou vectoriel. Lorsque cette approximation est prise en subdivisant l’espace entier en un grand nombre de petits sous-espaces, la méthode est considérée de type « discrétisation spatiale ». C'est le cas de la plupart des solveurs commerciaux, à savoir, Ansoft HFSS, COMSOL Multiphysics, et CST Microwave studio.

Méthodes basées sur la décomposition modale. Avec les logiciels commerciaux, la discrétisation spatiale de configurations complexes consomme de la mémoire informatique et la résolution des équations prend beaucoup de temps. Pour des structures de grandes dimensions par rapport à la longueur d'onde, on a affaire avec de très grande matrices et par conséquent un temps de calcul généralement important. Comme la modélisation inverse nécessite souvent un grand nombre d'analyses directes avant d'obtenir des résultats convergents, l'efficacité numérique devient un critère clé. Le développement d'outils spécifiques avec des performances numériques croissantes est l'objectif de la plupart des méthodes basées sur la décomposition modale nécessitant la résolution des problèmes aux valeurs propres sur des structures élémentaires. Ces méthodes sont souvent développées par des chercheurs universitaires pour des structures complexes avec plusieurs avantages.

- ✓ Plus de souplesse
- ✓ Mieux ciblé

Dans notre étude, la connaissance des capacités et des limites de ces algorithmes numériques permet de mieux comprendre leur impact sur diverses applications dans le problème direct et ouvre la voie à d'autres recherches.

ETUDE BIDIMENSIONNELLE AUX VALEURS PROPRES

Les cellules de mesure de matériau diélectrique dans la gamme RF et micro-ondes font souvent appel aux effets de propagation ou de résonance d'ondes électromagnétiques. En conséquence, ces systèmes de mesure sont souvent construits autour des structures de propagation des ondes. L'analyse électromagnétique directe de ces cellules par des méthodes modales nécessite la connaissance de la base modale dans ces structures. Pour des cellules ciblées par les travaux de cette thèse nous devons étudier des structures stratifiées.

Analyse théorique

Les cellules ciblées dans cette étude concernent une cellule coaxiale et une cellule en ligne planaire. La présence d'un matériau inconnu est modélisée par une structure de transmission hétérogène stratifiée. L'application de la méthode de l'opérateur transverse (TOM) sur la cellule coaxiale multicouche a permis la détermination de la constante de propagation du mode fondamental, la répartition des champs électromagnétique, et les caractéristiques des modes d'ordre supérieurs pour le besoin de la caractérisation des discontinuités entre lignes non remplie et partiellement remplie. Dans le cas de la cellule à base d'une ligne micro-ruban l'utilisation de la méthode de résonance transverse modifiée (MTRM) a permis la détermination des caractéristiques des modes d'ordre fondamental et supérieur.

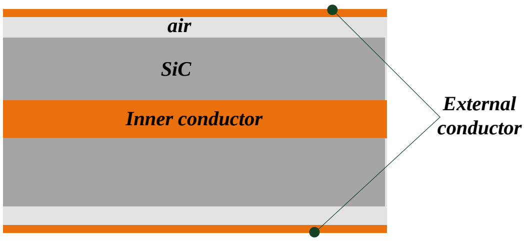

Fig.3. Longitudinal cross section of coaxial cell loaded with dielectric.

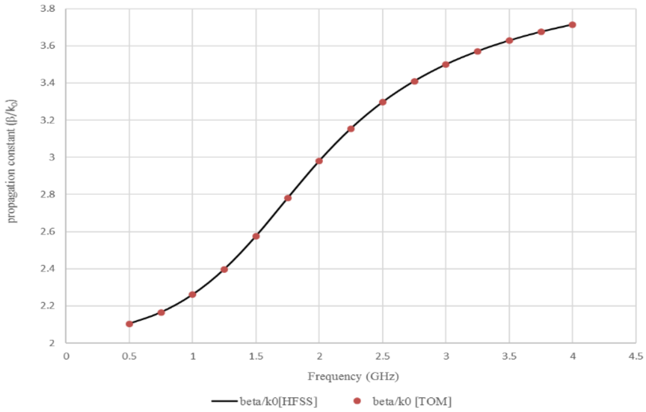

Fig.4. Constante de phase normalisée pour quasi-TEM dans une cellule coaxiale à deux couches sans perte, comparaison avec la simulation HFSS

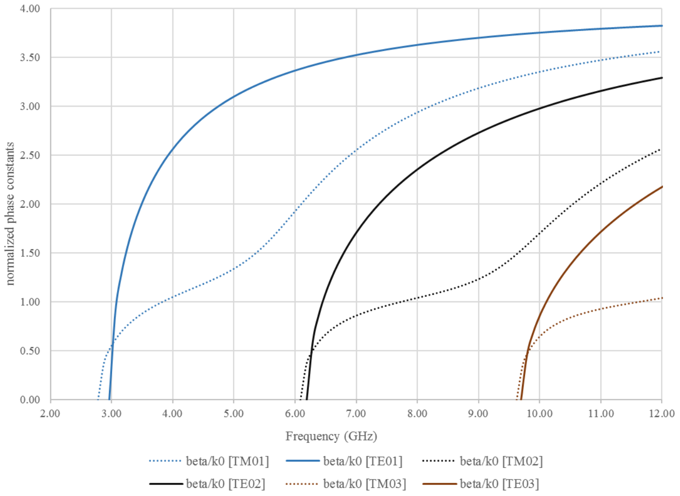

Fig.5. Constante de phase normalisée pour un ordre supérieur dans une cellule coaxiale à deux couches sans perte. Les modes sont disposés de gauche à droite TE_{01}, TM_{01}, TE_{02}, TM_{02}, TE_{03}, and TM_{03}.

Résultats numériques dans la structure coaxiale

Constantes de propagation dans une structure sans pertes

Une structure illustrée à la Fig.2.3 sera étudiée, avec la cellule coaxiale du rayon interne 6mm et externe 20mm, respectivement, et est remplie d'une couche diélectrique d'épaisseur 10mm et de constante diélectrique $\varepsilon_r = 16$; la couche d'air a une épaisseur de 4mm.

Dans la Fig.4, nos résultats théoriques sont comparés à ceux obtenus par la méthode des éléments finis à l’aide du logiciel commercial HFSS. Un bon accord est observé pour la caractéristique de dispersion pour une structure à deux couches sans perte sur une gamme de fréquences de 0,5 à 4 GHz. Des résultats sur les modes d'ordre supérieur sont illustrés sur la Fig.5.

Constantes de propagation dans une structure à deux couches avec pertes

Pour une ligne coaxiale de mêmes dimensions que le cas précédent, le matériau sans pertes de permittivité relative 16 est remplacé par de matériaux de même permittivité mais avec des tangentes de pertes non nulles. Nous avons comparé la constante d'atténuation normalisée et la constante de phase normalisée par notre méthode ('o') à celle du résultat de simulation par HFSS dans la même structure multicouche.

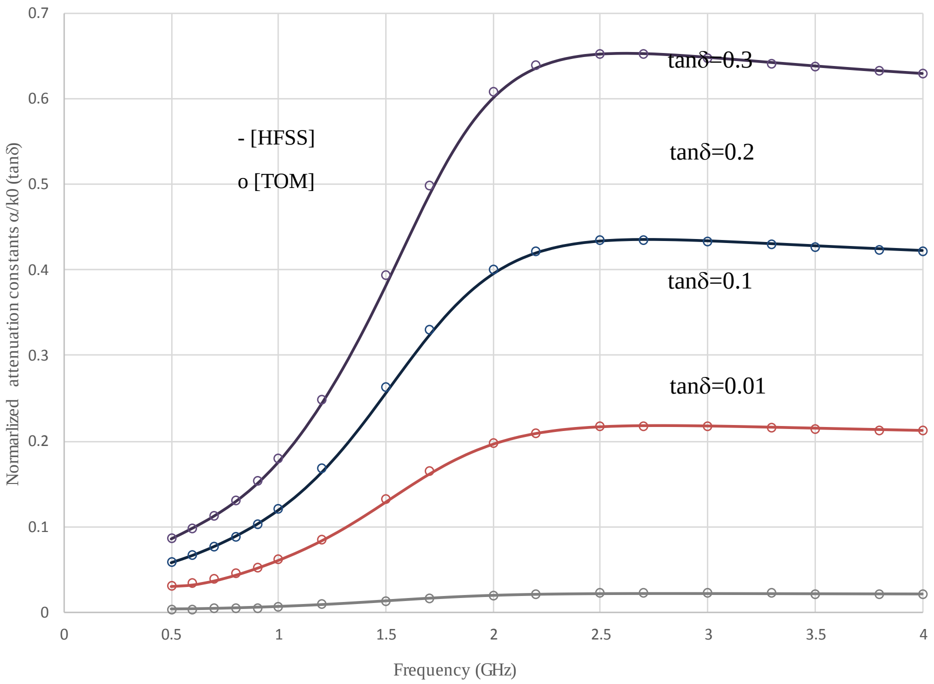

(a)

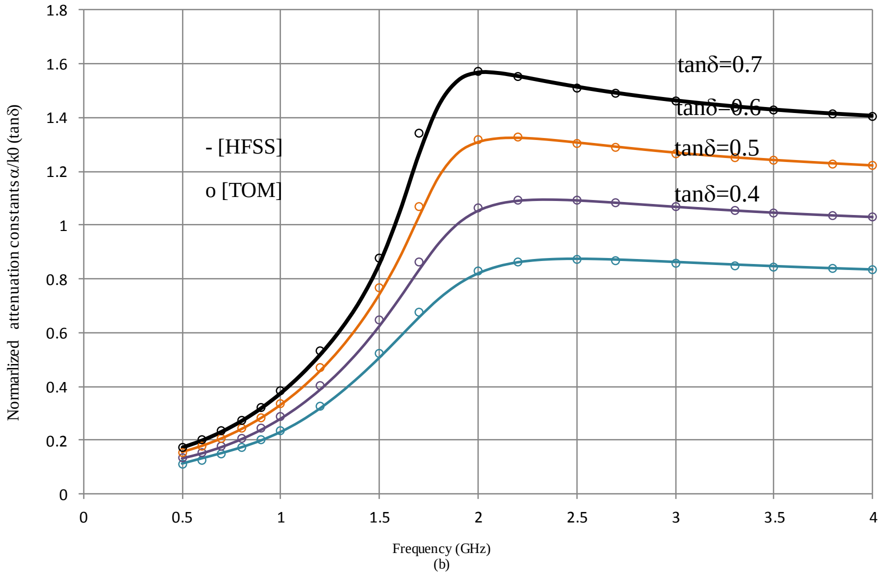

Fig.6. Constantes d'atténuation normalisées avec une tangent de perte (a) tanδ = 0,01 ; 0,1 ; 0,2 (b) tanδ = 0,4 ; 0,5 ; 0,6 de la cellule coaxiale chargée de diélectrique. Comparaison entre les résultats numérique ('o') et les résultats simulés de HFSS (lignes solide).

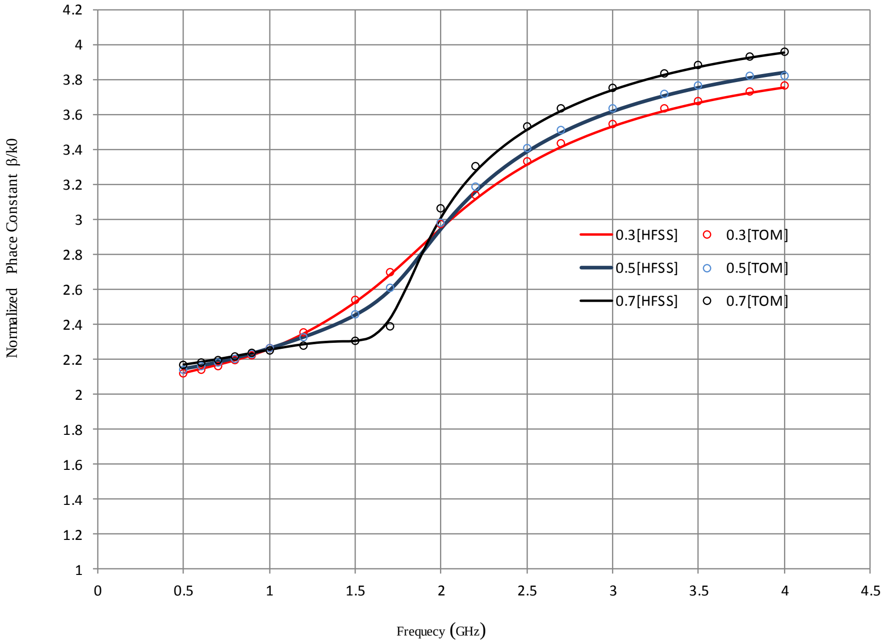

Fig.7. Constantes de phase normalisées avec une tangent de perte tanδ=0,3 ; 0,5 ; 0,7 de la cellule coaxiale chargée de diélectrique. Comparaison entre Comparaison entre les résultats numériques ('o') et les résultats de simulation de HFSS (lignes solide).

La Fig.6 compare des constantes d'atténuation normalisées. On peut constater que les résultats numériques obtenus à l’aide de la méthode de l'opérateur transverse ('o') sont en bon accord avec ceux du logiciel de simulation HFSS sur une gamme de fréquence allant de 0,5 à 4 GHz. La Fig.7 montre également un bon accord concernant les constantes de phase normalisées. Dans les expressions, les constantes de propagation complexes sont toutes normalisées par rapport à k_0, la constante de phase dans l'espace libre.

Constantes de propagation dans une structure à trois couches avec pertes

Une cellule coaxiale à trois couches a ensuite été étudiée. Les conducteurs métalliques ont les mêmes dimensions que le cas précédent. Une couche de Téflon est insérée entre le conducteur interne et le matériau à forte permittivité relative. Les constantes diélectriques complexes du téflon et de l'échantillon sont respectivement $\varepsilon_{rt} = 2{,}1\times(1-0{,}001i)$ et $\varepsilon_{rd} = 16\times(1-0{,}3i)$.

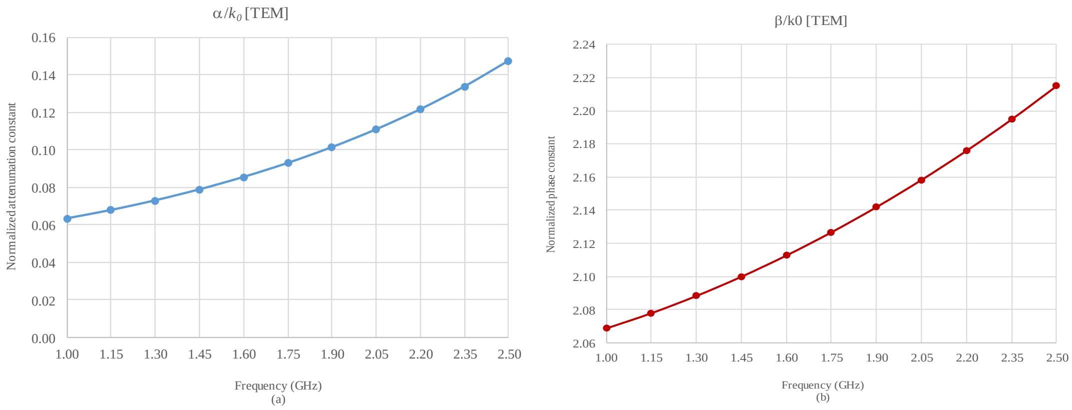

Fig.8. Constante de propagation complexe normalisée du mode fondamental (a) constante d'atténuation normalisée et (b) constante de phase normalisée de la cellule coaxiale à trois couches.

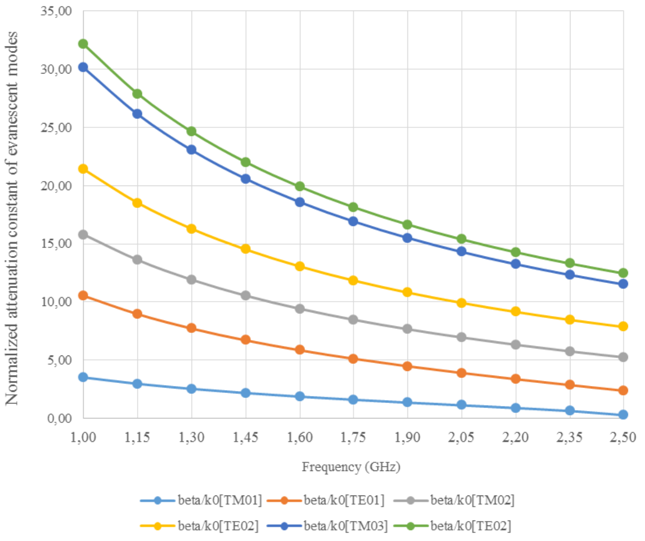

Fig.9. Constantes d'atténuation normalisées des modes évanescents d'ordre supérieur d'une cellule coaxiale à trois couches.

Nous avons étudié les constantes de propagation complexes du mode fondamental (quasi-TEM) et des modes d'ordre supérieur dans la gamme de fréquence allant de 1 à 2,5 GHz. Le mode quasi-TEM se propage dans la structure sans fréquence de coupure, alors que le premier mode d'ordre supérieur commence à se propager qu'à partir de 2,78 GHz. Par conséquent seul le mode quasi-TEM est propagatif entre 1 et 2,5GHz. La mode fondamentale est représenté sur la Fig.2.10. Néanmoins les modes évanescents seront excités dans des cellules de mesure près des discontinuités comme illustrées à la Fig.2.11.

Résultats numériques dans une structure planaire multicouche

Le matériau AD255C a été choisi pour la réalisation de la ligne micro-ruban de référence. C'est un substrat de permittivité relative $\varepsilon_r = 2{,}55$ et aux pertes faibles. Ce matériau permet la conception de circuits avec une faible constante diélectrique, un faible coût et d'excellentes caractéristiques de faibles pertes. La stabilité sur de larges plages de fréquence et de température le rend idéal pour diverses applications hyperfréquences et RF. Les autres paramètres de la ligne micro-ruban de référence représentée sur la Fig.10 sont : h = 1,524 mm, l'épaisseur du substrat ; w = 4,257 mm, la largeur de bande centrale et $t_1 = t_2 = 35\mu m$ l'épaisseur du conducteur de bande et du conducteur de masse.

Nous considérerons d'abord une structure multicouche avec une plaquette d'alumine de plusieurs épaisseurs, allant de 0,25mm à 2mm. Ensuite, la structure remplie d'une couche de plexiglas sera étudiée. Enfin, nous terminerons par un matériau céramique de la société Transtech pour lequel seul le cas sans perte est considéré. Ici, nous présenterons uniquement les structures multicouches remplies d'alumine, et les autres structures seront discutées clairement dans la thèse.

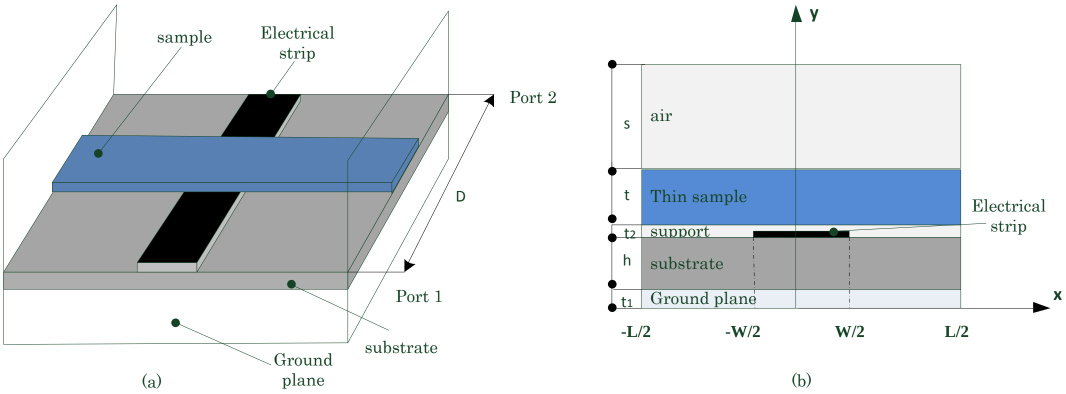

Fig.10. Cellule de mesure en ligne planaire chargé parc un échantillon de plaquette mince. (a) en trois dimensions et (b) en coupe transversale.

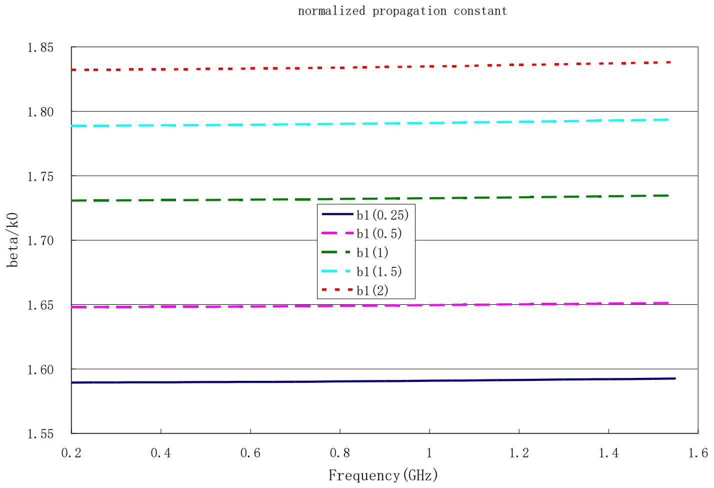

Fig.11. Constante de propagation normalisée de la ligne micro-ruban couverte d'alumine avec différentes épaisseurs de dalle (de 0,25 mm à 2 mm).

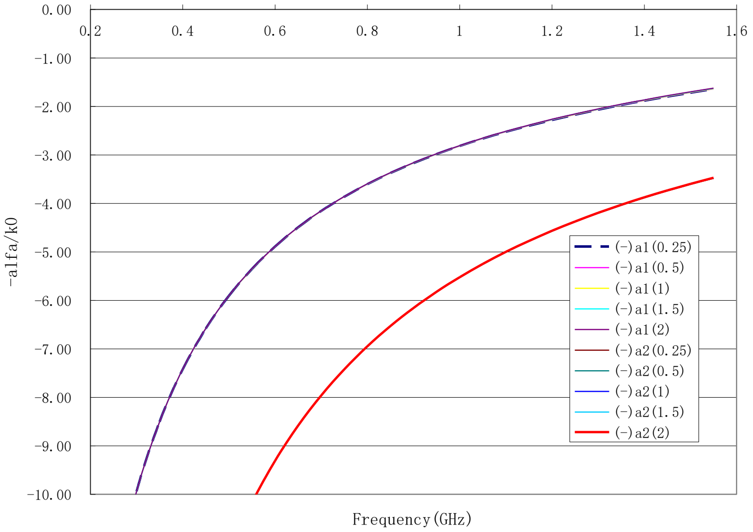

Fig.12. Constantes d'atténuation normalisées des deux premiers modes évanescents dans une ligne micro-ruban couverte d'alumine.

Nous considérons que la permittivité relative de notre plaque d'alumine est de 9,9 et les recherches de mode propre sont effectuées pour une épaisseur variant de 0,25mm à 2mm. L'influence de l'épaisseur de l'alumine sur la constante de propagation normalisée pour le mode quasi-TEM est illustrée à la Fig.11, tandis que le comportement en fréquence pour les premier et deuxième modes supérieurs est donné à la Fig.12.

Conclusion des études 2D :

Les bases modales des deux structures de propagation impliquées dans nos cellules de mesure diélectrique, structure coaxiale multicouche et structure planaire multicouche, ont été obtenue respectivement par deux méthodes de types modales : la méthode de l'opérateur transverse et la formulation de résonance transversale modifiée. Ces résultats seront utilisés pour l'étude tridimensionnelle des cellules de mesures correspondantes.

ETUDE TRIDIMENSIONNELLE DES DISCONTINUITÉS EN GUIDE D'ONDES

Dans des cellules de mesure impliquant des structures de propagation des zones transitoires entre deux guides de natures différentes sont souvent présentes. Ces zones constituent des zones de discontinuités (Fig.13).

L'effet de discontinuité est inévitable, car elle peut être délibérément introduite dans le circuit pour effectuer une certaine fonction (par exemple, diaphragme réactif dans un guide d'onde ou bouchons sur une ligne micro-ruban pour un circuit d'adaptation ou de filtrage). Une étude rigoureuse des discontinuités est indispensable pour décrire correctement le fonctionnement de l'ensemble.

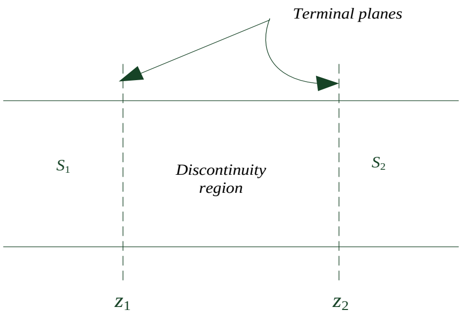

Fig.13. Structure de propagation avec la présence des discontinuités.

Analyse théorique

Chaque cellule de mesure étant constituée de plusieurs sections différentes, la matrice S de l'ensemble sera déterminée par l'utilisation de plusieurs méthodes modales : méthode du raccordement modal (MMM) et méthode variationnelle multimodale (MVM). Les codes d'analyse directe sont couplés avec plusieurs programmes d'optimisation pour constituer les logiciels d'extraction des paramètres matériaux. Ceux-ci sont appliqués à des échantillons de matériaux sous forme de cylindre trouée pour la cellule coaxiale, ou de plaquette rectangulaire mince pour la cellule micro-ruban. Des résultats d'extraction large bande ont été obtenus; des valeurs sont comparables avec ceux publiés. Aussi bien des diélectriques à fortes pertes que des matériaux nano structurés ont fait l’objet des études par nos méthodes.

Résultats numériques

La méthode variationnelle multimodale (MVM) et celle des raccordements modaux sont présentées pour caractériser les discontinuités simples et multiples entre structures guidantes uniaxiales. Ces méthodes seront utilisées pour l'analyse directe de deux structures principales de caractérisation de matériaux diélectriques : cellule en ligne coaxiale élargie et cellule en micro-ruban multicouche. Les résultats numériques seront introduits dans la modélisation inverse de chaque cellule de mesure en vue de l'extraction de la permittivité diélectrique à partir des mesures de paramètres S.

Analyse de discontinuité dans des structures coaxiales

Cette partie est consacrée à l'étude de discontinuité dans une cellule coaxiale élargie. Nous montrons ci-dessous une photo de la partie centrale de la cellule de mesure coaxiale sans conducteur extérieur, une figure (Fig.3.7) de la cellule de mesure globale incluant le connecteur N standard pour la transition coaxiale élargie et la discontinuité entre la ligne coaxiale élargie non remplie et la partie centrale remplie de matériau à mesurer. Une comparaison sera également effectuée avec les résultats de simulation de logiciels commerciaux.

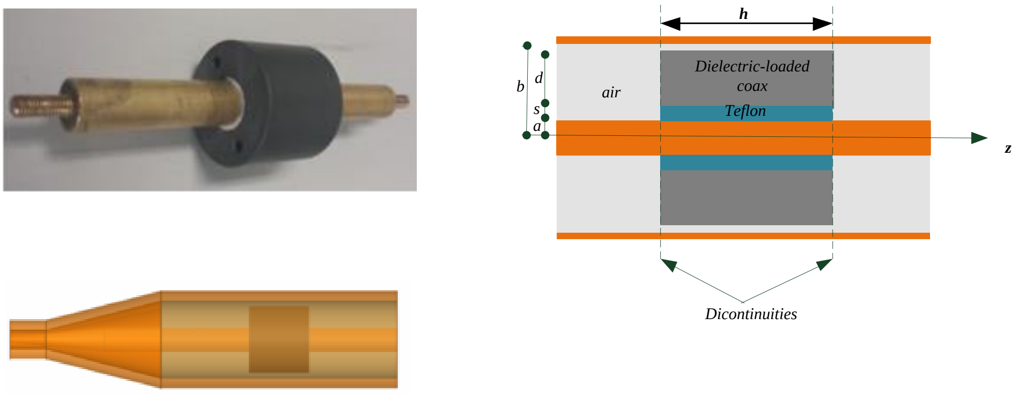

Fig.14. Discontinuités longitudinales (trois couches).

Les distributions de champ

Lorsqu’une technique basée sur la décomposition modale est choisie pour l’analyse d’une discontinuité, le couplage entre les modes propres d’un côté et de l’autre du plan de discontinuité est un élément crucial dans l’évaluation de l’effet de discontinuité par la matrice S. Ce terme de couplage s’exprime par le produit scalaire entre le champ électrique de chaque côté. La détermination de la répartition de champs est donc indispensable pour chaque mode. Dans le cas des structures coaxiales la composante radiale des champs a été comparée aux résultats obtenues avec le logiciel COMSOL utilisant un modèle axisymétrique 2D ; le bon accord laisse voir l'aboutissement prochain de la modélisation électromagnétique de la structure complète par une méthode modale.

Discontinuité simple

Comme le montre (Fig.3.7), les discontinuités incluent une discontinuité simple et plusieurs discontinuités doubles, et peut-être des discontinuités multiples. Une extension de la méthode du raccordement modal pour la détermination des paramètres S d'une discontinuité simple entre ligne coaxiale et ligne chargée a été présentée. D'abord nous avons obtenu des paramètres S avec un mode de chaque côté de la jonction dans le structure à deux couches (s = 0), puis pour la structure tri-couches (s = 2mm) lorsqu’une couche de téflon s’intercale entre le conducteur central et l’échantillon diélectrique à mesurer.

Discontinuité double

Un matériau céramique fait l'objet de notre étude. Pour limiter l'effet de gap d’air bien connu des mesures de matériau rigide, une couche de téflon remplira l'espace entre le conducteur central et l'échantillon céramique sous forme d’anneau. Le contrôle de cet espace à l’aide de matériau connu à faible permittivité réduit considérablement l'erreur lors d'extraction des paramètres diélectriques.

Nous allons maintenant étudier la double discontinuité avec une cellule coaxiale élargie partiellement remplie des couches multi-diélectriques dans la partie centrale. Pour valider notre analyse directe, nous utilisons une estimation de la permittivité relative de 16, et plusieurs valeurs de tangente de pertes. La hauteur de la bague est choisie pour être 60mm. C'est la hauteur réelle de l'échantillon dans la partie expérimentale qui sera décrite dans les applications de mesure.

Méthode du raccordement modal (MMM)

Dans la Fig.15, nous observons que les accords sont bons pour une tangente de perte d'essai de 0.2, alors qu'il y a une petite différence près de la transmission minimale pour une tangente de perte de 0.3. La méthode du raccordement mode a été utilisée pour ces comparaisons.

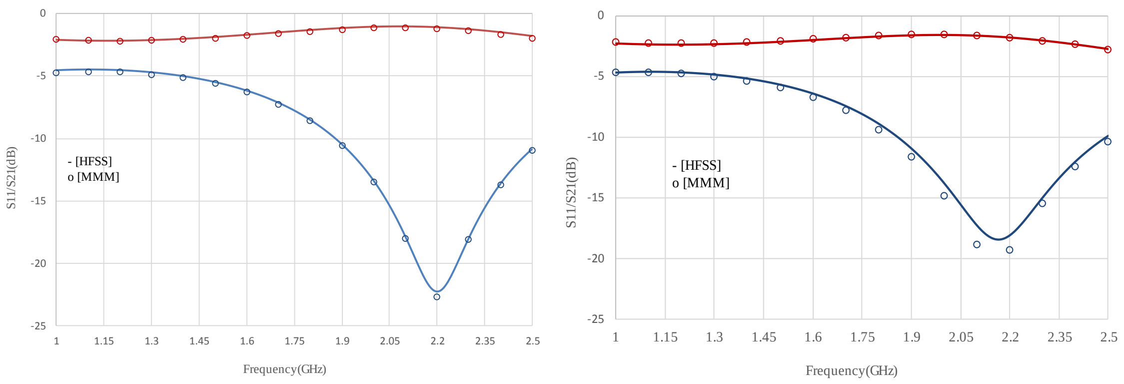

Fig.15. Double discontinuité entre ligne coaxial vide et celle partiellement remplie (3 couches). Pour Teflon $\varepsilon_r = 2.1(1-0.001i)$. A gauche $tan\delta=0.2$; A droite $tan\delta=0.3$.

Méthode variationnelle multimodale (MVM)

Pour la nécessité d'une étude de convergence, la formulation à double discontinuité de MVM est appliquée à un cas sans perte en faisant varier le nombre de modes dans la section partiellement remplie. Les résultats obtenus avec HFSS pour le coefficient de transmission dans la Fig.3.18 montrent un effet de résonance proche de 1.7GHz. L'analyse MVM a été effectuée sur des échantillons à fréquence limitée. Mais nous pouvons voir la grande influence du nombre de modes dans la partie centrale de la structure globale. En utilisant 6 modes propres dans la partie centrale, on peut observer un bon accord entre les résultats obtenus par MVM et ceux de HFSS à la fois pour le coefficient de réflexion et de transmission dans la Fig.3.19.

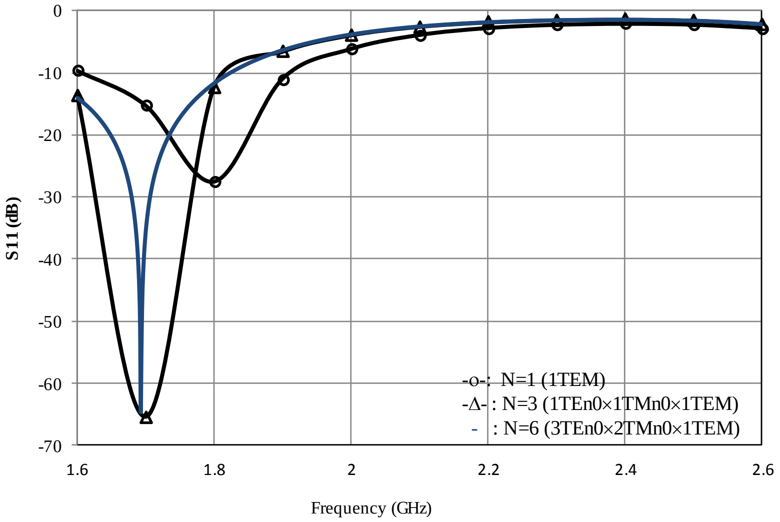

Fig.16. Comparaison S_{11} (dB) par rapport au nombre d'expansion de champ N de notre méthode de discontinuité double de la ligne coaxiale remplie avec l'échantillon sans perte.

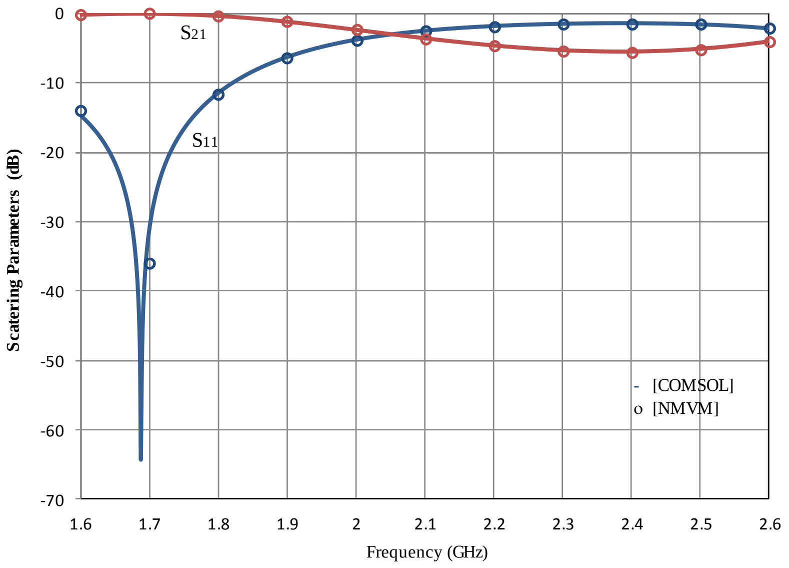

Fig.17. Comparaison S_{11}/S_{21} (dB) de notre méthode ('o') (N = 6) et résultats simulés par COMSOL de la discontinuité double de la ligne coaxiale remplie de l'échantillon sans perte.

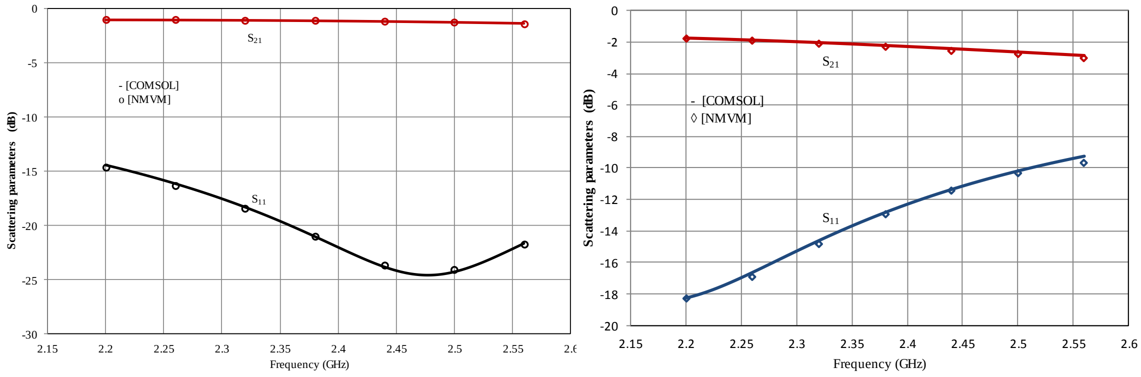

Fig.18. Comparaison S_{11}/S_{21} (dB) de notre méthode ('o') et de simulation COMSOL de la double discontinuité de la ligne coaxiale. La gauche avec un échantillon de tangente de perte (tanδ) 0.2 pris en sandwich par l'air; et le droit avec l'échantillon de tanδ = 0.3 pris en sandwich par le téflon et l'air.

Les céramiques avec pertes ont été étudiées par MVM et par COMSOL qui est un autre logiciel basé sur FEM. Nous pouvons voir que de bons accords ont été obtenus à la fois pour 0,2 (à gauche) et 0,3 (à droite) pour les tangentes des pertes dans la Fig.18.

Nous pouvons conclure que l'application de la méthode du raccordement modal et de la méthode variationnelle multimodale à la discontinuité de type coaxial donne des résultats raisonnablement précis, et son utilisation dans la modélisation inverse de la cellule de mesure diélectrique coaxiale sera présentée dans l'extraction des propriétés matérielles.

Analyse de discontinuité de la discontinuité micro-ruban multicouche

La structure planaire multicouche utilisée dans la configuration de mesure diélectrique est donnée dans la Fig.10, avec le côté droit de la micro-ruban chargée par l'échantillon diélectrique inconnu de couche mince. Dans cette partie nous ferons l'analyse directe afin d’obtenir la matrice de diffusion pour la modélisation inverse dans la caractérisation du matériau.

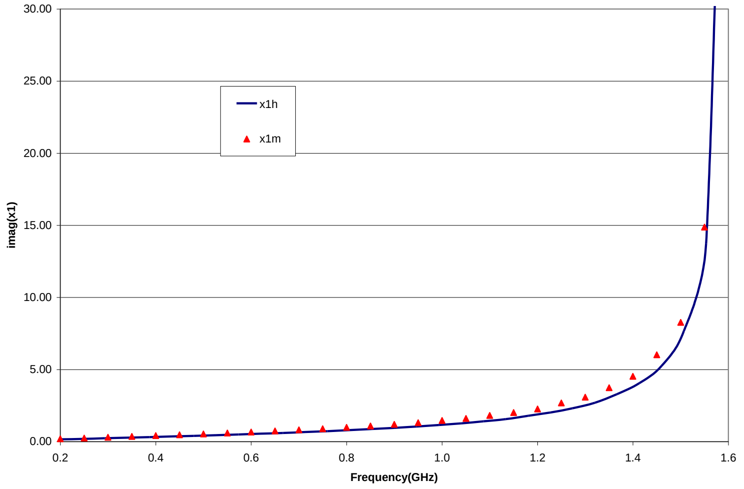

Fig.19. Comparaison sur imag (z_1) de notre méthode (triangle) et de HFSS (max(ΔS) =0.002).

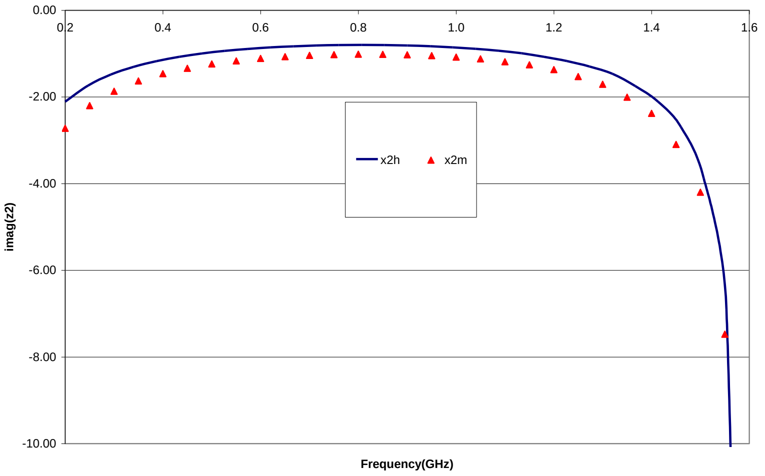

Fig.20. Comparaison sur imag (z_2) de notre méthode (triangle) et de HFSS (max(ΔS) =0.002).

Structure multicouche remplies d'alumine

Maintenant, pour une plaque d'alumine de 2 mm d'épaisseur et 50,8 mm de longueur, l'effet de discontinuité sera plus important avec une permittivité relative plus élevée.

Nous choisissons 9,5 comme valeur de test de la permittivité relative. Encore une fois, nous comparons nos résultats avec ceux obtenus à partir de HFSS avec un delta S maximum de 0,002. La comparaison de la partie imaginaire de l'impédance série est donnée à la Fig.3.24 tandis que celle de la partie imaginaire de l'impédance shunt de la Fig.3.25.

Nous avons donné une description de trois méthodes d'analyse de discontinuité de guide d'onde basées sur les modes propres. La méthode de raccordement modal et la méthode variationnelle multimodale ont été appliquées aux discontinuités impliquées dans la cellule de mesure diélectrique coaxiale. Les deux conduisent à des résultats comparables à des logiciels commerciaux basés sur des méthodes par éléments finis comme HFSS ou COMSOL.

Dans le cas des discontinuités de structure planaire multicouche, la double discontinuité symétrique a été modélisée par son schéma équivalent en T. Un bon accord a été observé entre les résultats obtenus par les différents outils d’analyse.

APPLICATIONS AUX CELLULES DE MESURE DIÉLECTRIQUES

Toutes les discussions sur les calculs numériques des structures multicouches permettent d’aborder la problématique de mesure de matériau à travers les deux cellules choisies dans le cadre de cette thèse. La cellule coaxiale et la ligne de transmission planaire sont appliquées à la mesure des propriétés électromagnétiques des matériaux. Pour cela des échantillons ont été préparés en forme d'anneau pour la cellule coaxiale, ou en forme de plaquette rectangulaire minces pour la cellule à base de ligne micro-ruban.

La déduction des propriétés matériaux à partir de la mesure des paramètres S comprend principalement deux étapes : les problèmes directs et les problèmes inverses. Le problème direct calcule les paramètres S de la cellule de mesure avec la présence de l’échantillon sous test ; seule le mode quasi-TEM se propage dans la gamme de fréquence choisie. A partir des valeurs estimatives de permittivité relative ε_r et de perméabilité relative μ_r, pour une fréquence donnée, les paramètres S peuvent être déduits numériquement. Le problème inverse permet la déduction des paramètres matériaux à l’aide des algorithmes d’optimisation s’appuyant sur la comparaison simulation/mesures.

Mesures et extraction de permittivité complexe dans la structure coaxiale

Nous présentons des mesures effectuées avec l'insertion d'un échantillon de matériaux céramiques à fortes pertes dans notre cellule de mesure coaxiale. L'échantillon annulaire est inséré dans la cellule coaxiale élargie à une position donnée. Une mesure en réflexion sera réalisée avec la cellule terminant par un court-circuit, donnant lieu à une impédance complexe équivalente d'un dipôle. Pour une mesure en réflexion/transmission la partie centrale élargie sera reliée aux câbles de connexion en connectique N à travers deux transitions coniques.

Description de la cellule de mesure

Pour les cellules de mesure diélectriques coaxiales, nous proposons la décomposition pour nos deux cellules de mesure comme suit (Fig.21).

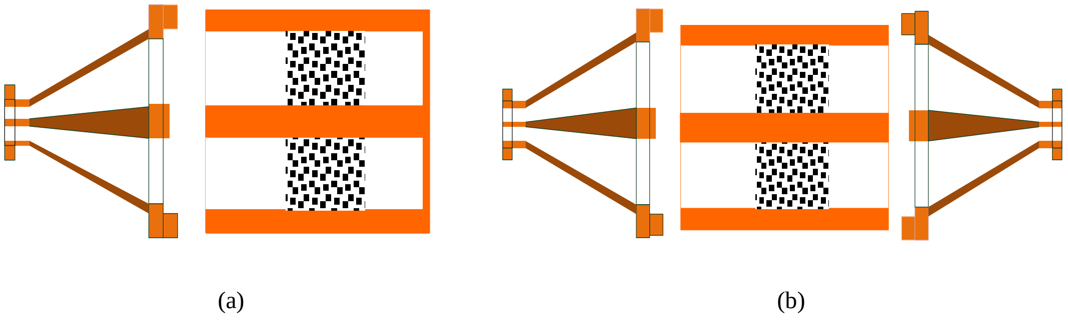

Fig.21. Configuration de mesure des cellules coaxiales. (a) Cellule réflexion (b) Cellule réflexion/transmission.

Une fois les paramètres S de l'ensemble obtenus, l'application d'une méthode de calibrage asymétrique conduit à une matrice S de la partie centrale référencée à une impédance de 73Ω d'une ligne coaxiale non standard. L'extraction de la permittivité complexe s'effectue en comparant ces paramètres S avec ceux obtenus par l'une des méthodes de modélisation électromagnétique. En attendant l'aboutissement de l'étude avec la méthode modale, nous avons déduit la loi de variation des permittivités avec les résultats de mesure.

Résultats numériques

La procédure de modélisation inverse est appliquée aux résultats de mesure d'un anneau céramique avec pertes. Dans notre installation, la longueur totale de la cellule coaxiale élargie est de 55,2 mm, avec les premiers 25,2 mm remplis d'air et dernier 30mm par le matériau céramique sous test. L'échantillon céramique est terminé par une plaque de court-circuit. Les rayons interne et externe sont respectivement de 8mm et 18mm pour l'échantillon en anneau, et la cellule coaxiale élargie a des rayons interne et externe respectivement de 6mm et 20mm. Nous utilisons donc du téflon de 2 mm d'épaisseur pour remplir l'espace entre l'anneau céramique et le conducteur interne de la cellule coaxiale. En introduisant les résultats mesurés dans la modélisation inverse, nous avons la permittivité relative complexe extraite comme montré sur la Fig.22.

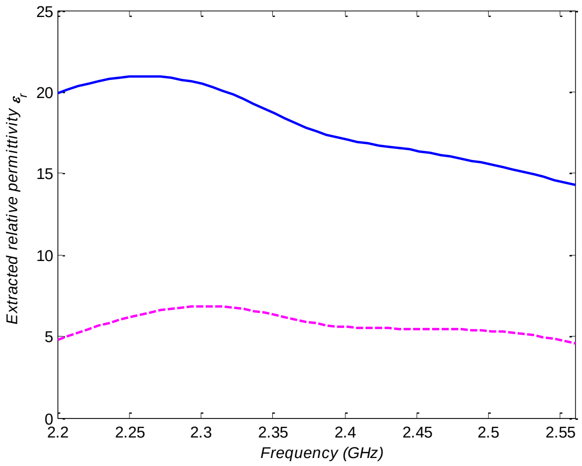

Fig.22. Parties réelles et imaginaires (-) de la permittivité relative extraite de l'échantillon testé.

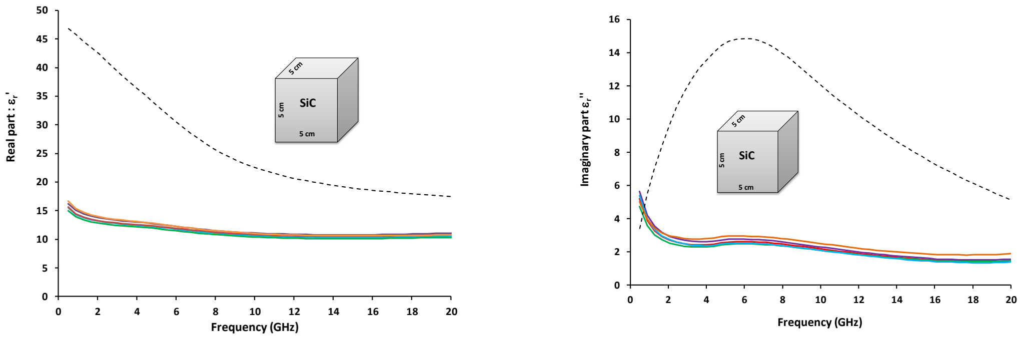

(a) (b)

Fig.23. Parties réelles (a) et imaginaires (b) de la permittivité relative données publiées avec le même matériau céramique.

Nous pouvons observer que la partie imaginaire est importante indiquant la nature à pertes de la matière céramique dans l'étude. Les résultats d'extraction pour des matériaux de même type obtenus avec d’autres types de cellules sont donnés à titre de comparaison (Fig.23). Comme ce dernier échantillon est un cube en céramique à 6 faces, la différence peut être importante entre la permittivité extraite en utilisant une face différente lors de la mesure.

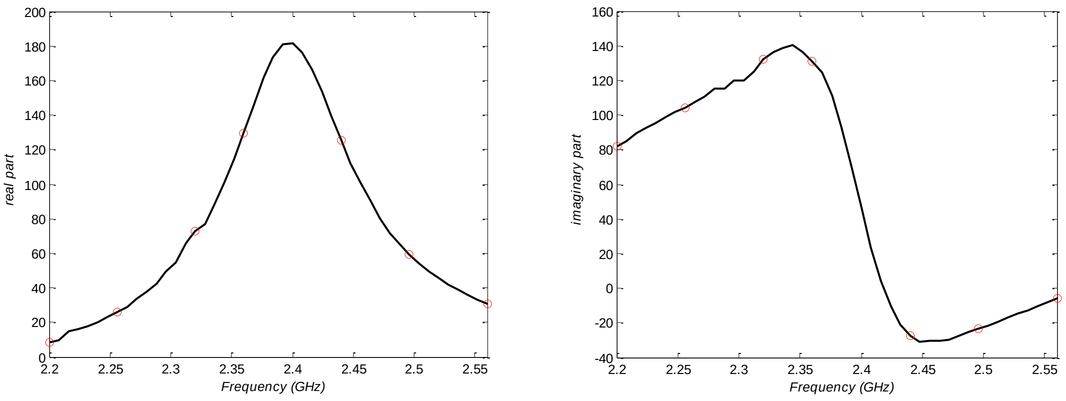

(a)

(b)

Fig.24. Comparaison des parties réelles (a) et imaginaires (b) de l'impédance d'entrée entre les données simulées ('o') et les résultats mesurés.

Afin de valider davantage les résultats de modélisation inverse, la permittivité relative complexe extraite a été réintroduite dans le logiciel de simulation COMSOL et le coefficient de réflexion résultant est utilisé pour déterminer la nouvelle impédance d'entrée à partir du connecteur N en utilisant un schéma équivalent de la transition. La Fig.4.17 compare la partie réelle et la partie imaginaire obtenues respectivement par la mesure et la simulation COMSOL. Un très bon accord peut être observé.

Mesures et extraction de propriétés matériaux dans la structure planaire

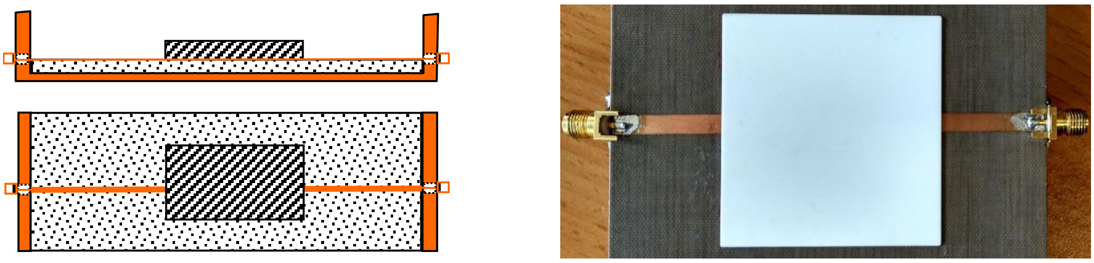

(a)

(b)

Fig.25. Configuration de mesure de micro-ruban. (a) schématique et (b) photo avec plaque d'alumine.

Description de la cellule de mesure

Une partie de la cellule de mesure à base de ligne micro-ruban est montrée dans la Fig.4.8, avec sa photo à droit, et les vues avant et supérieure à gauche. L'entrée et la sortie sont connectées au VNA via un connecteur SMA femelle d'impédance 50Ω.

Ainsi, la ligne micro-ruban de référence a été conçue pour avoir une impédance caractéristique de 50Ω.

Résultats numériques

Tout d'abord, les paramètres S sont mesurés à l'aide d'un VNA, ensuite, des transformations sont nécessaires pour obtenir les paramètres S entre les deux extrémités de la partie chargée de l'échantillon en utilisant la procédure d'étalonnage Thru-Reflect-Line (TRL). De plus, l'algorithme NRW permet la déduction de la permittivité relative effective et de la perméabilité de la ligne de transmission multicouche chargée par l'échantillon dans une large gamme de fréquences. Enfin, la permittivité complexe et la perméabilité des matériaux peuvent être extraites en utilisant la modélisation inverse.

- *Echantillon en alumine*

Pour illustrer cette procédure, nous considérons la mesure d'une plaque mince d'alumine de deux pouces carrés. L'application de l'algorithme NRW aux résultats de mesure nous permet de déduire la permittivité effective. Lors de l'introduction de ces résultats dans le programme de modélisation inverse 2D, la permittivité relative en fonction de la fréquence est illustrée sur la Fig.26.

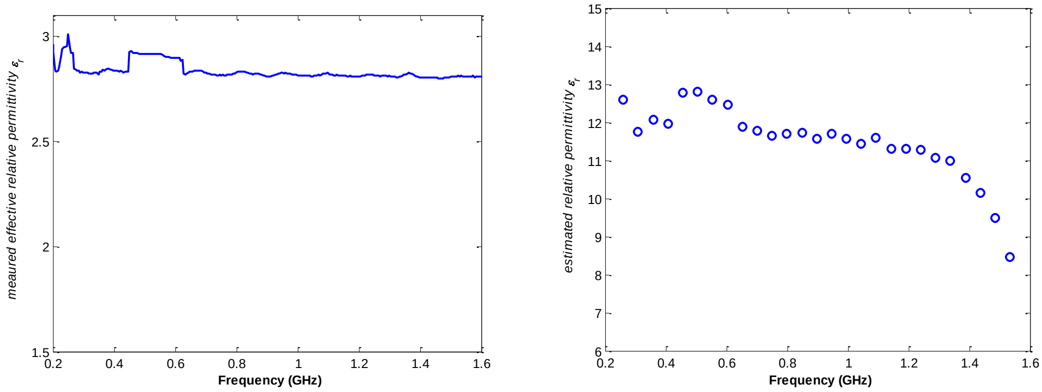

Fig.26. La permittivité relative effective (à gauche) de la ligne microruban couverte d'alumine et sa permittivité relative correspondante (à droite) obtenue avec la modélisation inverse.

En effet, dans l'algorithme NRW, aucune énergie électromagnétique réactive n'existe dans les régions de discontinuités car la configuration expérimentale d'origine ne donne pas lieu à des modes d'ordre supérieur. Malheureusement, ce n'est pas le cas avec une ligne de transmission hétérogène telle que la ligne micro-ruban. Cette énergie réactive contribue à modifier la longueur effective de la section centrale, introduisant ainsi une source d'erreur potentiellement importante. Nous proposons une procédure itérative pour minimiser l'erreur induite par la présence de cette énergie réactive en la modélisant comme un élément réactif localisé, déduit d'une simulation électromagnétique 3D d'une simple jonction.

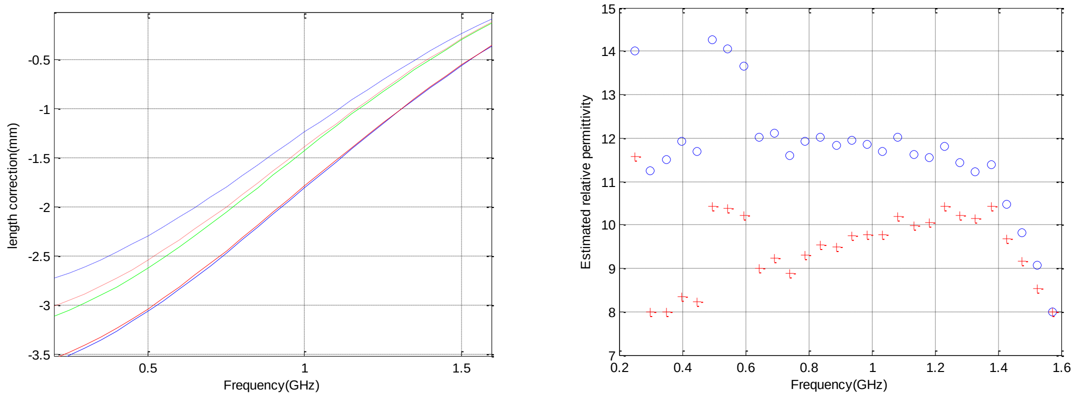

Fig.27. (a) Correction de longueur. (b) Comparaison entre les nouvelles valeurs ('+') et les anciennes ('o').

Dans la mesure de la plaque d'alumine, le modèle de jonction montre l'évolution de la longueur dl_1 du côté de la partie centrale, en fonction de la fréquence et de la permittivité relative estimée dans le cas de l'échantillon d'alumine (Fig.4.21 (a)). Cette longueur supplémentaire peut être supérieure à 3 mm dans certains cas, comparée à 50.8mm qui est la longueur réelle de la section centrale, son influence peut être importante dans les résultats d'extraction. Les nouvelles valeurs estimées ('+') de l'échantillon sont données dans la Fig.4.21(b) par rapport à celles dérivées directement des formulations NRW ('o'). Ces nouvelles valeurs correspondent mieux à celles attendues entre 9 et 11 comme prévu.

- *Matériau céramique TransTech*

Un autre exemple est présenté ici avec le diélectrique D-16 (Mg-Ti de Trans-Tech Company). La longueur de la plaque diélectrique est de 30,94 mm et 1,02 mm son épaisseur. Contrairement au cas ci-dessus, la correction de l'effet de discontinuité a été introduite dans la modélisation inverse. Dans cette partie, l'incertitude sur l'épaisseur de gap d'air a été prise en compte pour une mesure précise.

Dans le cas du D-16, la permittivité relative est donnée par TransTech, 16 à la fréquence de 9 GHz, et avec la tangente de perte faible inférieure à 10^{-3}. Il y a une grande différence entre les valeurs de la fiche technique et celles de modélisation inverse. Une solution simple est d'introduire une couche d'air d'une épaisseur donnée entre le ruban central et l'échantillon testé. Nous pouvons extraire la permittivité relative avec plusieurs épaisseurs de gap d'air (Fig.4.22), le choix de gap d'air de 0,1 mm produit alors des résultats proches de ceux de la fiche technique de la société.

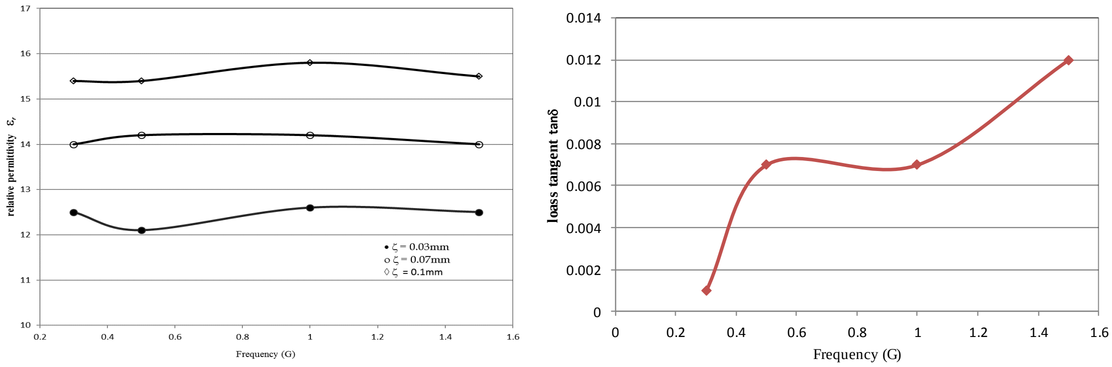

Fig.28. Permittivité relative extrait ε_r et perte tangente tanδ de l'échantillon.

- *Échantillon composite de nanostructure*

Plusieurs échantillons de nanostructures composites $Fe\text{-}Al_2O_3$ ont été fabriqués par le CIRIMAT à l'Université de Toulouse. Tous les échantillons sont métallisés d'un côté. Un bloc de métal carré est placé sur l'échantillon sous-test pour minimiser le gap d'air entre le ruban central et l'échantillon.

Après application de l'algorithme NRW aux résultats de mesure, les résultats bruts de la permittivité relative effective complexe et de la perméabilité de la région chargée avec l'échantillon sont obtenus; La permittivité relative et la perméabilité relative de ce matériau composite nanostructure sont extraites par la procédure de modélisation inverse (Fig.29). On peut remarquer que l'échantillon testé présente des pertes importantes et possède des propriétés magnétiques.

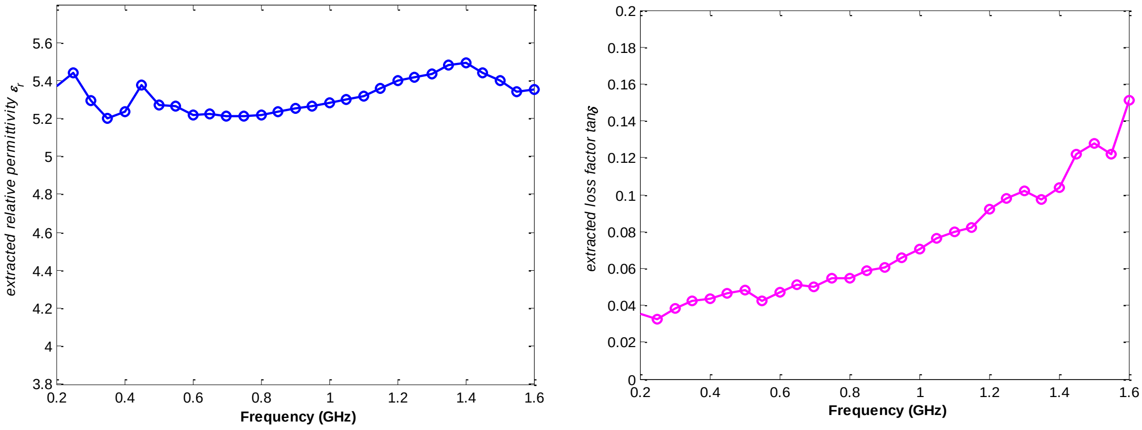

(a) (b)

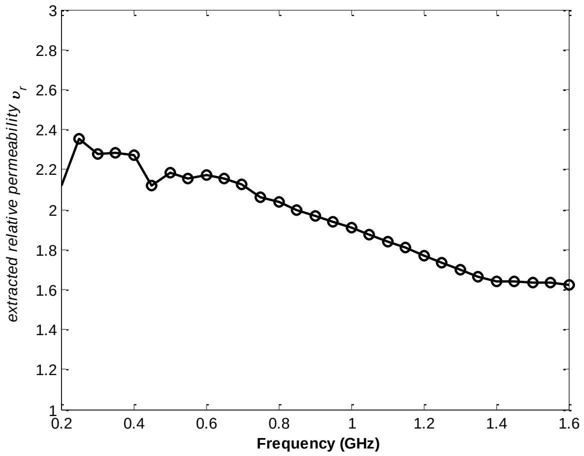

(c)

Fig.29. Propriétés électromagnétiques de l'échantillon. (a) Partie réelle et (b) partie imaginaire de la permittivité relative. (c) perméabilité relative.

CONCLUSION

L'objectif de cette étude est le développement des logiciels de modélisation électromagnétique spécifique aux cellules de caractérisation micro-ondes des matériaux. Ce développement s'appuie sur des méthodes numériques alternatives à celle des éléments finis largement utilisés dans des logiciels de commerce. Pour le besoin d'extraction des propriétés des matériaux par des méthodes de modélisation inverse, la recherche de l'efficacité numérique de l'analyse directe est le point central de cette étude.

Les méthodes basées sur la décomposition modale ont été mises en œuvre pour l'analyse directe des structures utilisées pour la réalisation des cellules de mesure diélectriques. On cite parmi ces méthodes la méthode de l'opérateur transverse, la méthode de résonance transverse modifiée, la méthode du raccordement modal, la méthode variationnelle multimodale. La modélisation inverse est appliquée pour extraire les propriétés du matériau dans les deux structures étudiées dans ce travail de thèse : la cellule coaxiale et la cellule planaire. Un certain nombre de matériaux ont été étudié, sur une large gamme de permittivité relative, avec des pertes plus ou moins importantes, y compris des matériaux composites à effet magnétique.

Publication

- 2016 - Analyse Electromagnétique d’une Ligne Coaxiale Partiellement Remplie de Diélectrique à Fortes Pertes

Authors : Jing-yi WANG, Jun-wu TAO, Jamal RAMMAL, Faycal BENMOHAMED, Li WU

National conférence: *Les Journées de Caractérisation Microondes et Matériaux (JCMM)*

- 2017 - An Efficient Numerical Method to Analyze Discontinuity of Coaxial Cable

Authors: Jingyi Wang, Junwu Tao, Fayçal Benmohamed

International conference: 2017 *International Applied Computational Electromagnetic Society (ACES) Symposium*

- 2017 - Numerical Simulation of Wave Propagation in Microstrip Line Containing Magnetic Layer

Authors: Faycal Benmohamed, Didier Vincent, Jing-yi Wang, Jun-wu. Tao

International conference: 2017 *International Applied Computational Electromagnetic Society (ACES) Symposium*

- 2017 - Extraction of Wideband Complex Permittivity in High Loss Material from a Coaxial Cell by Multimodal Variational Approach

Authors: Jing-yi Wang, Jun-wu. Tao, Tan-Hoa Vuong

International conference: *16th International conference on microwave and high frequency heating (AMPERE 2017)*

- 2017 - Microwave Characterization of Nanostructured Material by Modified Nicolson-Ross-Weir Method (also updated to be AMPERE Newsletter)

Authors: Jing-yi Wang, Jun-wu. Tao, Laura Severac, David Mesguich, Christophe Laurent

International conference: *16th International conference on microwave and high frequency heating (AMPERE 2017)*

- 2017 - An Accurate Spectral Domain Method to Analyze Multilayered Striplines on Magnetized Ferrite (submitted)

Authors: Fayçal Benmohamed, Jing-yi Wang, Jun-wu Tao, Noemen Ammar, Didier Vincent

Journal: IEEE Antennas and Wireless Propagation Letters